REPUBLIC OF TÜRKİYE

YILDIZ TECHNICAL UNIVERSITY

GRADUATE SCHOOL OF SCIENCE AND ENGINEERING

PRODUCTION OF GRAPHENE BASED NEW GENERATION ANODE MATERIALS FOR SODIUM ION BATTERIES AND INVESTIGATION OF THEIR PERFORMANCES

MohammedMustafa Hussein M ALMARZOGE

DOCTOR OF PHILOSOPHY THESIS

Department of Metallurgical and Material Engineering

Program of Materials Science and Engineering

Supervisor

Prof. Dr. Metin GENÇTEN

November, 2025

REPUBLIC OF TÜRKİYE

YILDIZ TECHNICAL UNIVERSITY

GRADUATE SCHOOL OF SCIENCE AND ENGINEERING

PRODUCTION OF GRAPHENE BASED NEW GENERATION ANODE MATERIALS FOR SODIUM ION BATTERIES AND INVESTIGATION OF THEIR PERFORMANCES

A thesis submitted by MohammedMustafa Hussein M ALMARZOGE in partial fulfillment of the requirements for the degree of **DOCTOR OF PHILOSOPHY** is approved by the committee on 14.11.2025 in Department of Metallurgical and Material Engineering, Program of Materials Science and Engineering.

Prof. Dr. Metin GENÇTEN
Yildiz Technical University
Supervisor

Approved By the Examining Committee

Prof. Dr. Metin GENÇTEN, Supervisor
Yildiz Technical University _____

Assoc. Prof. Dr. Burak BİROL, Member
Yildiz Technical University _____

Assist Prof. Dr. Nilüfer KOÇYİĞİT, Member
Biruni University _____

Prof. Dr. Hale BERBER, Member
Yildiz Technical University _____

Prof. Dr. Nilgün KARATEPE YAVUZ, Member
Istanbul Technical University _____

I hereby declare that I have obtained the required legal permissions during data collection and exploitation procedures, that I have made the in-text citations and cited the references properly, that I haven't falsified and/or fabricated research data and results of the study and that I have abided by the principles of the scientific research and ethics during my Thesis Study under the title of "Production of Graphene Based New Generation Anode Materials for Sodium Ion Batteries and Investigation of Their Performances" supervised by my supervisor, Prof. Dr. Metin GENÇTEN. In the case of a discovery of false statement, I am to acknowledge any legal consequence.

MohammedMustafa Hussein M ALMARZOGE

Signature

This work was supported by Yildiz Technical University Scientific Research Council (BAP) under FCD-2024-6420 project code and FDK-2024-6346 Doctoral Project code.

Dedicated to my parents,
my wife, my son Ali, and
my daughters Zainab and
Ruqaya…

ACKNOWLEDGEMENTS

First of all, profusely thanks be to ALLAH, the Lord of all creations, who enabled me to achieve this work. I would like to express my sincere gratitude to my supervisor, Prof. Dr. Metin GENÇTEN, for his invaluable guidance, encouragement, and support throughout my doctoral studies. His mentorship extended far beyond scientific training- his advice, motivation, and moral support, especially during difficult moments, were instrumental in the successful completion of this work. He was not only a supervisor but also a true friend, treating me and every member of our research group like family.

I am also grateful to my colleagues and friends for creating a collaborative, inspiring, and supportive environment. I thank the Gençten Research Group (GRG) and YTU Waste Recycling Research Group (WRRG) at Yildiz Technical University for their technical and academic support. I extend my sincere gratitude to our esteemed jury members, Assoc. Prof. Dr. Burak Birol, Prof. Dr. Hale Berber, Prof. Dr. Nilgun Karatepe Yavuz, and Assist. Prof. Dr. Nilüfer Koçyiğit, for their valuable insights and contributions. I would also like to thank Assoc. Prof. Dr. Gamzenur Özsin (Bilecik Şeyh Edebali University) for her continued support. I am deeply indebted to my lab mates in the gençten research group for their collaboration, encouragement, and friendship. You truly made the laboratory a productive and enjoyable place to grow. It was a true privilege to be a part of this journey and to work with such an invaluable team. Finally, and most importantly, I extend my heartfelt gratitude to my family—my parents, my wife, my son Ali, and my daughters Zainab and Ruqaya—for their endless love, patience, and unwavering support. They have been the foundation of my strength and the reason I never gave up. This achievement is not mine alone, it belongs to everyone who supported me along the way.

MohammedMustafa Hussein M ALMARZOGE

TABLE OF CONTENTS

LIST OF SYMBOLS ix

LIST OF ABBREVIATIONS x

LIST OF FIGURES xi

LIST OF TABLES xiv

ABSTRACT xv

ÖZET xvii

1 INTRODUCTION 19

1.1. Energy Storage Systems (ESSs). 19

1.1.1. Sodium-Ion Batteries (SIBs). 20

1.2. Scope and aim of the thesis 28

2 EXPERIMENTAL 29

2.1. Chemicals 29

2.2. Preparation of single- and co-doped graphene powders 29

2.3. Coin Cell Preparation. 30

2.3.1. Single-DGO. 30

2.3.2. Dual doped (N-S-GO). 31

2.4. Electrochemical Measurements 31

2.5. Characterization of DGO powders. 32

3 RESULTS 34

3.1 Characterization Single DGO Powder 34

3.1.1. XRD 34

3.1.2. XPS 35

3.1.3. FT-IR. 39

3.1.4. Raman spectroscopy 42

3.1.5. BET 44

3.1.6. SEM-EDX 46

3.1.7. TEM 49

3.2. Characterization of Dual DGO (N-S-GO) Powder 51

3.2.1. XRD 51

3.2.2. XPS 51

3.2.3. FT-IR 53

3.2.4. Raman spectroscopy 53

3.2.5. BET 54

3.2.6. FE-SEM-EDX 55

3.2.7. TEM 56

3.3. Electrochemical Results of Single DGO Anodes using $NaPF_6$ in EC: DMC- with 10%FEC electrolyte. 57

3.3.1. CV 57

3.3.2. Rate performance results 57

3.3.3. Long cycling performance 59

3.3.4. EIS 59

3.3.5. Calculation of Na^+ Diffusion Coefficients (D_{Na+}) 61

3.4. Electrochemical Results of Single DGO Anodes Using $NaPF_6$ in Diglyme Electrolyte. 62

3.4.1. CV 62

3.4.2. Rate performance results 63

3.4.3. Long cycling performance 63

3.4.4. EIS 65

3.4.5. Calculation of Na^+ Diffusion Coefficients (D_{Na+}) 66

3.5. Results of Dual DGO (N-S-GO) Anode Using $NaPF_6$ in Diglyme Electrolyte. 70

3.5.1. CV 70

3.5.2. Rate performance results 71

3.5.3. Long cycling performance 72

3.5.4. EIS 73

3.5.5. Calculation of Na^+ Diffusion Coefficients (D_{Na+}) 74

4 CONCLUSION **76**

REFERENCES **79**

PUBLICATIONS FROM THE THESIS **94**

LIST OF SYMBOLS

σ	Warburg coefficient.
C	Charge or Discharge Rate
D_{EIS}	Na^+ diffusion coefficient based on EIS results
D_{CV}	Na^+ diffusion coefficient based on CV results
mAh g^{-1}	milliampere-hour per gram
J mol^{-1} K^{-1}	joules per mole per kelvin
$\omega^{-1/2}$	inverse square root of angular frequency

LIST OF ABBREVIATIONS

A	Amper
Ag/AgCl	Silver/Silver Chloride
BET	Surface Area Measurements by Brunauer-Emmett-Teller
CV	Cyclic Voltammetry
GO	Graphene oxide
ClGO	Chlorine-doped graphene oxide powders
EDS	Energy Dispersive X-ray Spectroscopy
EIS	Electrochemical Impedance Spectroscopy
ESSs	Energy Storage Systems
FT-IR	Fourier transform infrared spectrophotometry
F	Faraday constant (96485 C mol^{-1})
GCD	Galvanostatic Charge and Discrage Tests
Lα	Nanocrystalline domain size (nm)
LIBs	Lithium-ion batteries
NGO	Nitrogen Doped graphene oxide powder
N-S-GO	Nitrogen and sulfur dual-doped graphene oxide powder
Pt	Platinum
SEI	Solid-electrolyte interface
SIBs	Sodium-ion batteries
SEM	Scanning Electron Microscopy
SGO	Sulfur doped graphene oxide
XRD	X-Ray Diffractometer
Z’	Real resistance (ohm)
Z_{Img}	Imaginary resistance (ohm)

LIST OF FIGURES

Figure 1.1 Advancement in Graphene-Based Nanocomposites As High-Capacity Anode Materials for Sodium-Ion Batteries [14]. 21

Figure 2.1 Coin-Cell Configuration. 31
Figure 2.2 Equivalent Circuit Model for Fitting Process of EIS. 32

Figure 3.1 XRD Pattern of (A) ClGO, (B) SGO, and (C) NGO-Based Powders. 34
Figure 3.2 XPS Analysis of ClGO Based Powders. 36
Figure 3.3 XPS Analysis of SGO Based Powders. 37
Figure 3.4 XPS Analysis of SGO Based Powders. 38
Figure 3.5 ClGO FT-IR Spectrum. 39
Figure 3.6 SGO FT-IR Spectrum. 40
Figure 3.7 NGO FT-IR Spectrum. 41
Figure 3.8 Raman Spectra of (A) ClGO, (B) SGO, and (C) NGO Based Powders. 42
Figure 3.9 (A-C) Nitrogen Adsorption/Desorption Isotherms Curves, (D-F) The Corresponding Pore-Size Distribution Curves of ClGO, SGO, and NGO Powders, Respectively. 45
Figure 3.10 ClGO SEM- EDS Mapping (A) Area Selected for EDS, (B) All Elements, (C) Carbon, (D) Oxygen, (E) Chlorine, (F) Compositional Percentages, and SEM Images of ClGO Powder Captured From The Same Surface Area at Different Magnifications: (G) 40k×, (H) 20 k×, and (I) 10 k×. 46
Figure 3.11 SGO SEM- EDS Mapping (A) Area Selected for EDS, (B) All Elements, (C) Carbon, (D) Oxygen, (E) Sulfur, (F) Compositional Percentages, and SEM İmages of SGO Powder Captured From The Same Surface Area at Different Magnifications: (G) 40k×, (H) 20 k×, and (I) 10 k×. 47
Figure 3.12 NGO SEM- EDS Mapping (A) Area Selected for EDS, (B) All Elements, (C) Carbon, (D) Oxygen, (E) Nitrogen, (F) Compositional Percentages, and SEM Images of SGO Powder Captured From The Same Surface Area at Different Magnifications: (G) 40k×, (H) 20 k×, and (I) 10 k×. 48
Figure 3.13 TEM Images of Synthesized ClGO. 49
Figure 3.14 TEM Images of Synthesized SGO. 49
Figure 3.15 TEM Images of Synthesized NGO. 50
Figure 3.16 XRD Pattern of N-S-GO Based Powders. 51
Figure 3.17 (A) Synthesized N-S-GO Powder XPS Survey, (B) O1s, (C) C1s, (D) S2p, and (E) N1s. 52
Figure 3.18 N-S-GO FT-IR Spectrum. 53
Figure 3.19 Raman Spectra Of N-S-GO Based Powders. 54

Figure 3.20 (A) Nitrogen adsorption/desorption isotherms curve, (B) The corresponding pore-size distribution curve of N-S-GO powder. 55
Figure 3.21 (A-D) FE-SEM Images of N-S-GO at Magnifications of (A) 25k×,(B) 50k×,(C and D) 100k× (E) Combined Elemental Mapping EDS Distribution Analysis; (F) Carbon; (G) Oxygen; (H) Nitrogen; (I) Sulfur. 56
Figure 3.22 TEM Images of Synthesized N-S-GO. 56
Figure 3.23 Three Consecutive Cyclic Voltammograms at 0.5 mV s^{-1} Scan Rate for: (A) ClGO, (B) SGO, and (C) NGO. 57
Figure 3.24 Single DGO Rate Performance Test: (A) ClGO, (B) SGO, and (C) NGO. 58
Figure 3.25 Capacity Retention vs. Coulombic Efficiency—Long-Term Cycling Performance (at 2C for 100 Cycles): (A) ClGO, (B) SGO, and (C) NGO. 59
Figure 3.26 Nyquist Plots for: (A) ClGO, (B) SGO, and (C) NGO, Using $NaPF_6$ in EC:DMC With 10% FEC Electrolyte. (D-F) Represent The Corresponding Typical Plots for Z' vs. ($\omega^{-0.5}$) in The Low-Frequency Region. 60
Figure 3.27 CV at Different Scan Rates (0.3-1.3 mV s^{-1}) for (A) ClGO, (B) SGO, and (C) NGO. 62
Figure 3.28 Rate Performance at Different Scan Rates, for (A) ClGO, (B) SGO, and (C) NGO. 63
Figure 3.29 Long-Term Cycling Test at 2C for 500 Cycles: (A) ClGO, (B) SGO, and (C) NGO. 64
Figure 3.30 Long-term cycling test at high rate of 5C for 100 cycles for (A) ClGO, (B) SGO, and (C) NGO. 64
Figure 3.31 Long-Term Cycling Test at High Rate of 10 C for 50 Cycles: (A) ClGO, (B) SGO, and (C) NGO. 65
Figure 3.32 Nyquist Plots for (A) ClGO, (B) SGO, and (C) NGO, using $NaPF_6$ in Diglyme Electrolyte. (D-F) Represent the Corresponding Typical Plots for Zreal vs. ($\omega^{-0.5}$) in the Low-Frequency Region. 65
Figure 3.33 Linear Fitting Profile Between the Peak Current and Square Root of the Scan Rate (A) ClGO, (B) SGO, And (C) NGO. 67
Figure 3.34 log (Peak Current) vs. log (ν, Scan Rate) for (A) ClGO, (B) SGO, and (C) NGO. 68
Figure 3.35 Relationship Between [(Peak Current / Square Root of Scan Rate) / Square Root of Scan Rate] for (A) ClGO, (B) SGO, and (C) NGO. .. 68
Figure 3.36 Total Na^+ Intercalation and Capacitive Contributions for (A) ClGO, (B) SGO, and (C) NGO. 69
Figure 3.37 CV at Different Scan Rates (0.3-10 mV s^{-1}). 70
Figure 3.38 N-S-GO Rate Performance at Different Scan Rates. 71
Figure 3.39 Long-Term Cycling Test at 2 C for 100 Cycles. 72
Figure 3.40 Long-Term Cycling Test at 5C for 50 Cycles. 72
Figure 3.41 Nyquist Plots and the Inset Shows the Equivalent Circuit. 73
Figure 3.42 (A) The Typical Plots Between Z' vs. ($\omega^{-0.5}$) in the Low Frequency Regain, (B) CV at Scan Rates (0.3-1.3 mv s^{-1}), (C) Linear Fitting Profile Between the Peak Current and Square Root of the Scan Rate , (D) log(i) Vs. log(*ν*), (E) Relation Between [(Peak Current / Square Root of Scan Rate)/Square Root of Scan Rate], (F) Total Na^+ Intercalation and Capacitive Contributions. 74

Figure 4.1 (A) Initial Discharge Capacity (B) 2nd Discharge Capacity, at 0.1C Rate. 77
Figure 4.2 Long Cycle Performance (A) 2C, (B) 5C, and (C) 10C, Utilizing Ether-Based Electrolytes. 77

LIST OF TABLES

Table 2.1 Experimental Parameters Employed for Powder Synthesis Via The Chronoamperometric Method. 30

Table 3.1 Raman Spectra Comparison Between ClGO, SGO, and NGO. 44
Table 3.2 BET Results of ClGO, SGO, and NGO. 45
Table 3.3 The Snigle DGO Using $NaPF_6$ in EC:DMC with 10% FEC Electrolyte Fitting Parameters For Electrochemical Impedance Spectroscopy (EIS) are as Follows: Rs is the Solution (Ohmic) Resistance, Rct is the Charge Transfer Resistance, CPE is the Constant Phase Element, And Zw is Warburg Impedance. 60
Table 3.4 The Snigle DGO Using $NaPF_6$ in Diglyme Electrolyte Fitting Parameters for Electrochemical Impedance Spectroscopy (EIS) are as Follows: Rs is the Solution (Ohmic) Resistance, Rct is the Charge Transfer Resistance, CPE is the Constant Phase Element, and Zw is the Warburg Impedance. 66
Table 3.5 The N-S-GO Using $NaPF_6$ In EC:DMC with 10% FEC Electrolyte Fitting Parameters for Electrochemical Impedance Spectroscopy (EIS) are as Follows: Rs is the Solution (Ohmic) Resistance, Rct is the Charge Transfer Resistance, CPE is the Constant Phase Element, And Zw is The Warburg Impedance. 73

ABSTRACT

Production of Graphene Based New Generation Anode Materials for Sodium Ion Batteries and Investigation of Their Performances

MohammedMustafa Hussein M ALMARZOGE

Department of Metallurgical and Material Engineering
Doctor of Philosophy Thesis

Supervisor: Prof. Dr. Metin GENÇTEN

Sodium-ion batteries (SIBs) have gained significant attention in recent years due to the global abundance and cost-effectiveness of sodium, making them a promising alternative to lithium-based batteries. This thesis introduces a straightforward, one-step, cost-effective, appropriate for large-scale application and eco-friendly chronoamperometric method for the synthesis of graphene oxide powders doped with chlorine (ClGO), sulfur (SGO), nitrogen (NGO), and a mixture of nitrogen and sulfur (N–S–GO).

XRD, Raman spectroscopy, XPS, FT-IR, BET, SEM, and TEM, were utilized to thoroughly analyze the structure and morphology of the doped powders. The structures comprised few-layered graphene oxide, consisting of around 2–3 layers, with nanocrystalline domains measuring 46–50 nm and having 18–19 sp^2 carbon rings. Doping led to an increase in interlayer spacing up to (6.7˚A) for ClGO, (3.38˚A) for SGO, (6.8˚A) NGO, and (6.58Å) for N-S-GO, enhancing the mobility and retention of Na^+ ions. XPS examination verified the successful covalent attachment of heteroatoms, resulting in the creation of C–Cl, Cl-Ox (x = 2, 3, 4), $C–SO_x–C$ (x = 2, 3), C–N, and C–S–C bonds, while also incorporating oxygenated groups that augment surface reactivity and defect density. Raman measurements

revealed heightened disorder ratios (I_D/I_G), indicating a greater number of defect sites favorable for sodium storage.

Electrochemical experiments revealed that all doped GO anodes displayed significant effectiveness in sodium storage. Two different electrolyte systems were utilized for the single DGO. The initial specific discharge capacity of ClGO, SGO, and NGO are 389.7, 256.7, and 200 mAh g^{-1} at a current rate of 0.1 C using 1 M of $NaPF_6$ in carbonate-based electrolyte with Na^+ diffusion coefficient (D_{EIS}) calculated to be about $6.8x10^{-13}$, $4.01x10^{-12}$, and $4.86x10^{-12}$ cm^2 s^{-1}, respectively.

Compared to 415, 733, and 952 mAh g^{-1} and (D_{EIS}) calculated to be about $7.49x10^{-10}$, $1.67x10^{-9}$, and $6.03x10^{-10}$ cm^2 s^{-1} of the ClGO, SGO, and NGO anodes using ether-based electrolyte. Whereas N-S-GO tested as anode using only ether-based electrolyte where shows an initial specific discharge capacity of 457mAh g^{-1} and (D_{EIS}) was calculated to be approximately 4.4 x 10^{-11} cm^2 s^{-1} before cycling and 3.2 x 10^{-10} cm^2 s^{-1} after cycling indicating effective ion transport. The synthesized anode has outstanding performance at high rates of 2C, 5C, and 10C when an ether-based electrolyte is employed, indicating its suitability as a high-rate anode material for (SIBs).

Prolonged cycling evaluations exhibited remarkable stability, with approximately 100% capacity retention after 100 cycles at a rate of 2C. The enhanced electrochemical performance arises from the synergistic effects of heteroatom doping, augmented interlayer spacing, and defect-induced pseudocapacitance, which jointly boost conductivity and the diffusion rate of Na^+. This study illustrates that heteroatom-doped graphene oxides synthesized by the chronoamperometric approach offer a feasible and adaptable foundation for high-performance, sustainable sodium-ion battery anodes.

Keywords: Sodium-ion batteries, graphene oxide, single doping, dual doping, chronoamperometric method, electrochemical performance.

ÖZET

Sodyum İyon Piller İçin Grafen Esaslı Yeni Nesil Anot Malzemelerinin Üretimi ve Performanslarının İncelenmesi

MohammedMustafa Hussein M ALMARZOGE

Metalurji ve Malzeme Mühendisliği Anabilim Dalı
Doktora Tezi

Danışman: Prof. Dr. Metin GENÇTEN

Sodyum iyon pilleri (SIBs), sodyumun küresel bolluğu ve uygun maliyeti nedeniyle son yıllarda önemli ölçüde ilgi görmüştür. Bu da onları lityum bazlı pillere umut verici bir alternatif haline getirmiştir. Bu tez, klor (ClGO), kükürt (SGO), nitrojen (NGO) ve nitrojen ile kükürt karışımı (N–S–GO) ile katkılanmış grafen oksit tozlarının sentezi için basit, tek adımlı, uygun maliyetli, büyük ölçekli uygulamaya uygun ve çevre dostu bir kronoamperometrik yöntem sunmaktadır.

Dopingli tozların yapısını ve morfolojisini kapsamlı bir şekilde analiz etmek için XRD, Raman spektroskopisi, XPS, FT-IR, BET, SEM ve TEM kullanılmıştır. Yapılar, yaklaşık 2-3 katmandan oluşan, 46-50 nm boyutlarında ve 18-19 sp^2 karbon halkasına sahip nanokristal alanlara sahip, birkaç katmanlı grafen oksitten oluşuyordu. Doping, ClGO için (6.7˚A), SGO için (3.38˚A), NGO için (6.8˚A) ve N-S-GO için (6.58˚A) kadar katmanlar arası mesafenin artmasına yol açarak Na^+ iyonlarının hareketliliğini ve tutulmasını artırdı. XPS incelemesi, heteroatomların başarılı kovalent bağlanmasını doğrulayarak, C–Cl, Cl-Ox (x = 2, 3, 4), C–SO_x–C (x = 2, 3) ve C–N bağlarının oluşumunu sağladı. Aynı zamanda, yüzey reaktivitesini ve kusur yoğunluğunu artıran oksijenli gruplar da dahil edildi. Raman ölçümleri,

artmış bozukluk oranlarını (I_D/I_G) ortaya çıkardı, bu da sodyum depolaması için uygun daha fazla kusur bölgesine işaret ediyor.

Elektrokimyasal deneyler, katkılı tüm GO anotlarının sodyum depolamada önemli ölçüde etkinlik gösterdiğini ortaya koydu. Tek DGO için iki farklı elektrolit sistemi kullanıldı. ClGO, SGO ve NGO'nun başlangıç özgül deşarj kapasiteleri, 0.1 C akım hızında, Na^+ difüzyon katsayısı (D_{EIS}) sırasıyla yaklaşık $6.8x10^{-13}$ cm^2 s^{-1}, $4.01x10^{-12}$ cm^2 s^{-1} ve $4.86x10^{-12}$ cm^2 s^{-1} olarak hesaplanan karbonat bazlı elektrolitte 1 M $NaPF_6$ kullanıldığında sırasıyla 389.7, 256.7 ve 200 mAh g^{-1}'dir.

Eter bazlı elektrolit kullanan ClGO, SGO ve NGO anotlarının 415, 733 ve 952 mAh g^{-1} ve (D_{EIS}) değerleri sırasıyla yaklaşık $7,49x10^{-10}$, $1,67x10^{-9}$ ve $6,03x10^{-10}$ cm^2 s^{-1} olarak hesaplanan değerlerle karşılaştırıldığında. N-S-GO, yalnızca eter bazlı elektrolit kullanılarak anot olarak test edildiğinde, başlangıçta 457 mAh g^{-1} özgül deşarj kapasitesi gösterirken, (D_{EIS}) döngü öncesinde yaklaşık 4.4×10^{-11} cm^2 s^{-1} ve döngü sonrasında 3.2×10^{-10} cm^2 s^{-1} olarak hesaplandı, bu da etkili iyon taşımacılığını göstermektedir. Sentezlenen anot, eter bazlı bir elektrolit kullanıldığında 2C, 5C ve 10C gibi yüksek hızlarda üstün performans göstererek (SIBs) için yüksek hızlı bir anot malzemesi olarak uygunluğunu kanıtlamaktadır.

Uzun süreli döngü değerlendirmeleri, 2C hızında 100 döngüden sonra yaklaşık %100 kapasite korumasıyla dikkate değer bir kararlılık gösterdi. Geliştirilmiş elektrokimyasal performans, heteroatom dopinginin sinerjik etkilerinden, artırılmış katmanlar arası mesafeden ve kusur kaynaklı psödokapasitans'tan kaynaklanmaktadır. Bu etkiler birlikte iletkenliği ve Na^+ iyonlarının difüzyon hızını artırmaktadır. Bu çalışma, kronoamperometrik yöntemle sentezlenen heteroatom katkılı grafen oksitlerin, yüksek performanslı, sürdürülebilir sodyum iyon bataryası anotları için uygulanabilir ve uyarlanabilir bir temel sunduğunu göstermektedir.

Anahtar Kelimeler: Sodyum iyon pilleri, grafen oksit, tek doping, çift doping, kronoamperometrik yöntem, elektrokimyasal performans.

1

INTRODUCTION

1.1. Energy Storage Systems (ESSs).

Over the extended term, discovering superior alternatives to fossil fuels is crucial if we aim to utilize energy sources that are inexhaustible. According to Worldometer, our current oil reserves are projected to last only 47 years [1]. We need to swiftly find a suitable replacement, perhaps within our lifetime, given the urgency posed by global warming and the challenges associated with petroleum and coal. This has prompted an investigation into ecologically sound and limitless resources obtained from energy sources that are renewable such as wind, water, solar, geothermal, as well as tidal energies [2]. The advancement of Energy Storage Systems (ESSs) is crucial to tackle this issue. These systems store power generated from sources like wind or solar to be utilized during periods when these sources aren't actively generating- such as when the wind stops, sunlight is obstructed, or during night-time. Batteries serve as a key component of this system, enabling the storage and subsequent use of this stored energy.

Among energy storage systems, batteries have been identified as an efficient technology thanks to their high energy conversion efficiency, comparatively compact dimensions, and rapid reaction capabilities**.** There are two main types of batteries:

1. Non-rechargeable (primary batteries) employ electrochemical reactions during discharge but are unable to reversed through supplying electricity. Hence, they are thrown away after single discharge. The primary batteries comprise 20% of the battery market.

2- Rechargeable (secondary batteries) as the primary batteries employ electrochemical reactions during discharge, but this kind are capable of being charged again by applying a voltage to reverse the chemical reactions.

The most popular rechargeable batteries are lead–acid, nickel–based, and lithium–ion. Among the array of ESSs, lithium-ion batteries (LIBs) presently reign as the predominant solutions for energy storage [3]. The sodium-ion battery (SIBs) has unmistakably entered the race toward commercialization. In general, rechargeable batteries operate through the movement of ions during the charging and discharging processes. The fundamental components of battery cells include the cathode, anode, a porous separator situated between them to prevent short circuits, and the electrolyte.

1.1.1. Sodium-Ion Batteries (SIBs).

Several countries propose the Net Zero Emissions (NZE) strategy by reducing the environmental effect of using non-sustainable power sources, such as fossil fuels, with renewable power sources [4]. Let’s take into account only the transportation sector, and from the transportation sector only (vehicles), how many batteries will be needed to achieve the NZE goal, which, according to the World Economic Forum, is that the global need for electrical vehicles (EVs) will be about 2 billion in 2050 [3]. We're aware that LIBs reign as the primary power source among ESSs for EVs [3], [6]. Given that approximately 25% of annually consumed lithium minerals are used in the battery industry [7]. If we consider that only 60 million cars are produced annually, each requiring roughly 1.4 kg of lithium carbonate, the total annual demand will surpass current lithium carbonate production by fivefold [8], [9]. The sales of LIBs have witnessed remarkable growth, escalating from around US$ 7 billion in 2009 to an estimated 54.6 billion U.S. dollars in 2021, with a projected valuation of approximately 257 billion U.S. dollars in 2030 [10]. Additionally, the uneven distribution of lithium resources worldwide grants countries with significant lithium reserves a monopoly in the battery manufacturing market. Moreover, the reliance on rare and potentially toxic elements like cobalt in LIBs poses challenges. These factors, coupled with the anticipated surge in demand, may lead to short-term price hikes and market fluctuations. Consequently, finding alternatives to LIBs becomes an imperative goal to replace the costly and finite resources of lithium with more abundant and cost-effective alternatives.

Researchers have shifted their focus to SIBs due to various advantages they offer. Sodium, being the 4th most abundant element in the Earth's crust, ensures a cost-effective material and mitigates the potential for monopolizing the battery manufacturing market. Additionally, the use of inexpensive aluminum as a current collector at both the anode and cathode is feasible because sodium does not form alloys with aluminum. This feature not only enhances safety during transportation but also enables the battery to discharge into a near-zero state of charge (SOC) [11], [12]. One major advantage of transitioning from manufacturing LIBs to SIBs is the compatibility with existing infrastructure used in LIB manufacturing processes. This seamless transition allows for the utilization of the same manufacturing infrastructure, streamlining the shift from LIBs to SIBs without requiring significant retooling or substantial alterations in production facilities [13].



Figure 1.1 Advancement in Graphene-Based Nanocomposites As High-Capacity Anode Materials for Sodium-Ion Batteries [14].

Despite sodium's lower theoretical capacity (1165 mAh g^{-1}) compared to lithium (3860 mAh g^{-1}). SIBs can still play a crucial role in various applications that prioritize relatively lower energy density and longer lifespan. This makes SIBs suitable for a wide range of scenarios where high energy density is not the primary concern, but durability and cost-effectiveness are key considerations [15].

1.1.1.1. Graphene in SIBs

Concerns associated with increasing energy demand, limitations about fossil resources, and political instability have prompted the swift development of diverse intermittent renewable and cleaner energy alternatives [3], [6], [16], [17]. The drive to achieve NZE by prioritizing environmental sustainability has also accelerated research and development in energy storage and transportation electrification. It is known that the global need for (EVs) will be about 2 billion in 2050 [5], and currently LIBs occupy a predominant position in the realm of such (ESSs) [18]. Unfortunately, approximately one-fourth of the annual lithium mineral consumption is known to be dedicated to the battery industry [7]. It has been anticipated that if the 60 million vehicles produced globally per year get substituted by plug-in hybrid vehicles, each of which requires nearly 1.4 kg of lithium carbonate, the entire per year need could reach roughly 420,000 tons, which is more than 5 times present lithium carbonate production [9]. It is imperative to address challenging issues regarding lithium supply, such as the uneven distribution of resources on Earth, logistic problems, and price instabilities [19]. Therefore, a proper replacement LIBs is an essential goal for sustainable energy supply and storage in the future.

SIBs are promising alternatives to traditional LIBs since they show comparable chemical properties and work on almost the same underlying principles as LIBs due to their affordability and plentiful supply of sodium [20], [21], [22], [23]. Therefore, considerable advantages exist in the industrial shifting of LIBs towards SIBs. At first, SIBs offer potential advantages in terms of cost, resource availability, safety, and environmental impact [19], [24], [25]. SIBs are compatible with a lighter, more cost-effective, and oxidation-resistant aluminum current collector on the anode side, which leads to safer transportation and usage [12], [26]. The higher standard electrode potential of Na (−2.71 V) compared to Li (−3.04 V) versus the standard hydrogen electrode (SHE) facilitates the advancement of high-voltage SIBs. Conversely, the electrochemical properties of Na^+ exhibit similarities with those of Li^+.

The efficient operation of SIBs depends on the use of active materials in their electrodes. Significant research has focused on developing anodes that offer

high performance, safety, and cost-effectiveness to enable wider adoption in various applications. The nano-structured anode materials enable the exposure of more active sites and shorten the ion transport path by increasing the specific surface area or reducing the domain size to improve the specific capacity and rate performance of SIBs which benefits ion diffusion and electrode structural integrity [21]. Functional carbon-based materials with diverse structures have attracted significant attention in SIBs, such as reduced graphene oxide [27], [28], [29], [30], graphene quantum dots [31], three-dimensional doped graphene [32], holey graphene oxide [33], petroleum cokes [34], carbon black [35][36], 3D porous carbon [37], sodium-graphene oxide composite [38], carbon microspheres [39], carbon nanofibers [40], and hard carbon [41], [42], [43], [44], in view of the fact that carbon-based materials have excellent chemical stability, well-developed porous structure, high conductivity, outstanding mobility, and short diffusion length [45], [46].

A key challenge for SIBs arises from the intrinsic properties of sodium ions; Since Na^+ ions are 55% larger than Li^+ ions, the electrode materials typically used in LIBs cannot be used for SIBs. This size disparity can affect the structural compatibility and overall performance of the conventional LIBs electrode materials in the sodium-based systems, making it necessary to explore and develop new materials for the transition of Na-driven technologies in the near future [29].

Graphite, a common anode material used in commercial LIBs with a theoretical capacity of 372 mAh g^{-1}, proves to be ineffective for SIBs due to its unsatisfactory theoretical capacity of only 35 mAh g^{-1} [47]. The mean reason for it that the Na^+ ion needs an interlayer distance of ~ 3.7 Å for the introduction of sodium ions, while the interlayer distance of graphite is only ~ 3.35 Å [48], [49], [50]. Hence, for carbon-based anode electrochemical processes, increased interplanar spacing is critical for dependable and rapid Na^+ insertion and extraction. Despite the limited capacity of two-dimensional carbon materials, efforts have focused on enhancing both the reversibility of intercalation and the number of reversible Na^+. These efforts include heteroatom doping, creating surface defects, increasing interlayer distance, adding surface functionalities, and adjusting the number of layers in carbon materials such as graphene [51], [52], [53].

When it comes to the mechanism lying behind the Na^+ ion storage in carbon materials, two main processes are involved: the surface-induced capacitive process (SCP) and the diffusion-controlled intercalation process (DIP). SCP happens when Na^+ ions attach to tiny voids and surface features (like defects and surface functional groups), allowing for quick movement and a capacitor-like behavior [54]. Meanwhile, DIP involves the Na^+ ions moving in and out of the graphite layers. Defective carbon structure is leading to higher specific capacity because the imperfections (vacancies or irregularities) create additional sites for Na^+ ions to be absorbed. Electrode-electrolyte reaction activity can be improved by the introduction of new functional groups on the carbon material's surface [55], [56].

Heteroatom doping, being a straightforward and effective functionalization approach, significantly influences electrochemical performance based on the specific form of the doping. Basically, it is considered that some heteroatoms manifest as surface functional groups that act as key sites for the adsorption and desorption of electrolytes. These groups also play a vital role in electrochemical redox reactions, greatly improving the capacity for Na^+ storage. This enhancement is essential for optimizing the performance of energy storage devices. On the other hand, the other part of the heteroatoms is thought to occupy lattice carbon sites, which can expand the spacing of graphitic microcrystallites and modify the electronic structure of carbon, improving diffusion dynamics [57]. Therefore, heteroatom doping of carbons is considered a straightforward method to enhance Na^+ ion storage, and its mechanism should be well understood by examining the effects of different dopants on the carbonaceous matrix.

As we mentioned, additionally introduced new functional groups which seems that doping can make all the improvements in need into the carbon-based material and enhance the electrochemical performance.

It is well known that the capacity of carbon materials can be enhanced through various strategies, including heteroatom doping [58], [59], [60], creating surface defects [61], [62], introducing surface functional groups, increasing d-spacing [51], [52], [53], customizing the number of layers of carbon-based materials like graphene [51], [52], [53] and even by using different electrolyte systems [63], [64] Especially, incorporating heteroatoms into the carbon framework has been shown

to enhance the electrochemical performance of carbon materials by increasing the number of active sites, thereby facilitating greater Na^+ insertion and improving specific capacity [65]. Also, recent studies have demonstrated that glyme-based electrolytes generally exhibit superior electrochemical performance compared to conventional carbonate-based electrolytes in SIBs, with this advantage strongly influenced by the nature of the electrodes and the formation and solid electrolyte interphase (SEI) formation dynamics. For example, Cohn et al. [66] evaluated a highly crystalline few-layered graphene capable of functioning as an ultrafast layered Na^+ anode in a 1M $NaPF_6$-diglyme system, in which a diglyme solvent shell encapsulated Na^+ and promoted ion insertion. Glyme-based electrolytes are known to enable the co-intercalation of solvated Na^+ ions into graphite, forming ternary graphite intercalation compounds (t-GICs) [63], [67]. A study presented by Seh et al., who showed 1 M $NaPF_6$ in diglyme to result in high reversibility, related to the formation of a stable SEI [68], [69]. Moreover, diglyme facilitates sodium intercalation as $Na^+(diglyme)_2$ complexes in graphite anodes, boosting graphite's capacity from 35 mAh g^{-1} in carbonate electrolytes to over 100 mAh g^{-1} in diglyme, despite graphite's typical inactivity in SIBs [69], [70], [71]. Therefore, diglyme may serve a promising electrolyte solvent by enabling reversible sodium intercalation in soft carbon and graphite, forming stable interfaces, and offering good compatibility with sodium salts and electrode materials in SIBs.

It's worth noticing that numerous methods has been employed to obtain carbon-based materials with heteroatoms such as hydrothermal synthesis [72], chemical vapor deposition (CVD) [73], ball milling [74], heat treatment and/or pyrolysis [61], [75], ball milling [26], and templating [76] techniques. Each doping method comes with its own advantages and disadvantages, such as high operating temperatures, the risk of hazardous gas formation, low yield, high cost, edge-specific doping, difficulty in controlling the doping process, and the presence of significant impurities. Additionally, many of these methods involve multiple complex steps, making the overall process less efficient. An evaluation of the synthesis techniques for heteroatom-doped graphene and graphene oxide in the literature also concludes that they often involve complex, multi-step processes requiring demanding conditions, such as the use of hazardous chemicals, high temperatures, and inert atmospheres [77], [78], [79]. Therefore, the preparation of

graphene oxide using simpler processes and green synthesis methods under room temperature and more practical conditions would offer a significant advantage. The chronoamperometric method is a single-step, environmentally friendly technique that has been previously utilized for the production of graphene oxide derivatives under mild conditions [80], [81], [82], [83], [84], [85].

The dopant effect on the electrochemical performance of the anode could be summarized as:

I. Chlorine Doping

Electron conductivity is enhanced when doped heteroatoms, acting as either p-type electron acceptors or n-type electron donors, penetrate the graphene framework and create structural defects [86]. In addition, chlorine is frequently selected over carbon as a doping element due to its greater atomic radius as well as higher electronegativity [87]. The chemical activity of graphene is further enhanced by the negative charges generated on carbon atoms by the chlorine atoms that are covalently linked to it. Chlorine heteroatom doping of graphene results in p-type defects in the graphene framework that boosts its electrical conductivity up to 2.5 times more than undoped counterpart [88].

II. Sulfur Doping

Sulfur atoms can replace carbon atoms in the graphene lattice or attach to the edges and defect sites [89]. This doping can create structural defects and modify the electronic structure of graphene oxide [90]. Therefore, adjusting the electronic structure can enhance the electrical conductivity of graphene oxide, which in turn reduces the energy barriers for Na-ion diffusion within the electrode, leading to improved charge transport properties during Na-ion intercalation and greater structural stability [91].

The greater ionic radius between sulfur and carbon (Sulfur: 102 pm, compared to Carbon: 77 pm) is favorable for increasing the interlayer spacing of carbon layers. A greater layer space may dramatically boost the rate of Na^+ insertion and extraction as well as maximize SIB storage capability. The increased capacity is derived from the more active reaction locations after sulfur doping, which gives more sites to absorb Na^+ [62].

Sulfur doping with high sulfur content was studied by a research group. They found that because of the high S percentage inside this composite, as high as 26.9% a high specific capacity of 516 mAh g^{-1} was obtained combined with relatively poorer cycling stability which is hardly due to the higher sulfur quantity inside [55]. Subsequent to the aforementioned observations, research indicates that the introduction of approximately 2.5% Sulfur into graphene can yield a remarkable reversible capacity of 291 mAh g^{-1}, alongside exceptional rate capabilities of 127 and 83 mA h g^{-1} at charging/discharging rates of 2.0 and 5.0 A g^{-1} within 3.8 and 1 minute, respectively, in addition to demonstrating considerable stability during cycling [92]. Sulfur doping holds significant relevance for battery applications due to sulfur's status as an electrochemically active element capable of engaging in reversible reactions with sodium [93].

III. Nitrogen Doping

N-doping enhances the electrical conductivity of graphene, facilitating electron transport, while also expanding the specific surface area to provide additional binding sites [94]. The presence of nitrogen atoms, which possess greater electronegativity than carbon atoms, results in an increased affinity for sodium ions, thereby significantly improving sodium absorption during the charging process [62], [95]. Furthermore, the substantial interlayer distance facilitates the movement and retention of Na^+ ions within the graphene layers, thereby enhancing the rate performance significantly [96], [97]. Due to the aforementioned factors, Nitrogen stands out as the most thoroughly examined heteroatom [94]. It is known that N-doping improves carbon’s electrical conductivity and specific surface area, increasing binding sites while enhancing electron transfer efficiency due to nitrogen's higher electronegativity compared to carbon. This results in better Na^+ absorption during charging. N-doped carbons also introduce carbon vacancy defects via heteroatoms like pyridine-N and pyridine-N oxide, creating electron acceptor states that capture electrons from sodium atoms. Additionally, the larger interlayer distance facilitates Na^+ ion transport and storage, boosting high-rate performance [62], [94], [95], [96], [97], [98], [99], [100].

1.2. Scope and aim of the thesis

The increased interest in SIBs in recent years has manifested in the commercialization of this type of battery. Commercial batteries primarily comprise a hard carbon active anode material. The synthesis of hard carbon requires high temperatures over prolonged periods, along with the necessity of an inert atmosphere. We synthesized a simpler alternative that can be achieved in one step, without the need for an inert environment. Doping takes place concurrently during this phase.

This method is utilized to synthesize three types of singly doped graphene oxide (sulfur, chlorine, and nitrogen) and one dual-doped graphene oxide (N-S-GO).

Two distinct types of electrolytes are utilized during the optimization phase. To achieve this objective, various doping elements were incorporated into GO via chemical methods, followed by structural characterization using XPS, FT-IR, Raman, XRD, BET surface area assessments, and property analysis through SEM-EDS and TEM techniques.

The synthesized powders served as standalone active anode materials, without the addition of other active components, and were analyzed electrochemically through cyclic voltammetry (CV), electrochemical impedance spectroscopy (EIS), and galvanostatic charge-discharge tests.

To the best of our knowledge, this is the first study on the use of ClGO, SGO, NGO on its on without adding any other component as anode for sodium ion batteries. Also, this is the first study on the use of ClGO, SGO, NGO and nitrogen-sulfur-dual-doped graphene oxide (N-S-GO) in combination with an ether-based electrolyte (diglyme) for SIBs.

This approach explores the impact of single and dual doping with the use of two different electrolytes on electrochemical performance using a simple chronoamperometric method, offering new insights for designing high-performance SIBs for future commercialization.

2

EXPERIMENTAL

2.1. Chemicals

Sulfuric acid, perchloric acid, and nitric acid were obtained from Merck and used as the reaction and doping medium. A graphite rod (Ø6X200E, 99.9%, 0.5 cm diameter) served as the working electrode and carbon source.

Sodium foil, 1.0 M $NaPF_6$ dissolved in a 1:1 (v/v) mixture of ethylene carbonate (EC) and dimethyl carbonate (DMC) with 10 vol.% fluoroethylene carbonates (FEC) as an additive, and 1.0 M $NaPF_6$ in 100% diglyme were used as received, without further purification, after being purchased from Sigma-Aldrich.

2.2. Preparation of single- and co-doped graphene powders

The synthesis of all single and dual-doped graphene oxide powders was conducted using the Gamry 1010B Potentiostat/Galvanostat through the chronoamperometric method. The chronoamperometric method employed a graphite rod as the working electrode, a platinum wire as the counter electrode, 5.0M acidic medium, and an Ag/AgCl (3.0 M KCl) as the reference electrode, appling a scan rate of 50 mVs^{-1} at room temperature.

The single doped graphene powders were synthesized utilizing 5.0 M concentrations of the respective doping elements in a supporting electrolyte: 5.0 M HNO_3 for nitrogen doping, 5.0 M H_2SO_4 for sulfur doping, and 5.0 M $HClO_4$ for chlorine doping, under an operating potential of 2.1 V.

The dual-doped graphene oxide powder (N-S-GO) was synthesized in a (1:1) (V: V) ratio using 5.0 M concentrations of each doping element, with an operating potential of 2.3 V.

The graphite rod functions as the carbon source in the electrochemical process, whereas the 5 M solution acts as the electrolyte. Electrolysis occurs upon the application of voltage, resulting in the oxidation of the graphite rod and the formation of graphene oxide (GO) powder. The acidic environment facilitates the oxidation process and serves as a dopant agent. The produced powder was filtered and washed multiple times to eliminate the acid solution from the synthesized powders, followed by drying at 90°C for 12 hours prior to characterization.

Table 2.1 Experimental Parameters Employed for Powder Synthesis Via The Chronoamperometric Method.

No.	Synthesized powder	Electrolyte	Operating potential (V)
1	SGO	5.0 M H_2SO_4	2.1
2	NGO	5.0 M HNO_3	2.1
3	ClGO	5.0 M $HClO_4$	2.1
4	N-S-GO	5.0 M HNO_3: 5.0 M H_2SO_4, 1:1 (v/v)	2.3

2.3. Coin Cell Preparation.

2.3.1. Single-DGO.

To prepare the anode slurry, a high-speed magnetic stirrer was used to thoroughly mix 80 wt. % Single DGO, 10 wt. % carbon black, and 10 wt. % polyvinylidene difluorides (PVDF) with N-methyl pyrrolidone (NMP) for two hours.

After the slurry had homogenized over a magnetic stirrer for 2 hours. The film was created using Dr. Blade by putting the homogenized slurry over copper foil with a 100µm coating thickness. To dry the film and eliminate the NMP, the film was left in a vacuum oven overnight at 120°C. The electrodes were made by cutting electrode film into 16-mm-diameter discs.

Two electrolyte systems were employed: (i) Carbonate-based electrolyte of 1.0 M $NaPF_6$ dissolved in a 1:1 (v/v) mixture of ethylene carbonate (EC) and dimethyl

carbonate (DMC) with 10 vol.% fluoroethylene carbonates (FEC) as an additive, and (ii) Ether-based consist of 1.0 M $NaPF_6$ in 100% diglyme. For the purpose of separation, the glass microfibre Whatman GF/D was utilized, and sodium metal was appointed to serve as both the counter electrode and the reference electrode.

2.3.2. Dual doped (N-S-GO).

Electrode material was made utilizing the produced powder with a view to testing the anode performances of the dual-doped GO. A mixture with a ratio of 7:2:1 of dual-doped GO, carbon black, and PVDF was added to N-methyl pyrrolidone (NMP) for electrode preparation. After the slurry had homogenized over a magnetic stirrer for 2 hours. The film was created using Dr. Blade by putting the homogenized slurry over copper foil with a 100 μm coating thickness. To dry the film and eliminate the NMP, the film was left in a vacuum oven overnight at 120°C. The electrodes were made by cutting electrode film into 16-mm-diameter discs. A single type of electrolyte was used in N-S-GO half-cells (consisting of 1.0 M of $NaPF_6$ in 100% diglyme). For the purpose of separation, the glass microfibre Whatman GF/D was utilized, and sodium metal was appointed to serve as both the counter electrode and the reference electrode.

2.4. Electrochemical Measurements

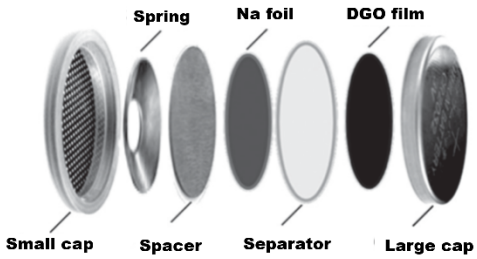


Figure 2.1 Coin-Cell Configuration.

Electrochemical measurements were carried out using a CR-2032-coin half-cell type assembled in an argon-filled glove box with O_2 and H_2O less than 1 ppm. All assembled cells were brought to testing after 12 hours.

At different scan rates, cyclic voltammetry (CV) was conducted throughout a potential range of 0.02–3V (versus Na/Na^+) at different scan rates. Furthermore, electrochemical impedance spectroscopy (EIS) was conducted using an AC signal

with a 5 mV amplitude (vs. Na/Na^+) throughout a frequency range of 0.1–10,000 Hz. The EIS spectrum was analyzed using an equivalent circuit model. EIS results were employed to estimate the Na^+ diffusion coefficient. CV and EIS measurements were conducted using a Gamry Interface 1010B potentiostat/galvanostat.

The cycling performance at a 2 C rate, along with the rate performance at various C rates (0.1 C, 0.5 C, 1 C, and 2 C), was evaluated through galvanostatic charge-discharge measurements within a controlled voltage range of 0.02–2.5 V (vs. Na/Na^+) using a NEWARE unit.

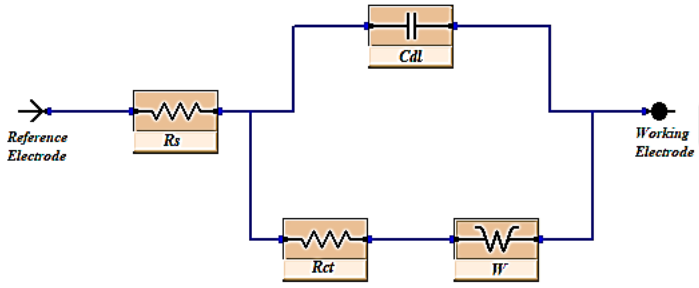


Figure 2.2 Equivalent Circuit Model for Fitting Process of EIS.

2.5. Characterization of DGO powders.

The structural information for the as-prepared DGO powder was investigated by X-ray diffraction (XRD) analysis using the Malvern PANalytical X'Pert PRO instrument (anode material: Cu and wavelength: CuKα1 = 1.54059 Angstrom).

The chemical states of the surface atoms of the prepared DGO powder were determined by X-ray photoelectron spectroscopy (XPS) analysis, where a thermo-scientific K-Alpha model (Kα = 1468.3 eV, Avantage 5.934 software) device was used.

Raman spectra using WiTec Alpha (532 nm) Raman spectra were recorded to calculate the number of sp^2 carbon rings, nanocrystalline domain, average number of layers, and the presence of defects.

Using the Perkin Elmer Spectrum 100, a Fourier transform infrared spectrometer (FT-IR) examination was carried out to determine the presence of functional groups that contained oxygen, chlorine, sulfur, and nitrogen.

The specific surface area and the pore size distribution of the prepared powder were inspected by the Brunauer-Emmett-Teller (BET) by nitrogen adsorption/desorption measurements at 77 K (ASAP 2020 V4.00 C (V4.00 C H). In order to determine

the Brunauer-Emmett-Teller (BET) specific surface area and the pore size distribution of the powder that were manufactured, nitrogen adsorption/desorption experiments were carried out at 77 degrees Kelvin (ASAP 2020 V4.00 C (V4.00 C H).

Using a Zeiss EVO LS 10 (Au-Pd coating) and a Thermo Scientific Apreo 2 S LoVac, respectively, a scanning electron microscope (SEM) that was equipped with energy-dispersive X-ray spectroscopy (EDS) was utilized to study the morphology and elemental composition of the DGO powder that had been formed. The HITACHI FHT7700 was utilized to acquire images from a transmission electron microscope (TEM).

3

RESULTS

3.1 Characterization Single DGO Powder

3.1.1. XRD

The effect of heteroatom doping on the graphene oxide layers was examined using XRD analysis. The d-values and the spacing between the graphene oxide layers were obtained using the Bragg equation ($n\lambda = 2d \sin\theta$). The XRD pattern shown in (Figure 3.1) displays a diffraction peak for ClGO and NGO powders at a 2θ value of ≈ 13°, which corresponds to the (002) plane of graphene oxide [101], [102]. While this peak is not present at SGO powder. The characteristic peak of graphite typically appears at 2θ ≈ 26°, also corresponding to the (002) plane, but indicating a smaller interlayer distance due to its more ordered layered structure [101]. This dominant primary peak observed at ≈ 26° in all produced powder is indicative of a high oxidation level on the graphitic surface [103]. This peak is indicating a smaller interlayer distance due to its more ordered layered structure [101].

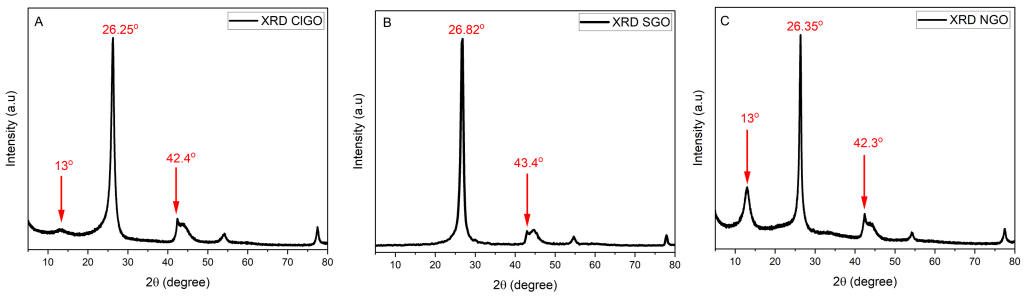


Figure 3.1 XRD Pattern of (A) ClGO, (B) SGO, and (C) NGO-Based Powders.

There are no peaks related to pure sulfur, nitrogen, or chlorine observed. The broadening diffraction peak at around 2θ of 42.3° is related to the edge doping of graphene oxide [104]. In the case of ClGO and NGO powders, the d-spacing—which determines the distances between the graphene oxide layers— was calculated

and found to be equal (d = 6.58 Å for ClGO and 6.8 Å for NGO). While in the case of SGO, the d-spacing didn't increase significantly (d = 0.338 nm) indicating the partial restoration of sp^2 carbons.

We can conclude that when chlorine and nitrogen atoms replace carbon in the lattice, they disrupt the regular GO structure, causing local distortions and increasing the spacing between layers. This expanded interlayer distance may facilitate better Na^+ transport and storage, improving electrochemical performance [105]. In other words, the XRD pattern of ClGO and NGO indicates that chlorine and nitrogen doping increased the interlayer distance significantly, which will enhance the diffusion-controlled intercalation process (DIP) storage mechanism. While in the case of SGO, the presence of a peak at 42.3 indicated only edge doping was accomplished in SGO powder, which means that the surface-induced capacitive process (SCP) will be the main storage mechanism in SGO anodes.

3.1.2. XPS

The chemical states of the surface atoms of the prepared DGO powders were determined by XPS analysis.

3.1.2.1. ClGO XPS

The chemical state of ClGO was determined using XPS, and the survey scan (Figure 3.2.A) revealed the presence of C, O, and Cl, confirming the high purity of the resulting powder. The successful incorporation of chlorine dopants into the GO network was confirmed through the XPS survey spectra, which revealed the presence of Cl atoms in the structure. This finding is further supported by the SEM mapping results, which demonstrate the uniform distribution of Cl throughout the GO, providing additional evidence of effective doping. In XPS analysis, ClGO powder exhibited functional groups, including oxygen and chlorine, on its main structure. The C1s and C2s XPS spectra of ClGO (Figure 3.2.B) showed peaks around 284.3 eV, corresponding to –C–C– bonding [106], and peaks around 286.6 eV, indicative of C–Cl bond formation [87]. The detection of distinct C–Cl bond peaks in the XPS spectra provides clear evidence of the successful incorporation of Cl heteroatoms into the graphene lattice structure, confirming the effectiveness of the doping process and the chemical bonding between chlorine and carbon atoms within the material. (Figure 3.2.C) shows $Cl2p_{1/2}$ spectrum. The spectrum displayed

peaks at approximately 199.69 eV, indicating –C–Cl bonding [107]. Peaks attributed to $Cl2p_{3/2}$, corresponding to ClO_x (ClO_2, ClO_3, and ClO_4) were observed at around 207.58 eV[108], [109]. However, peak in the O1s spectrum (Figure 3.2.D) were more intense than in the $Cl2p_{1/2}$ spectra, suggesting higher doping of Cl-containing oxygenated groups in synthesized powder. O1s Peaks at 532.29 eV attributed to C = O bonds. The absence of a reduction step in this synthesis method likely preserves the oxygen-rich functional groups on the surface of the powdered ClGO and this retention of oxygen-containing groups may play a crucial role in enhancing the material's surface chemistry, potentially contributing to improved functionality [87]. Even though oxygen-containing groups decrease the electronic conductivity, they are beneficial for enlarging the interlayer distance [110].

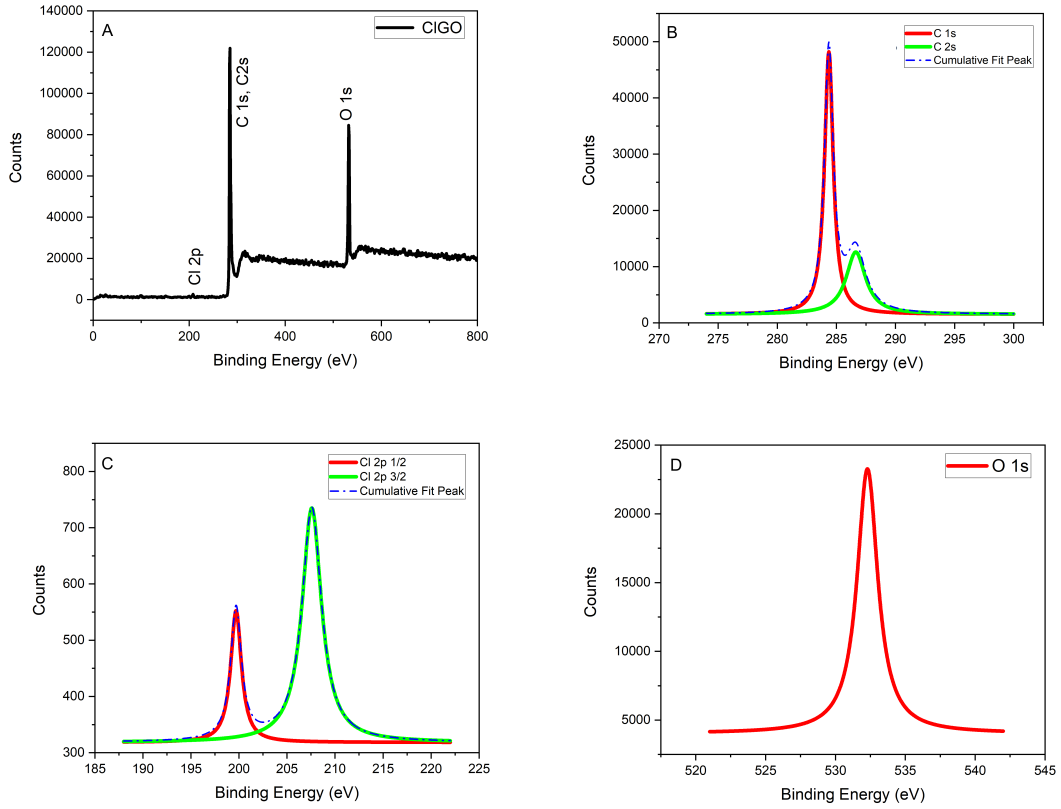


Figure 3.2 XPS Analysis of ClGO Based Powders.

3.1.2.2. SGO XPS

The chemical states of the surface atoms of the prepared SGO powder were determined by XPS analysis. The survey XPS spectrum of SGO powder (Figure 3.3.A) shows the related spectrums of C1s, O1s, and S2p with an atomic percentage of 80.48, 17.75, and 1.77%, respectively.

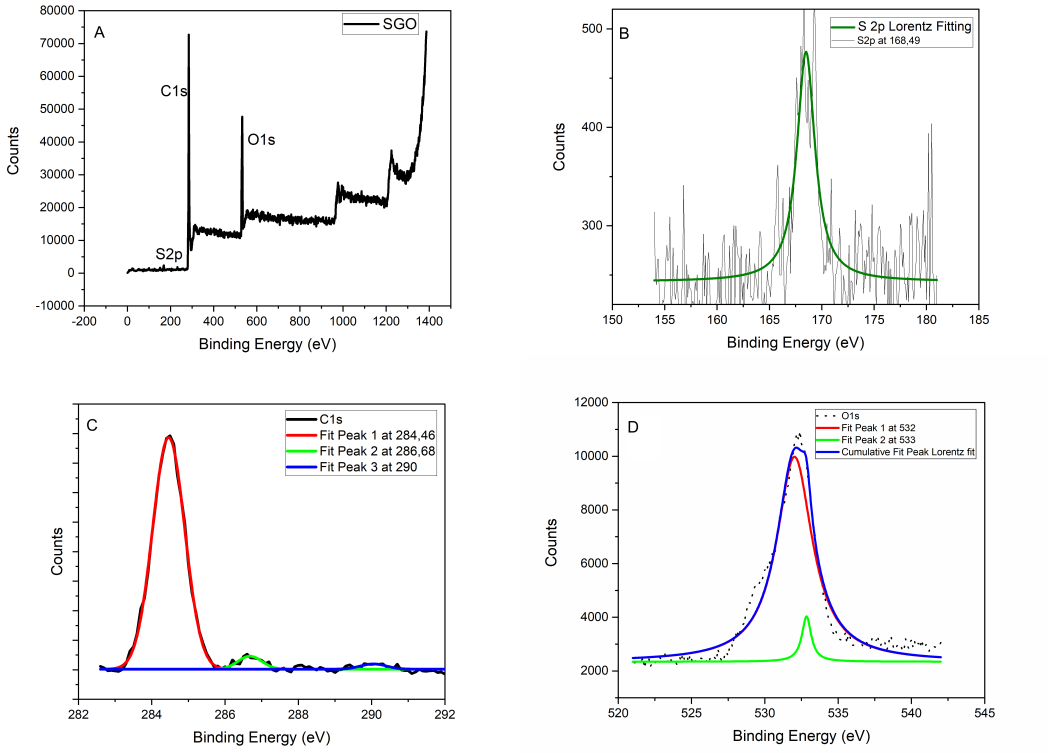


Figure 3.3 XPS Analysis of SGO Based Powders.

SGO powder had oxygen and sulfur including functional groups on its main structure in XPS analysis. XPS spectrums (Figure 3.3.B) the peaks that were related to the formation of –C-SOx-C- (x = 2, 3) were determined at S2p at 168.49 eV, from which is caused by sulfur incorporated into disordered carbon successfully [111], [112]. The C1s spectrum (Figure 3.3.C) located at 284.5 eV, can be resolved as follows: C-C and C=C at 284.46 eV[113], C-O at 286.68 eV, and O-C=O at 290.0 eV indicating that most of the C atoms remained in the conjugated honeycomb lattice, like sp2 C in the graphite [64], [106], [112], [114], [115], [116], [117]. The O1s XPS spectra of the prepared SGO powder reveal distinct peaks (Figure 3.3.D). Notably, peaks are observed around 532.11 eV, with a two-tip configuration at approximately 532 eV and 533 eV. These peaks are associated with C–O and O=C–O groups, respectively.

3.1.2.3. NGO XPS

The spectrum survey of NGO (Figure 3.4.A) shows the related spectrums of C1s, O1s, and N1s with an atomic percentage of 72.251, 26.554%, and 1.195, respectively.

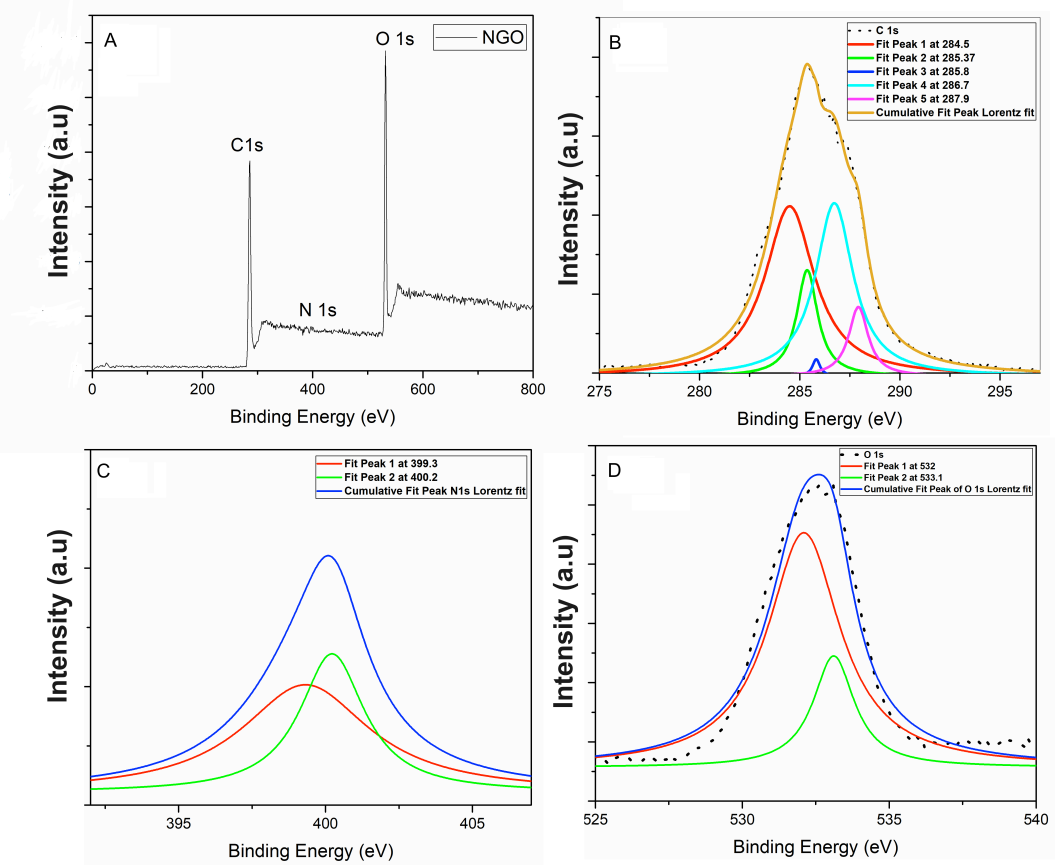


Figure 3.4 XPS Analysis of SGO Based Powders.

Upon analyzing the C1s spectra of the NGO in (Figure 3.4.B), it was deconvoluted into five peaks. The main peaks correspond to C-C (sp^2 hybridized) at 284.5 eV, sp^3 C at 285.37 eV, N-C (sp^2 hybridized) at 285.8 eV, C-O at 286.7 eV, and C=O at 287.9 eV. The N-C (sp^2 hybridized) peak at 285.8 eV indicates that nitrogen atoms are covalently bonded to the primary carbon structure [118], [119], [120], [121]. Analysis of the XPS spectra of NGO (Figure 3.4.C) revealed the presence of both pyridinic N and pyrrolic N, as indicated by the characteristic peaks observed at approximately 399.3 eV and 400.2 eV [111], [115], [118], [119]. It is known that pyridinic and pyrrolic N atoms located at the edge of the graphitic layer are more effective in adsorbing exotic atoms and enhancing the Na-ion storage capacity. While graphitic N atoms bring extra free electrons to the structure, leading to an increase in the electric conductivity [122]. When it comes to O1s XPS spectra

of prepared NGO powder (Figure 3.4.D) the peaks obtained at around of 532.41 eV with a peak of two tips around of 532 eV and 533 eV are attributed to the groups of C-O and O=C-O, respectively [120].

3.1.3. FT-IR.

FT-IR spectroscopic analysis was performed to identify the oxygen and doped elements containing functional groups present in the synthesized DGO powders.

3.1.3.1. ClGO

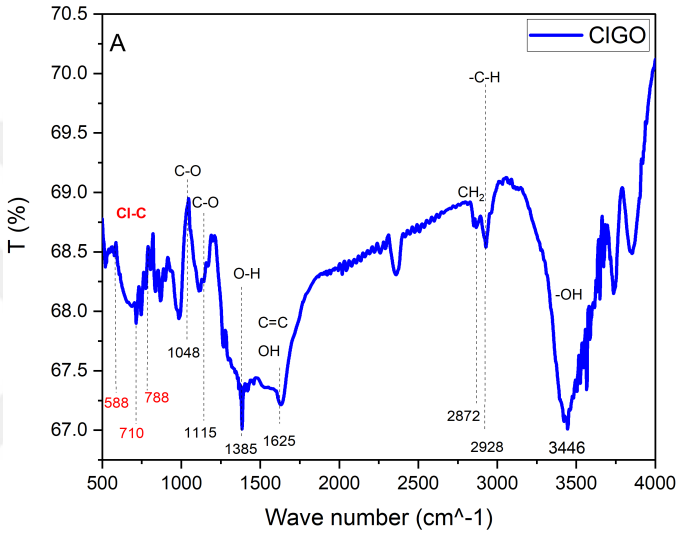


Figure 3.5 ClGO FT-IR Spectrum.

In Figure 3.5, the Fourier transform infrared (FT-IR) spectra of ClGO exhibits peaks at 588, 710, and 788 cm^{-1}. These peaks match the stretching vibrations of C−Cl, which verifies the effective insertion of chlorine atoms into the powder that has been produced [123]. There are bands of absorption that are associated with oxygen-containing functional groups, such as C-O or C-O-C at 1048 cm^{-1} and C-O at 1115 cm^{-1}[123], [124], [125]. Also 1115 cm^{-1} peak may overlap with C-C band [126]. The other peaks at 1385 cm^{-1} correspond to O-H stretching vibration [125], and 1625 cm^{-1} to C=C and -OH stretching vibration also [127], [128]. Peaks at 2872, and 2928, are ascribed to CH_2 stretching vibration [129], and -OH stretching vibration at 3446 cm^{-1} [123], [130], [131]. It clearly shows the successful doping and creating of the functional groups into the structure.

3.1.3.2. SGO

An FT-IR spectroscopic study was carried out in order to determine the characteristics of the oxygen- and sulfur-containing functional groups that were present in the manufactured SGO powder (Figure 3.6).

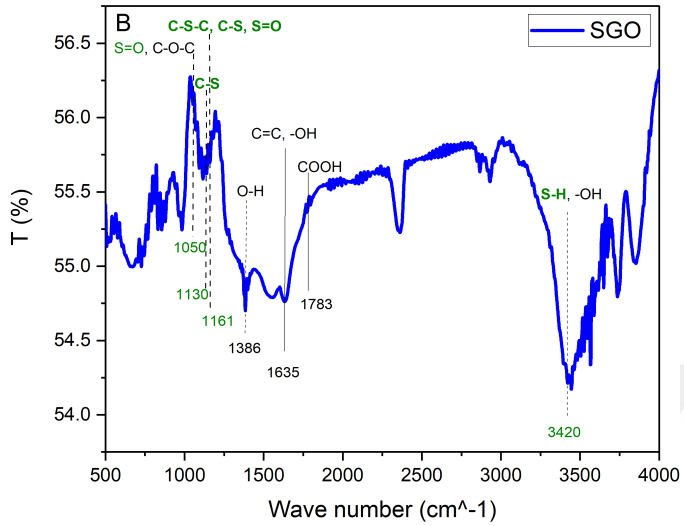


Figure 3.6 SGO FT-IR Spectrum.

Within the existence of S=O stretching modes originating from sulfate and sulfonate groups, the peak that is centered at 1050 cm^{-1} is indicative of their presence. The C-O-C stretching vibration that originates from epoxy functionality [127]. overlaps with this peak of the stretching vibration.The peak that is centered at 1050 cm-1 may possibly potentially relate to the C-O stretching vibration in addition to the S=O stretching modes that originate from the sulfate and sulfonate groups, which indicates that there may be an overlap in this particular spectral region [131]. It is most likely that bonds of C–O–C and S=O are present at 1161 cm^{-1}, which corresponds to the frequency [132]. There is a deformation vibration of O-H that is responsible for the band that is located at 1386 cm^{-1} [125]. The presence of the C=C stretching band led to the band at 1635 cm^{-1}, which overlapped with the absorbed hydroxyl group in graphene oxide domains [127]. This was due to the presence of the hexagonal aromatic ring. It was determined that the presence of carboxyl functional groups COOH was associated with the peak that was found at approximately 1738 cm^{-1} [127]. Further identification of the state of sulfur (S) was accomplished by identifying unique peaks at 3420 cm^{-1}. These peaks originate from the in-plane bending vibration of S–H bonds [133].

3.1.3.3. NGO

FTIR spectrum analysis was conducted to characterize the oxygen and nitrogen-containing functional groups in NGO powder, as illustrated in (Figure 3.7).

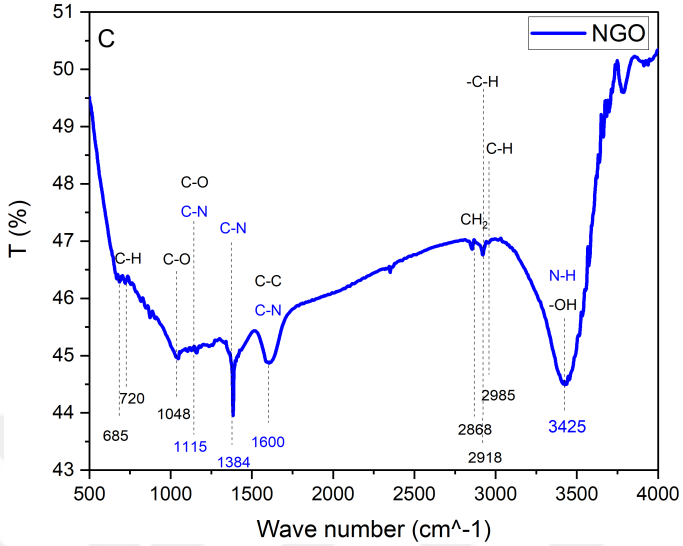


Figure 3.7 NGO FT-IR Spectrum.

The FT-IR spectrum revealed absorption peaks at 720 and 685 cm^{-1}, which are associated with aromatic C-H deformation [124]. The peak at 1048 cm^{-1} is attributed to C-O absorption bands, signifying the presence of oxygen-containing functional groups [124], [131]. A weak peak around 1115 cm^{-1} suggests the presence of vibrations from C-O bonds, which likely overlap with C-N bonds [125], [126]. The sharp deformation vibration of O-H peak located at about 1384 cm^{-1} [125]. The peaks near 1600 cm^{-1} are linked to the overlapping vibrations of C=C and C=N bonds, indicating that nitrogen atoms have been effectively integrated into the sp^2 networks of the graphitic structure [125], [134]. The small peaks at 2879 cm^{-1} in the spectrum are attributed to the stretching vibrations of CH_2 groups [124]. The peaks at 2985 cm^{-1} correspond to the symmetric and asymmetric stretching vibrations of C-H bonds [134]. The broad and intense peaks around 3425 cm^{-1} are associated with the stretching vibrations of O-H bonds [124], [125], [126] and N-H bonds [125], resulting from adsorbed H_2O molecules and the incorporation of nitrogen functional groups into graphene oxide (GO), respectively. The FT-IR spectra of NGO demonstrate the formation of various oxygen functionalitie along with the replacement of carbon atoms with nitrogen, which can play a significant role in electrochemical redox reactions with improving the Na^+ ion storage capacity.

3.1.4. Raman spectroscopy

Raman spectroscopy used to obtain information on the structural, optical, and defect-related changes induced by elemental doping into GO powder (Figure 3.8).

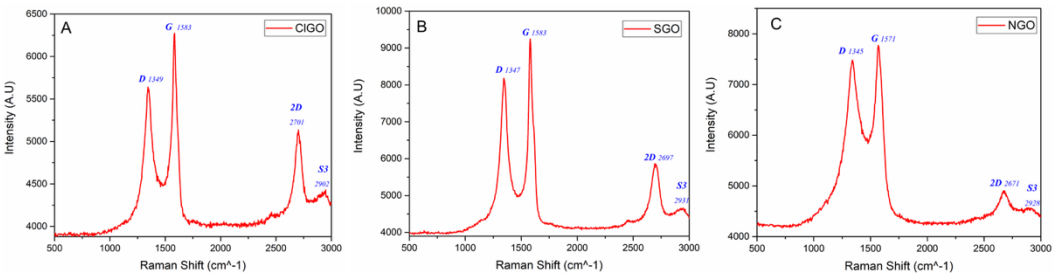


Figure 3.8 Raman Spectra of (A) ClGO, (B) SGO, and (C) NGO Based Powders.

Raman spectrum showed that all DGO powder contains four bands marked as D, G, 2D and S3 bands. The D band activates in the presence of defects, is a defect-induced double-resonant Raman feature linked to the symmetrical breathing vibrations (A1) of the hexagonal carbon rings [135], [136], [137], [138]. This band signifies disorder in crystalline materials and points to defects related to vacancies and grain boundaries [138]. The G band arises from the tangential in-plane stretching vibrations associated with the (E_{2g}) optical phonon of sp^2 C–C bonds, which is a common feature to all sp^2 carbon systems [49], [135], [138]. The (I_D/I_G) ratio obtained from the Raman spectrum reflects the level of defects and disorder introduced by nitrogen doping. This ratio is crucial for understanding how doping affects the material's structural integrity and electronic properties. Higher ratio of intensity (I_D/I_G) assigned to a higher ratio of defects and distortions [139]. This higher ratio is beneficial for existence of more active sites for Na^+ storage [140]. Optical properties of the GO can be interpretated according to that ratio too (I_D/I_G value closer to value of one show more transparent property) our prepared samples show optical transparency which is compatible with the TEM image results [141], [141], [142]. Intensity ratio (I_D/I_G) of ClGO, SGO, and NGO were found to be 0.9, 0.89, and 0.96, respectevily. which indicates the presence number of defect sites in all DGO, which may be caused by doping into the GO structure which will cause a structural distortion [139], and presence of defect-rich GO [143]. Also, all DGO must show optical transparency. The second order of D peak (2D) [136], [144], can be used to determine the layers number of the synthesized DGO as it is highly

sensitive to stacking of graphitic layers [49], since its result of a higher order process involving two phonons [137]. Backes et al. presented metrics to quantify the mean number of layers (N) depending on the I_{2D}/I_G ratio as follow [145]:

$$\mathbf{N = 1.04 \times \left(\frac{I_{2D}}{I_G}\right)^{(-2.32)}} \qquad \textbf{Equ. 1}$$

The I_{2D}/I_G ratio for ClGO was found to be 0.82 which indicates synthesized ClGO is of double layers (N = 1.64). While for SGO and NGO, this ratio was found to be 0.63 for both. That indicates synthesized SGO and NGO are both of few layers since (N = 3).

Another band, known as the S3 band (2902-2931 cm^{-1}), is a second-order peak derived from the D + G peak combination and is also present [138].

For a more quantified characterization of DGO using Raman spectroscopy, the nanocrystalline domain size (Lα) was calculated using the Tuinstra and Koenig equation (TK) (Equ. 2) [142].

$$\frac{I_D}{I_G} = \frac{C_\lambda}{L_\alpha} \qquad \textbf{Equ. 2}$$

According to the calculations, there were roughly 19 sp^2 carbon rings, and the calculated L_α value was about 49 nm for ClGO material. For SGO, L_α value of approximately 50 nm with sp^2 carbon rings around 19. In NGO the calculated L_α value was ~ 46 Nm, and the number of sp^2 carbon rings was calculated to be ~ 18. Table 3.1 shows a comparison of raman spectra results of ClGO, SGO, and NGO. Along with the FT-IR spectra, the Raman spectra indicated the presence of numerous defects introduced during the chronoamperometric synthesis process. These defects may enhance the electrochemical performance of DGO anodes for Na^+ ion storage.

Table 3.1 Raman Spectra Comparison Between ClGO, SGO, and NGO.

Synthesized powder	ClGO	SGO	NGO
Observed Raman Bands	D, G, 2D, and S3	D, G, 2D, and S3	D, G, 2D, and S3
D Band (cm^{-1})	1349	1347	1345
G Band (cm^{-1})	1583	1583	1571
2D Band (cm^{-1})	2701	2697	2671
S3 Band (cm^{-1})	2902	2931	2928
I_D/I_G Ratio	0.90	0.89	0.96
Optical Transparency	Yes (compatible with TEM images).	Yes (compatible with TEM images).	Yes (compatible with TEM images).
I_{2D}/I_G Ratio	0.82	0.63	0.63
Calculated Layer Number (N)	1.64 (≈ double layers)	3 (few layers)	3 (few layers)
Nanocrystalline Domain Size (Lα)	~ 49 nm	~ 50 nm	~ 46 nm
No. of sp^2 Carbon Rings	~19	~19	~18

3.1.5. BET

The analysis of the specific surface area, volume of pores, average size of pore, and distribution of pore sizes of the synthesized ClGO, SGO, and NGO powders was conducted using N_2 adsorption/desorption isotherms. The characterization was conducted using Brunauer Emmett-Teller (BET) gas adsorption measurements for DGO. The distribution of pore sizes for DGO assessed using with Barrett-Joyner-Halenda (BJH) approach. The N_2 adsorption isotherm

observed in (Figure. 3.9.A-C) identified as a type IV isotherm. This isotherm type indicates the existence mesopores within the material [99]. The pore size distribution curve of DGO (Figure 3.9.D-F) indicates that the predominant size range of mesopores falls between 2 and 40 nm, confirming the pore type as mesopores.

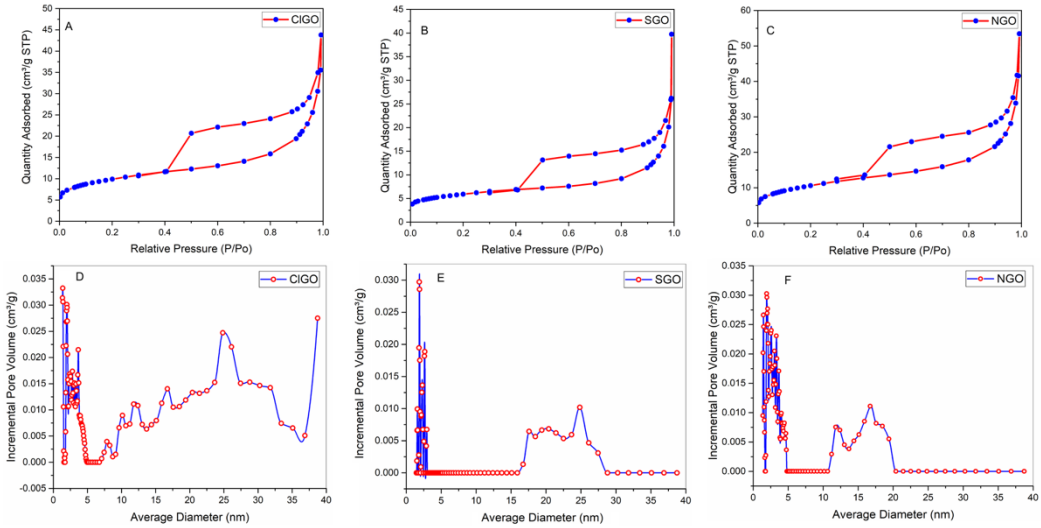


Figure 3.9 (A-C) Nitrogen Adsorption/Desorption Isotherms Curves, (D-F) The Corresponding Pore-Size Distribution Curves of ClGO, SGO, and NGO Powders, Respectively.

Table 3.2 BET Results of ClGO, SGO, and NGO.

Sample	Isotherm Type	Pore Type	Pore Size Range (nm)	BET Surface Area (m^2/g)	Pore Volume (cm^3/g)	Average Pore Size (nm)
ClGO	Type IV	Mesoporous	2–40	35.15	0.0677	7.71
SGO	Type IV	Mesoporous	2–40	20.9	0.061	11.75
NGO	Type IV	Mesoporous	2–22	38.03	0.0827	8.7

Furthermore, the specific surface area, volume of pores, average pore size, and the distribution of pore sizes were computed as illustrated in (Table 3.2). The porous structure of the DGO is anticipated to be beneficial for its use as an anode in SIBs. These characteristics are expected to create a 3D interconnected conductive network, aiding in efficient charge transfer. This setup is likely to enhance the electrochemical performance of the DGO material [118].

3.1.6. SEM-EDX

3.1.6.1. ClGO

The EDS elemental mapping of ClGO, presented in (Figure 3.10.A-E), clearly illustrates the homogeneous distribution of chlorine heteroatoms across the graphene oxide structure. Elemental mapping confirms the presence of Cl, C, and O atoms in the synthesized ClGO material. The analysis confirms the successful incorporation of chlorine atoms into the graphene oxide structure, with a measured chlorine atomic content of 1.15%, thereby validating the effectiveness of doping process.

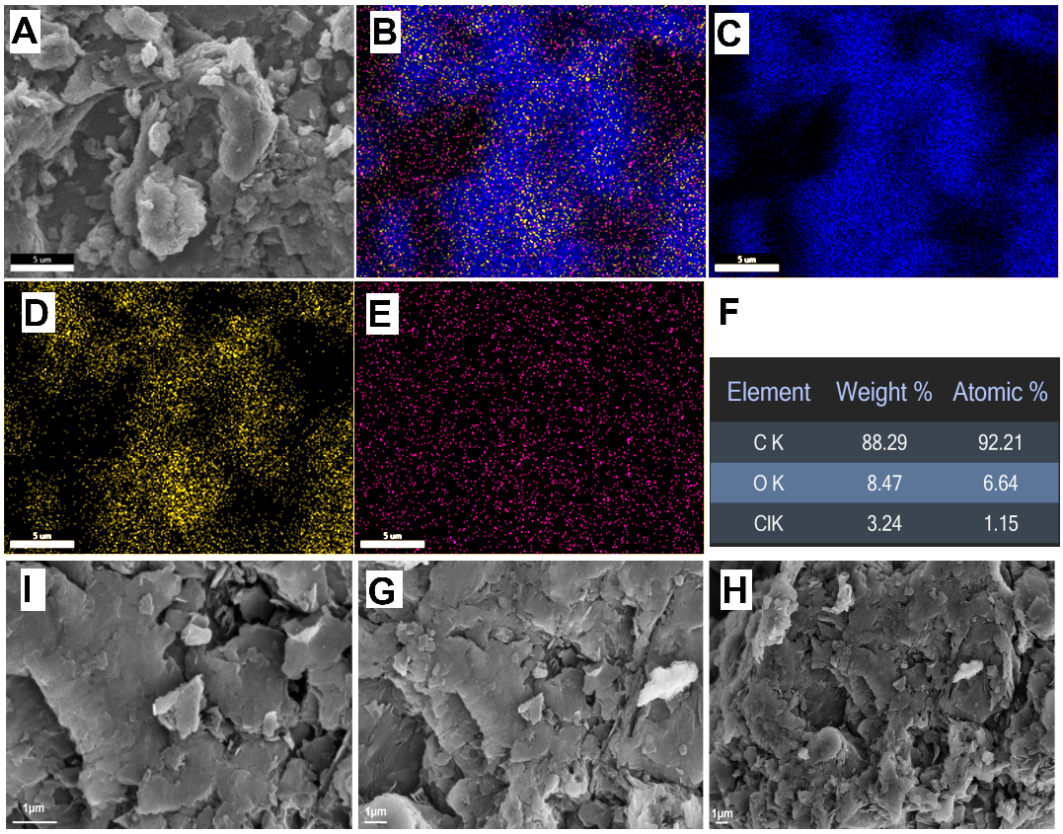


Figure 3.10 ClGO SEM- EDS Mapping (A) Area Selected for EDS, (B) All Elements, (C) Carbon, (D) Oxygen, (E) Chlorine, (F) Compositional Percentages, and SEM Images of ClGO Powder Captured From The Same Surface Area at Different Magnifications: (G) 40k×, (H) 20 k×, and (I) 10 k×.

The morphology of the synthesized ClGO was examined using SEM and TEM, with the resulting micrographs presented in (Figure 3.10.I-H). SEM micrographs captured at magnifications of 10kX, 20kX, and 40kX reveal that the ClGO powder consists of layered bundles arranged in a multi-layered structure. These bundles are closely stacked, leading to the formation of large, cohesive clusters. The layered morphology observed in the SEM images highlights the

structural integrity of the synthesized ClGO, which is characteristic of graphene-based materials and critical for applications requiring high surface area and robust conductivity.

3.1.6.2. SGO

The EDS elemental mapping of SGO (Figure 3.11.A-F) displays the distribution and compositional percentages of each element. Sulfur atoms are observed to be uniformly dispersed among the graphene oxide sheets, with an atomic ratio of 2%. This suggests the successful creation of chemically heteroatom S-doped graphene oxide. Both SEM images and corresponding EDS analysis confirm the presence of sulfur (S), carbon (C), and oxygen (O) within the SGO material.

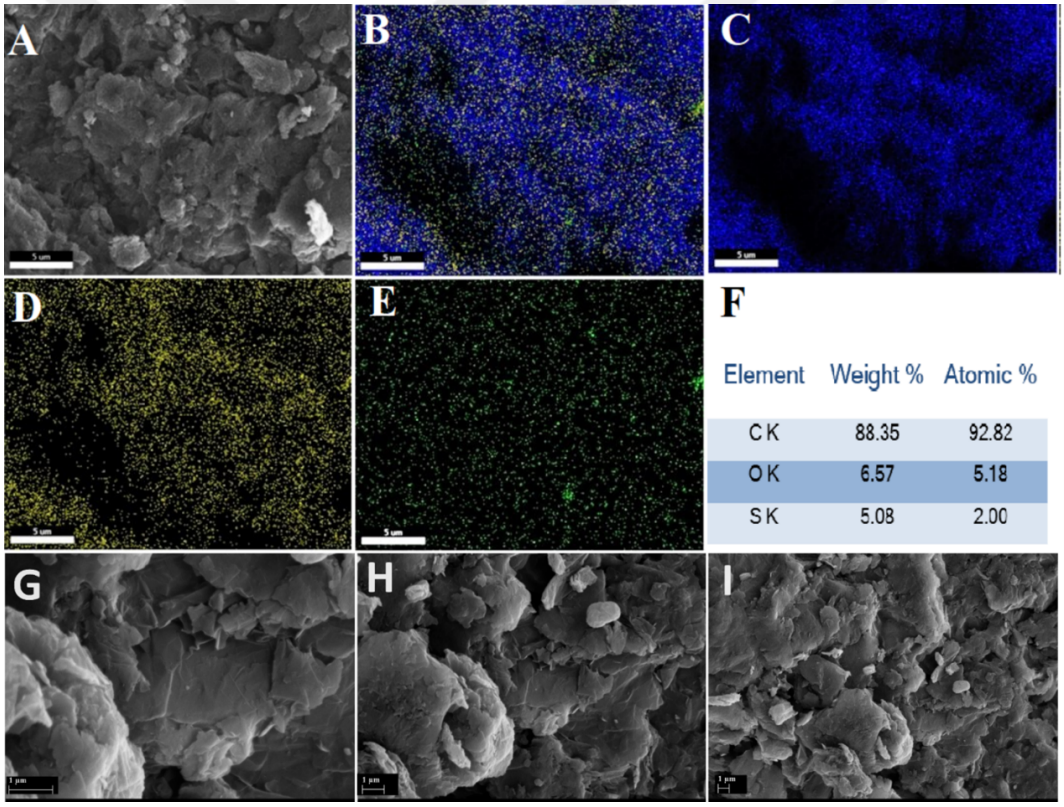


Figure 3.11 SGO SEM- EDS Mapping (A) Area Selected for EDS, (B) All Elements, (C) Carbon, (D) Oxygen, (E) Sulfur, (F) Compositional Percentages, and SEM İmages of SGO Powder Captured From The Same Surface Area at Different Magnifications: (G) 40k×, (H) 20 k×, and (I) 10 k×.

The morphology of the prepared SGO was explored using SEM and TEM. SEM images at various magnifications (10k×, 20k×, and 40k×) in (Figure 3.11.G-I) show the SGO powder exhibits bundled layers arranged in a multi-layered configuration, often forming large clusters.

3.1.6.3. NGO

Microstructural analysis of the NGO powder was conducted using SEM and TEM techniques. The SEM-EDS elemental mapping (Figure 3.12) indicates that the heteroatoms are uniformly distributed throughout the GO structure.

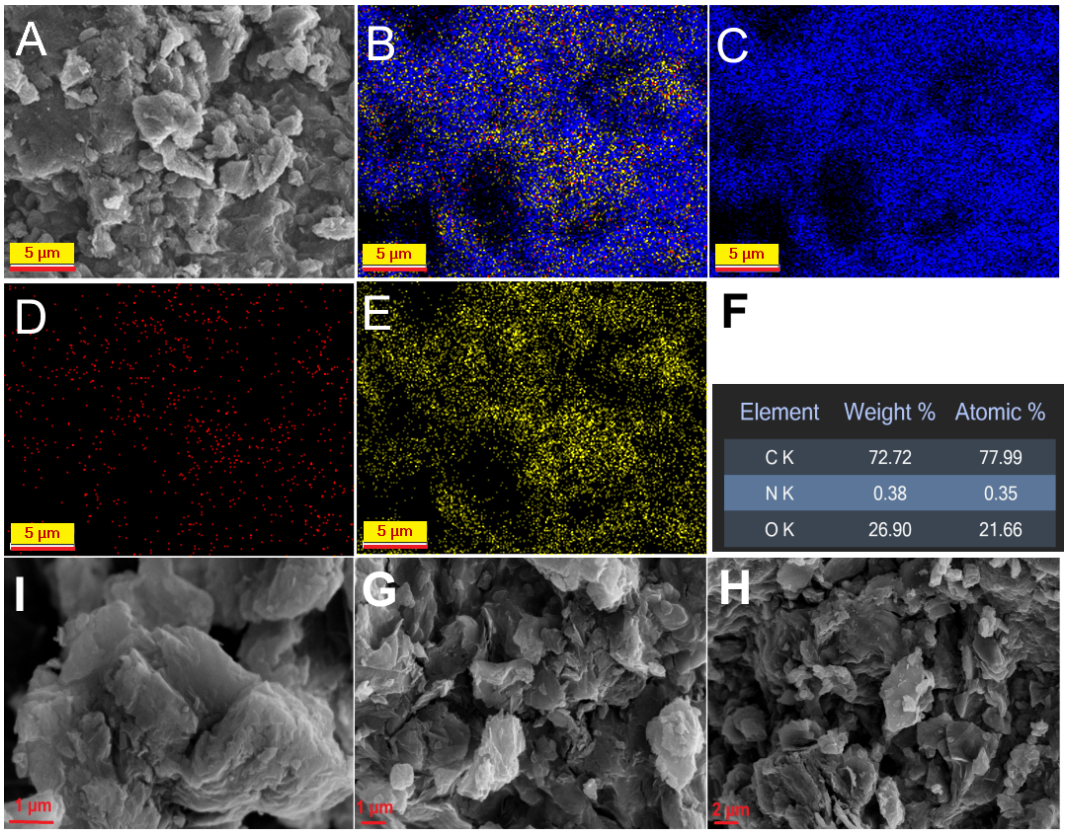


Figure 3.12 NGO SEM- EDS Mapping (A) Area Selected for EDS, (B) All Elements, (C) Carbon, (D) Oxygen, (E) Nitrogen, (F) Compositional Percentages, and SEM Images of SGO Powder Captured From The Same Surface Area at Different Magnifications: (G) 40k×, (H) 20 k×, and (I) 10 k×.

The SEM images, along with the corresponding EDS analysis, reveal the presence of nitrogen, carbon, and oxygen in the NGO, with a nitrogen atomic percentage of 0.35%. Additionally, SEM images of the electrochemically synthesized NGO at various magnifications (Figure 3.12.G-I) show that the NGO powder forms multi-layered bundles, leading to the formation of large clusters.

3.1.7. TEM

3.1.7.1. ClGO

TEM analysis, presented in (Figure 3.13), demonstrates the formation of ultrathin laminar layers of ClGO, distinguished by their high degree of transparency. The images also confirm the two-dimensional structure of the ClGO powder.

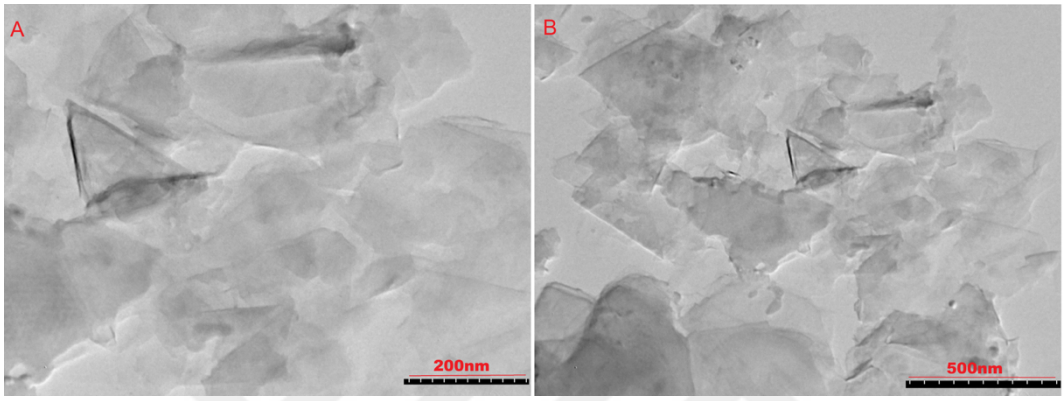


Figure 3.13 TEM Images of Synthesized ClGO.

3.1.7.2. SGO

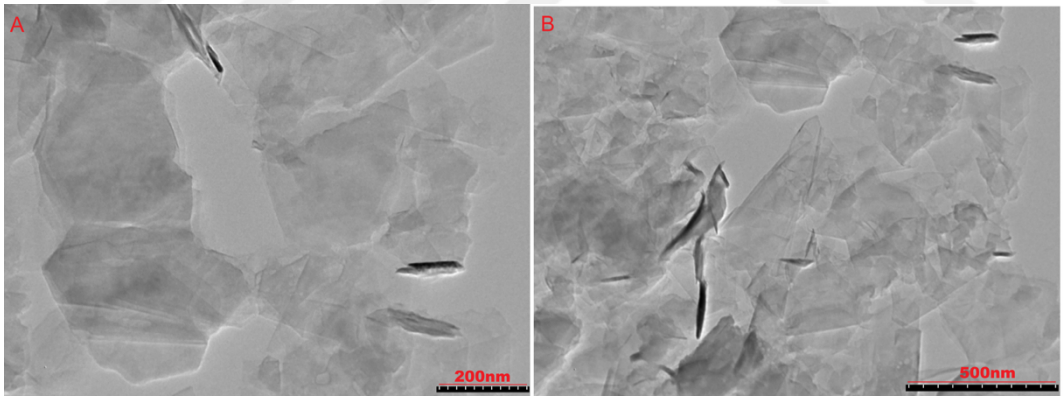


Figure 3.14 TEM Images of Synthesized SGO.

The TEM study depicted in (Figure 3.14) demonstrated ultrathin SGO layers characterized by exceptional transparency and a laminar shape. The regions with more transparency indicate the existence of thinner films composed of merely a few layers of stacked SGO. The TEM pictures revealed the development of a few-layered, two-dimensional (2D) structure within the SGO powder, corroborating the previously reported Raman estimates.

3.1.7.3. NGO

The micromorphology and microstructure of the NGO were further examined using TEM, with the images presented in (Figure 3.15).

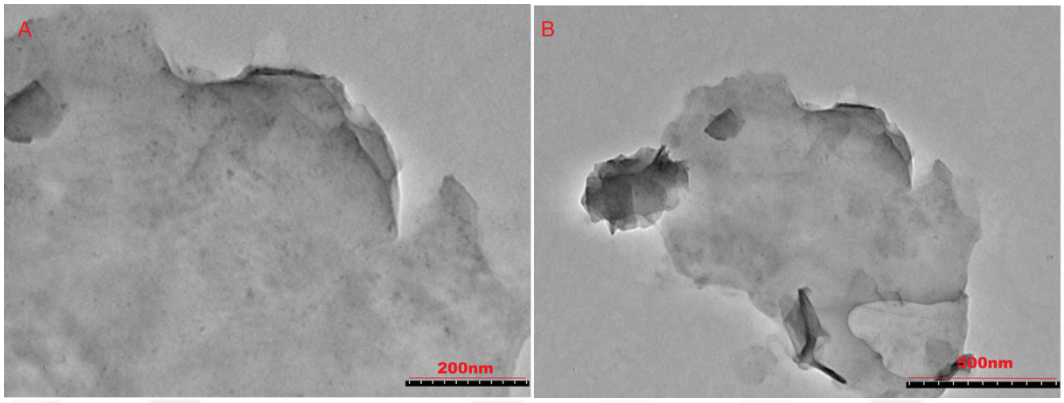


Figure 3.15 TEM Images of Synthesized NGO.

TEM analysis revealed the formation of ultrathin laminar NGO layers exhibiting high transparency. Additionally, the TEM images confirmed the development of a two-dimensional structure in the NGO powder. The synthesized NGO shows high transparency with stacking of graphitic layers about 3 layers which is compatible with the calculated number of layers using Raman spectroscopy test results along with its optical properties.

3.2. Characterization of Dual DGO (N-S-GO) Powder

3.2.1. XRD

The effect of heteroatom (N and S) doping on the graphene oxide layers was examined using XRD analysis. The XRD pattern (Figure 3.16) displays a diffraction peak for N–S–GO powder at a 2θ value of 13.44°, corresponding to the (002) plane. The dominant primary peak observed at 26.49° is indicative of a high oxidation level on the graphitic surface [103]. The d-spacing, which determines the distances between the graphene oxide layers, was calculated using the Bragg equation ($n\lambda = 2d \sin\theta$), and it was found to equal (d = 6.58 Å), which is sufficient for sodium ion intercalation/deintercalation. No peaks related to pure sulfur or nitrogen were observed. The broadening diffraction peak at around 2θ of 42.38° is related to the edge doping of graphene oxide [104]. These results show the successful increase in the d-spacing and the successful incorporation of the N, S doping elements.

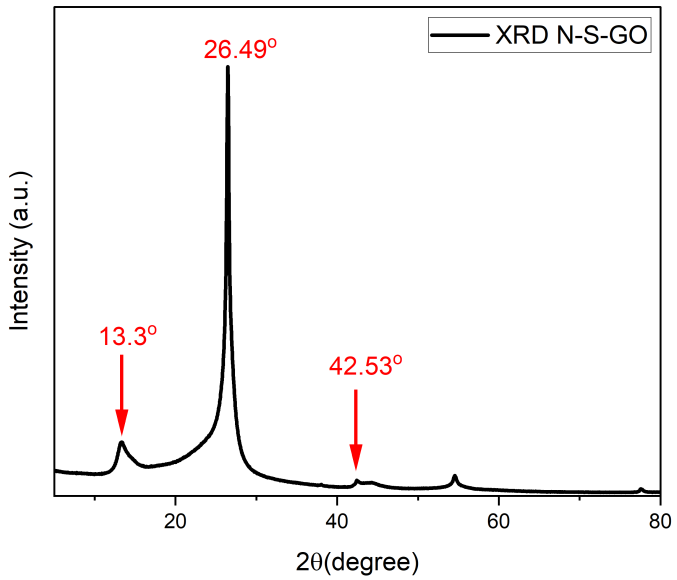


Figure 3.16 XRD Pattern of N-S-GO Based Powders.

3.2.2. XPS

To investigate the bonding of nitrogen and sulfur atoms to the graphene oxide sheets, X-ray photoelectron spectroscopy (XPS) measurements were performed. The survey scan (Figure 3.17.A) revealed a dominant graphitic C 1s peak at approximately 284.5 eV and an O 1s peak near 531 eV for the doped GO. Additionally, the XPS spectra confirmed the presence of S2p and N1s signals,

verifying successful doping. The presence of C, O, N, and S with an atomic percentage of 78.6%, 19.66%, 0.976%, and 0.746%, respectively, confirms the high purity of the resulting powder.

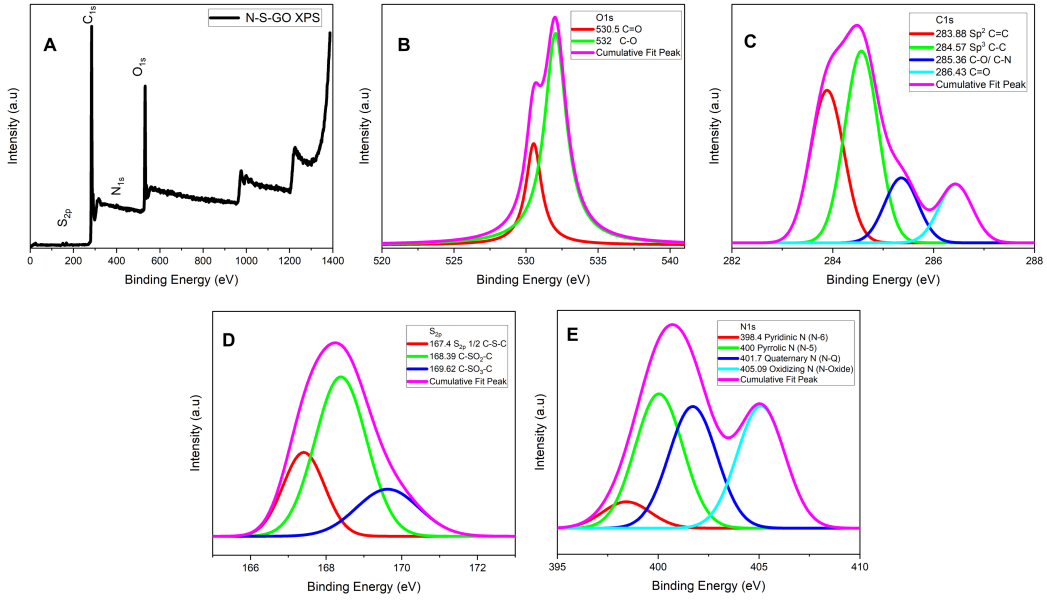


Figure 3.17 (A) Synthesized N-S-GO Powder XPS Survey, (B) O1s, (C) C1s, (D) S2p, and (E) N1s.

This finding is further supported by the SEM mapping results, which demonstrate the uniform distribution of N and S atoms throughout the GO, providing additional evidence of effective doping. O 1s spectra was deconvoluted into two peaks (Figure 3.17.B) at 530.5 eV, 532 eV corresponding to C-O, C=O, accordingly [120]. The C1s spectrum is located at 284.5 eV, which resolved into four peaks (Figure 3.17.C) related to C=C (283.88 eV), C-C (284.57 eV), C-O/C-N (285.36 eV), and C=O (286.43 eV) [146], [147]. Three independent peaks are obtained by peak fitting of the S2p high-resolution spectrogram (Figure 3.17.D). It shows that S has three different bonding forms related to C-S-C and oxidized sulfur -C-SOx-C- (x = 2, 3) bond peaks at 167.4 eV, 168.39 eV, and 169.62 eV, respectively [111], [112], [146], [148], [149] N1s spectrum contains four peaks of energy spectrum (Figure 3.17.E), which shows that the nitrogen atoms are in the presence of pyridinic nitrogen (398.4 eV), pyrrolic nitrogen (400 eV), graphitic nitrogen (401.7 eV), and oxidizing nitrogen at (405 ev) [147], [150], [151], [152], [153], [154]. By omitting the reduction step in this chronoamperometric synthesis method, the oxygen-rich functional groups on the surface of the N–S–GO powder are likely preserved, which may play a crucial role in enhancing the material's

surface chemistry and overall functionality [87]. Although oxygen-containing groups may reduce electronic conductivity, they simultaneously increase the interlayer spacing, which can facilitate the sodiation/desodiation process [110].

3.2.3. FT-IR

The infrared spectrum of N-S-GO is shown in (Figure 3.18). The figure illustrates that the prominent absorption band around 1583 cm^{-1} is associated with the stretching vibration absorption of the sp^2 (C=C) arrangement of graphene oxide [155], [156]. The band situated at 3432 cm^{-1} is associated with the stretching vibrations of (O-H) [157], (S-H) [158] and (N-H). The absorption peak observed at approximately 1500 cm^{-1} is attributed to the stretching vibration of the C-C bond. The vibrational absorption peaks are observed at 864 cm^{-1} (N-H) and 1035 cm^{-1} (N-C). Furthermore, the peak observed at 1044 cm^{-1} is associated with (N-C) and/or originates from sulfate groups (S=O)[159]. The vibration of (C-H) stretching occurs at 1407 cm^{-1}[160].

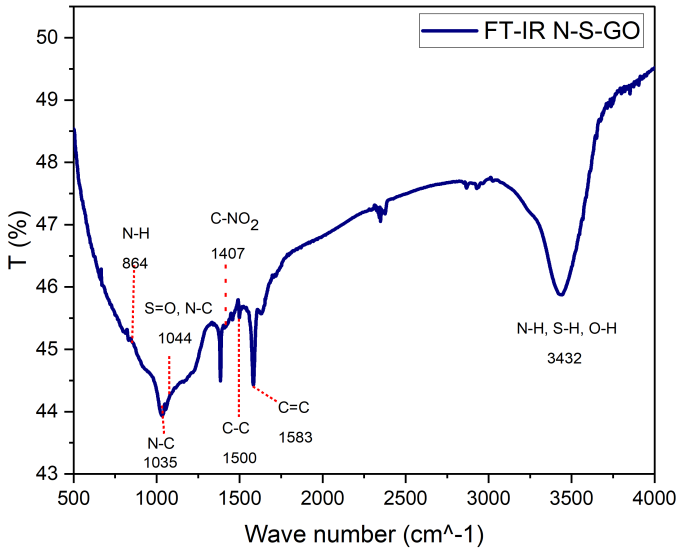


Figure 3.18 N-S-GO FT-IR Spectrum.

3.2.4. Raman spectroscopy

The Raman spectra of the prepared sample are presented in (Figure 3.19). The spectra show four peaks that are characteristic of the vibrational modes of the carbon-based material group denoted as D, G, 2D, and S3 bands. The peaks at around 1344 cm^{-1}, 1588 cm^{-1}, and 2702 cm^{-1} are related to D, G, and 2D bands characteristic of carbon-based material.

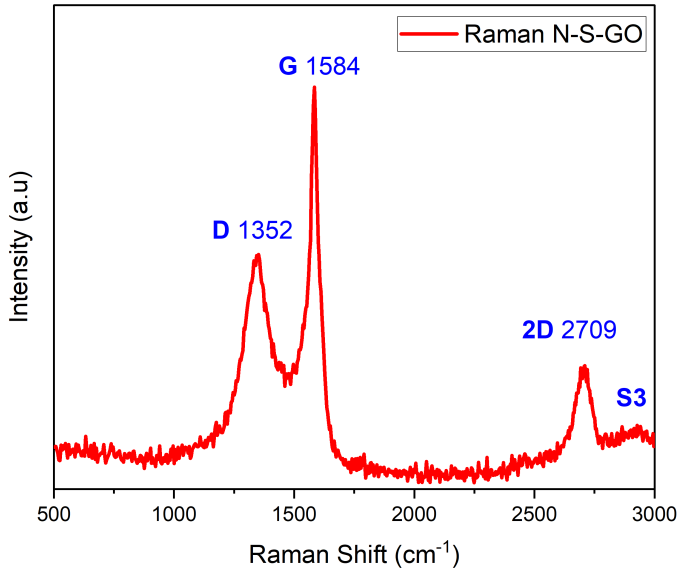


Figure 3.19 Raman Spectra Of N-S-GO Based Powders.

The same equation and procedure were used to calculate the nanocrystalline domain size (L_α), number of layers, sp^2 carbon rings, and estimated optical transparency of the synthesized powders. In our case, the (I_D/I_G) ratio of synthesized N-S-GO is about 0.92. It confirms two facts: (1) Our prepared N-S-GO powder should show optical transparency, which is compatible with the TEM image results. The calculated Lα value is ~ 48 nm, and the number of sp^2 carbon rings was calculated to be ~ 19. I_{2D}/I_G is 0.63, which indicates synthesized N-S-GO is of few layers (N = 3).

3.2.5. BET

Brunauer-Emmett-Teller (BET) N_2 adsorption-desorption isotherms were used to investigate the surface area and pore size distribution of the N-S-GO powder. The presence of a developed mesoporous structure is confirmed by the type IV isotherm observed in the N_2 adsorption curve (Figure 3.20.A) [99].

The pore size distribution (Figure 3.20.B) reveals a prominent mesopore range of 2–80 nm, indicating the formation of both mesopores and macropores, with mesopores predominantly between 20–50 nm and macropores exceeding 50 nm [161]. Upon comparing the synthesized S-doped GO [59], and N-doped GO [60] with the current study, it is noticeable that all three materials demonstrate a type IV N_2 isotherm, implying their dominant mesoporosity. While N-S-GO possess a broader spectrum of pore sizes, broadening into the macropore range (>50 nm).

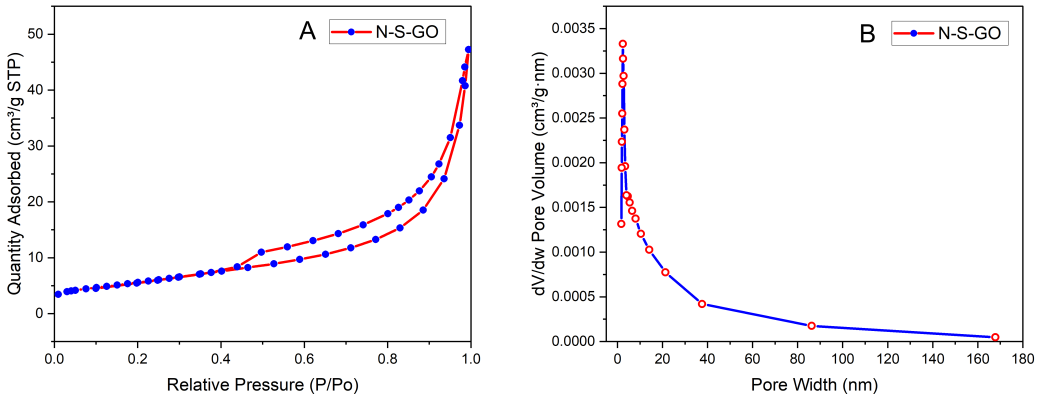


Figure 3.20 (A) Nitrogen adsorption/desorption isotherms curve, (B) The corresponding pore-size distribution curve of N-S-GO powder.

Conversely, ClGO, SGO, and NGO are mainly mesoporous. The presence of macropores acts as ion storage reservoirs and helps in reducing the diffusion resistance. Another advantage of the presence of macropore they allow the electrolyte and ions to penetrate deeply into the N-S-GO anode [162], [163]. The mesopores' existence offers more room for Na^+ ion insertion; mesopores in the N-S-GO structure boost the transit of Na^+ ions and increase the total ion storage capacity. By shortening the diffusion route length for Na^+ ions, such a porous framework optimizes ion transport kinetics [118]. Therefore, it can be anticipated that the N-S-GO's structure will produce a three-dimensional, interlinked conducting network that promotes its application as an intercalation anode in SIBs and facilitates charge transfer. The average pore size, pore volume, as well as BET surface area have been calculated to be 13.855 nm, 0.072666 $cm^3\ g^{-1}$, and 17.9345 $m^2\ g^{-1}$, respectively.

3.2.6. FE-SEM-EDX

Figure 3.21 presents FE-SEM micrographs and corresponding EDS elemental maps of the N–S–GO powder. The material exhibits a thin, sheet-like morphology with only minor agglomeration. EDS mapping reveals a homogeneous dispersion of the N and S dopants across the sheets, indicating effective doping. This uniform distribution is anticipated to enhance electronic conductivity and maintain the material's structural integrity during electrochemical charge–discharge cycles by preventing localized strains and uneven reactions that typically lead to structural degradation.

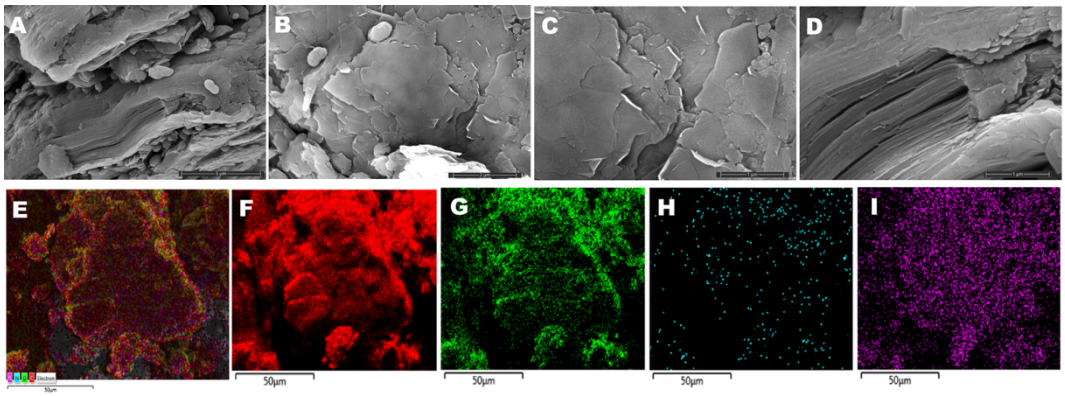


Figure 3.21 (A-D) FE-SEM Images of N-S-GO at Magnifications of (A) 25k×,(B) 50k×,(C and D) 100k× (E) Combined Elemental Mapping EDS Distribution Analysis; (F) Carbon; (G) Oxygen; (H) Nitrogen; (I) Sulfur.

3.2.7. TEM

TEM analysis (Figure 3.22) reveals the formation of a two-dimensional structure composed of a few ultrathin layers in the N–S–GO powder. This observation aligns with the average number of layers calculated using the method proposed by Backes et al. (Equ. 2), based on Raman spectroscopy data. Additionally, the layers exhibit optical transparency consistent with the estimated optical properties inferred from the (I_D/I_G) intensity ratio of 0.92, which closely approaches the value of 1.

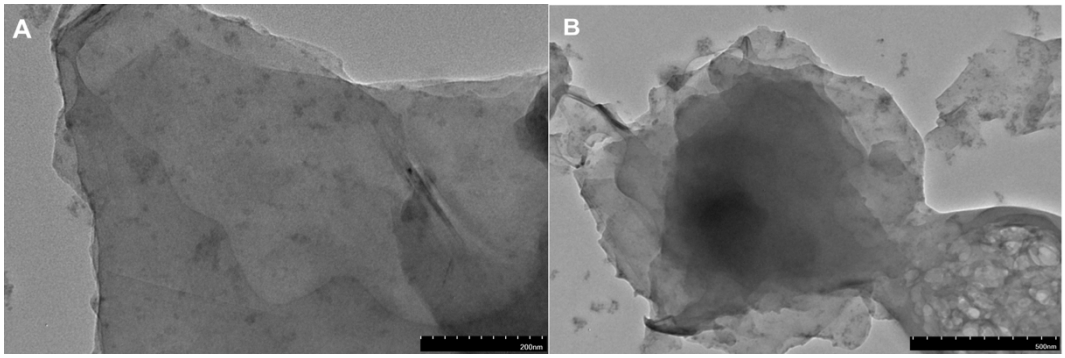


Figure 3.22 TEM Images of Synthesized N-S-GO.

3.3. Electrochemical Results of Single DGO Anodes using $NaPF_6$ in EC: DMC- with 10%FEC electrolyte.

3.3.1. CV

The Cyclic Voltammogram (CV) analysis was conducted to elucidate the Na^+ diffusion mechanism and electrochemical behaviors. The CV curves, as shown in (Figure 3.23.A-C), for three consecutive cycles (taken after the rate performance test) demonstrate excellent cyclability, which suggests that a stable (SEI) layer has been formed. The CV profile of the electrodes in question exhibit a remarkable degree of overlap in subsequent continuous scans, suggesting that the electrode is capable of efficiently inserting and extracting Na^+ ions while maintaining performance integrity. The high degree of overlap also reflects excellent reversibility, meaning that the electrochemical processes are efficient and consistent across cycles, which is a desirable characteristic for reliable energy storage applications.

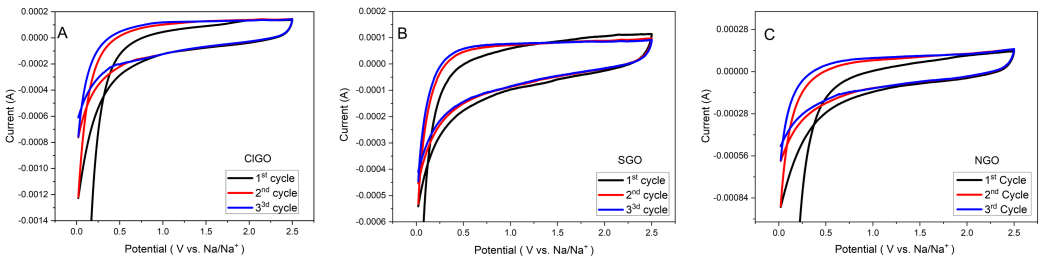


Figure 3.23 Three Consecutive Cyclic Voltammograms at 0.5 mV s^{-1} Scan Rate for: (A) ClGO, (B) SGO, and (C) NGO.

3.3.2. Rate performance results

The DGO anodes underwent galvanostatic charge-discharge (GCD) rate test, shown in (Figure 3.24). The rate performance properties of the DGO, were assessed by incrementally varying the current density from 0.1 C to 2 C.

The NGO half-cell anode demonstrated excellent cycle stability across all current densities, including the maximum of 2C. When the current density was reduced from 2 C back to 0.1 C, the discharge capacities of all DGO anodes returned to high values, indicating that their structure remained intact even after high-rate cycling. During the charging process, it is well-known that Na^+ ions are extracted from the cathode bulk phase and interact with solvent molecules in the electrolyte to form solvated Na^+ ions. These solvated ions then migrate to the anode surface

under the influence of the electric field, where they detach from the solvent molecules, pass through the solid electrolyte interphase (SEI), and are subsequently intercalated into the anode, as seen in anodic intercalation reactions. The procedure encompasses the movement of Na^+ across the electrode bulk, the electrolyte, and the solid electrolyte interphase (SEI), in addition to the charge transfer interactions between Na^+ and electrons at the interface of the electrode and electrolyte [164]. With a current rate of 0.1 C, the initial specific discharge capacities of ClGO, SGO, and NGO are 389.7, 256.7, and 200 mAh g^{-1}, respectively.

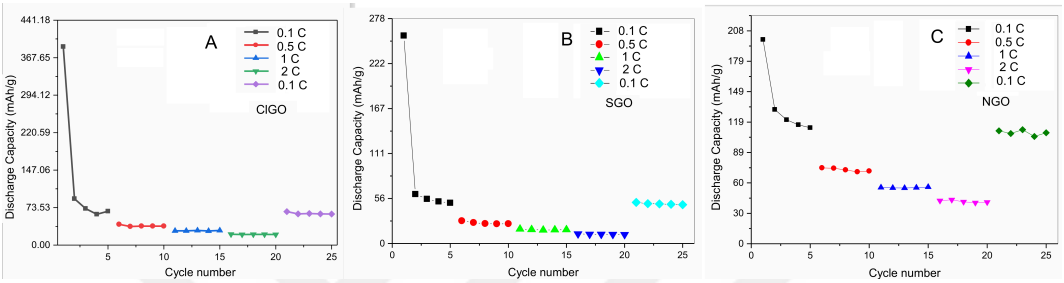


Figure 3.24 Single DGO Rate Performance Test: (A) ClGO, (B) SGO, and (C) NGO.

The capacity fading observed between the first and second cycle is primarily linked to the formation of the SEI layer. The SEI forms as a result of the reactions between the electrode material and the electrolyte, it can consume some of the sodium ions during its formation, leading to a loss in capacity during the initial cycles. Additionally, the small variations in capacity at the same current density during constant current cycling can be linked to an activation process. In our case, involves the interactions between sodium ions and dopant atoms present in DGO electrode. These interactions can influence the electrochemical performance of the anode, resulting in slight fluctuations in total capacity, particularly noticeable at lower current densities where ion transfer kinetics are more sensitive. Consequently, capacities measured at the same rate during different cycling sequences—such as constant current cycling tests and stepwise current cycling tests—may show slight variations due to the different level of activation that take place in each cycling process. This can result in slight differences in the effective capacity of the electrode material, ultimately impacting the overall performance of SIB.

3.3.3. Long cycling performance

Long-term cycling performance in Figure 3.25 was evaluated after activating the coin cell for one cycle at 0.1 C, followed by 100 cycles at 2 C to assess the effect of high-rate cycling on the coulombic efficiency. All DGO demonstrates minimal capacity degradation over the course of 100 cycles, maintaining both coulombic efficiency (CE) and capacity retention at over 99% at 2 C. This suggests that the DGO anodes exhibits excellent rate capabilities.

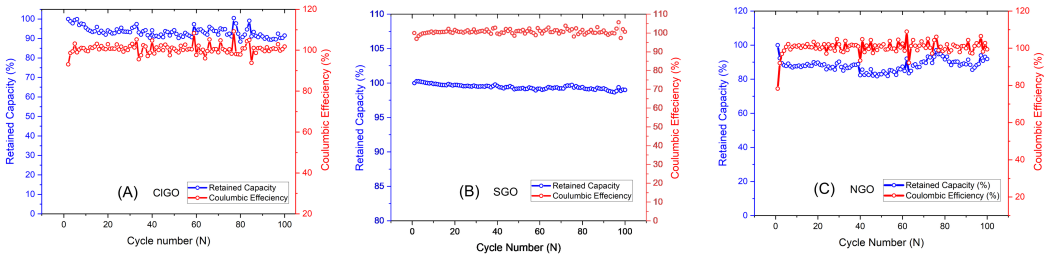


Figure 3.25 Capacity Retention vs. Coulombic Efficiency—Long-Term Cycling Performance (at 2C for 100 Cycles): (A) ClGO, (B) SGO, and (C) NGO.

3.3.4. EIS

EIS measurements were performed both before and after cycling to assess the electrochemical characteristics of the cell. As illustrated in Figure 3.26, the EIS spectra reveal a single semicircular feature in the high-frequency region, observed consistently both prior to and following the cycling process. This semicircle corresponds to the charge-transfer resistance at the electrode-electrolyte interface. Additionally, a sloping straight line is present in the low-frequency region, indicative of the diffusion-controlled process associated with sodium ion transport within the electrode material. These observations provide valuable insights into the cell's electrochemical behavior and the stability of its impedance characteristics during cycling.

Regarding ClGO, after cycling, the semicircle becomes smaller (Rct: 88.44 Ω compared to 677.2 Ω), as detailed in Table 3.3, indicating a reduction in charge transfer resistance (Rct). This decrease is likely due to the stabilization of the electrode and improved electrolyte infiltration [96]. Another factor contributing to the large irreversible capacity in the initial cycles may be the extensive trapping of Na^+ in the ClGO electrode, which, along with the presence of sodium, likely enhances the anode electronic conductivity [97], [98]. Moreover, the doped GO structure may experience further rearrangement or partial reduction after several

cycles, which enhances its conductivity and reduces the Rct [99]. In particular, the reduced R_{ct} value means better Na deposition kinetics [100].

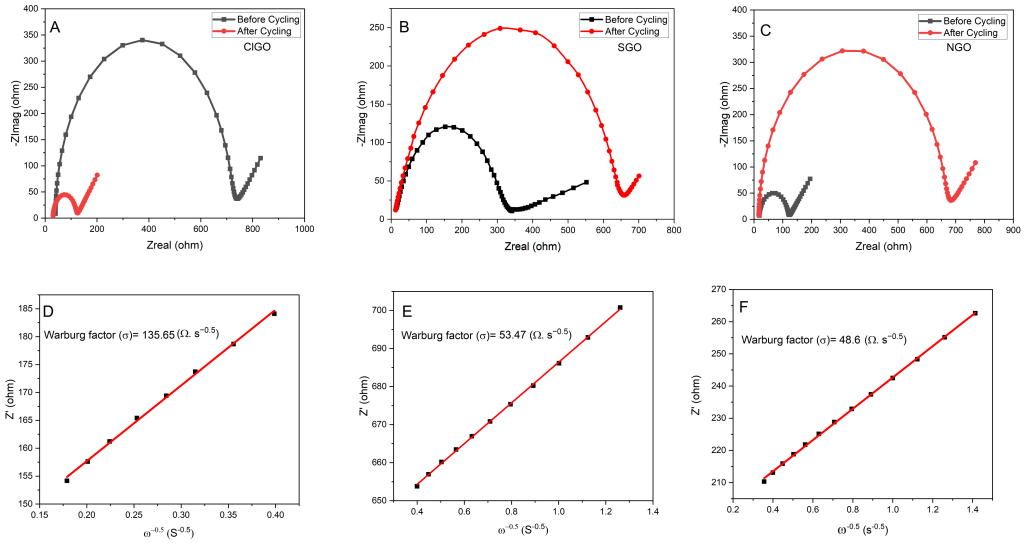


Figure 3.26 Nyquist Plots for: (A) ClGO, (B) SGO, and (C) NGO, Using $NaPF_6$ in EC:DMC With 10% FEC Electrolyte. (D-F) Represent The Corresponding Typical Plots for Z' vs. ($\omega^{-0.5}$) in The Low-Frequency Region.

Table 3.3 The Snigle DGO Using $NaPF_6$ in EC:DMC with 10% FEC Electrolyte Fitting Parameters For Electrochemical Impedance Spectroscopy (EIS) are as Follows: Rs is the Solution (Ohmic) Resistance, Rct is the Charge Transfer Resistance, CPE is the Constant Phase Element, And Zw is Warburg Impedance.

Sample	Zw / S*s^ (1/2) Before/after cycling	CPE/F Before/after cycling	Rs /Ω Before/after cycling	Rct/Ω Before/after cycling
ClGO	$7.8270e^{-3}$/$10.86e^{-3}$	$1.882e^{-6}$ / $3.886e^{-6}$	39.72 / 30.65	677.2 / 88.44
SGO	$6.7770e^{-3}$/ $7.01e^{-3}$	$1.5563e^{-6}$ / $2.453e^{-6}$	18.25 / 15.79	286.12/554.9
NGO	11.57 e^{-3} / 8.35 e^{-3}	$2.189e^{-6}$ / $2.168e^{-6}$	18.03 / 17.1	99.45 / 644.9

3.3.5. Calculation of Na^+ Diffusion Coefficients (D_{Na+})

To better perceive the electrochemical reaction kinetics of single DGO anodes. The EIS technique was employed to calculate the Na^+ diffusion coefficient (D_{EIS}). The calculation of the diffusion coefficient of Na^+ based on EIS results using the following equation:

$$\mathbf{D_{EIS}} = \left(\frac{\mathbf{R^2T^2}}{\mathbf{2\,A^2n^4F^4C^2\sigma^2}}\right) \qquad \textbf{Equ.3}$$

Here, R represents the universal gas constant (8.314 J mol^{-1} K^{-1}), T is the absolute temperature (298 K), (A) denotes the effective area of the electrode, (C) is the concentration of Na^+, (n) is the number of electrons involved, (F) is the Faraday constant (96485 C mol^{-1}), and (σ) is the Warburg coefficient. The Warburg coefficient represents the slope of the linear region at low frequencies in the plot of real resistance (Z') versus the inverse square root of angular frequency ($\omega^{-1/2}$) as depicted in (Figure 3.26.D-F). The Na^+ diffusion coefficient (D_{EIS}) of the ClGO, SGO, and NGO anodes were calculated to be about $6.8x10^{-13}$, $4.01x10^{-12}$, and $4.86x10^{-12}$ cm^2 s^{-1}, respectively.

3.4. Electrochemical Results of Single DGO Anodes Using $NaPF_6$ in Diglyme Electrolyte.

3.4.1. CV

The electrochemical performance of the single DGO anode was initially evaluated by cyclic voltammetry (CV), as shown in (Figure 3.27). The measurements were conducted using an electrolyte composed of $NaPF_6$ salt dissolved in 100% diglyme solvent. The half-cell was tested over a potential window of 0.02 to 3 V (vs. Na^+/Na) at various scan rates of 0.3, 0.5, 1, 3, 5, and 10 mV s^{-1}.

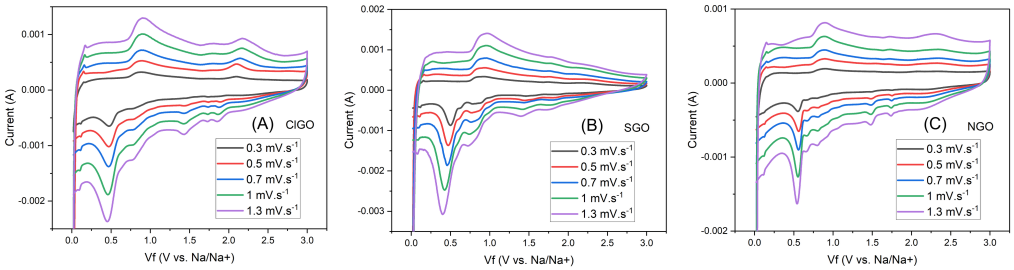


Figure 3.27 CV at Different Scan Rates (0.3-1.3 mV s^{-1}) for (A) ClGO, (B) SGO, and (C) NGO.

Each observed peak corresponds to the reversible extraction of Na^+ ions. Although the peaks maintain similar shapes, their intensities vary due to changes in the scan rate; specifically, peak currents increase with higher scan rates. The CV results demonstrate excellent electrochemical reversibility and stability, as evidenced by the substantial overlap of the curves across multiple cycles at different sweep rates [169]. A stable SEI layer may have developed, as evidenced by the coherence of all oxidation and reduction peaks, which demonstrate exceptional cyclability. The cause may be associated with the utilization of diglyme as an electrolyte solvent, which is thought to yield high reversibility connected to the formation of a stable SEI layer [68], [69]. The strong overlap of the curves demonstrates excellent reversibility, showing that the electrochemical processes are efficient and stable over multiple cycles. The presence of several oxidation and reduction peaks indicates a complex and sequential storage process. Additionally, no discer SIB peaks appear between 2.5 and 3 V, signifying the lack of any electrochemical response within this voltage interval. As a result, the cycling

performance and rate performance tests will be conducted in the 0.02–2.5 V potential range.

3.4.2. Rate performance results

The single DGO electrode exhibits an initial discharge capacity of approximately 415, 733, and 952 mAh g^{-1} at a rate of 0.1C for Cl, S, and NGO, respectively. The following cycle leads to a notable and largely irreversible decrease in capacity, reducing it to around 212, 392, and 442 mAh g^{-1}, as shown in (Figure 3.28.A-C). The formation of the solid electrolyte interphase (SEI) film accounts for the considerable capacity loss noted in the initial and following cycles [170]. Furthermore, initial parasitic reactions and irreversible phase transitions in the material lead to sodium depletion [30], [60], [162].

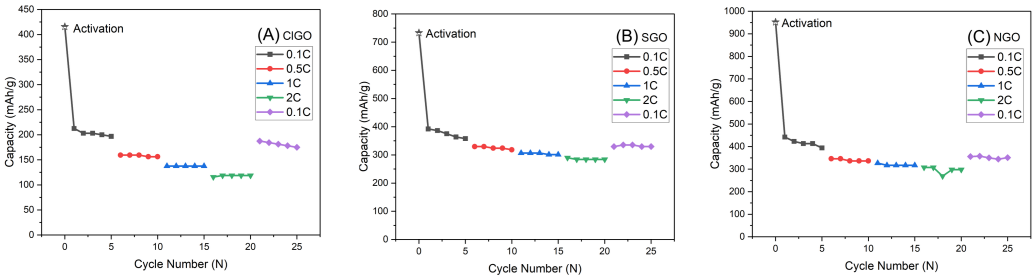


Figure 3.28 Rate Performance at Different Scan Rates, for (A) ClGO, (B) SGO, and (C) NGO.

The rate performance of the single DGO half-cell anode exhibits excellent cycling stability across current densities ranging from 0.1 C to 2 C. Notably, the anode demonstrates a strong ability to recover high discharge capacities when the current density returns to 0.1 C after cycling at 2 C, indicating effective structural stability. The capacity values at all tested rates remain close to their maximum, reflecting favorable kinetics and a mechanically stable electrode [171].

3.4.3. Long cycling performance

The long-term cycle stability of single DGO at a current density of 2C over 500 cycles is illustrated in (Figure 3.29), showing a discharge capacity at the end of the 500th cycle approximately 78, 199 and 240 mAh g^{-1} for Cl, S, and NGO, respectivlly. These results accompanied by a columbic efficiency of approximately 100% at the end of the 500th cycle.

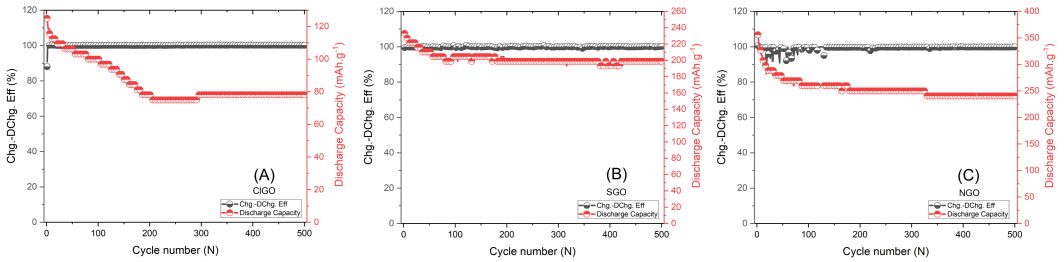


Figure 3.29 Long-Term Cycling Test at 2C for 500 Cycles: (A) ClGO, (B) SGO, and (C) NGO.

The long-term cycle stability of single DGO at a current density of 5C over 100 cycles is illustrated in (Figure 3.30), showing a discharge capacity at the end of the 100th cycle approximately 90, 97 and 86 mAh g^{-1} for Cl, S, and NGO, respectively. These results are also accompanied by a columbic efficiency of approximately 100% at the end of the 100th cycle.

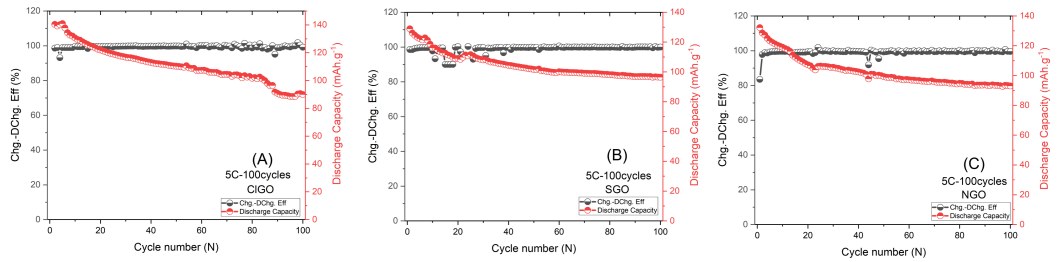


Figure 3.30 Long-term cycling test at high rate of 5C for 100 cycles for (A) ClGO, (B) SGO, and (C) NGO.

At a very high rate (10 C) (Figure 3.31.A), regarding the ClGO anode, the specific capacity decreased from an initial 141 mAh g^{-1} to 125 mAh g^{-1} after 50 cycles with a columbic efficiency of approximately 98.56%.

SGO anode (Figure 3.31.B), the specific capacity decreased from an initial 222 mAh g^{-1} to 210 mAh g^{-1} after 50 cycles with a columbic efficiency of approximately 99.89%.

Finally, for the NGO anode (Figure 3.31.C), the specific capacity decreased from an initial 326 mAh g^{-1} to 260 mAh g^{-1} after 50 cycles with a columbic efficiency of approximately 99.79%.

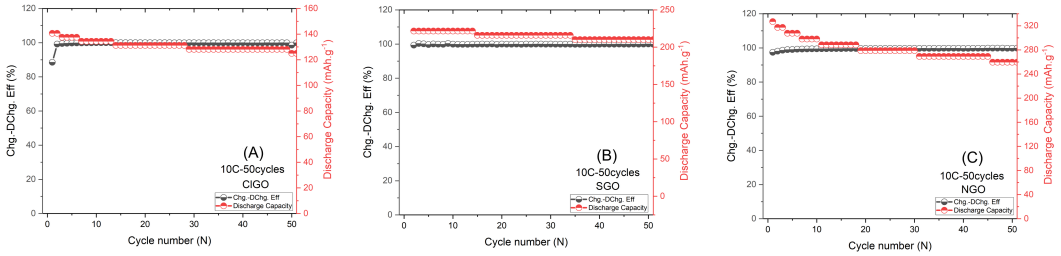


Figure 3.31 Long-Term Cycling Test at High Rate of 10 C for 50 Cycles: (A) ClGO, (B) SGO, and (C) NGO.

3.4.4. EIS

(Figure 3.32.A-C) presents the EIS test results for individual DGO anodes utilizing $NaPF_6$ in a 100% diglyme electrolyte. The results exhibit analogous behavior to that observed with $NaPF_6$ in EC: DMC with 10% FEC electrolyte. One semicircle in the high-frequency domain and a Warburg tail in the low-frequency domain.

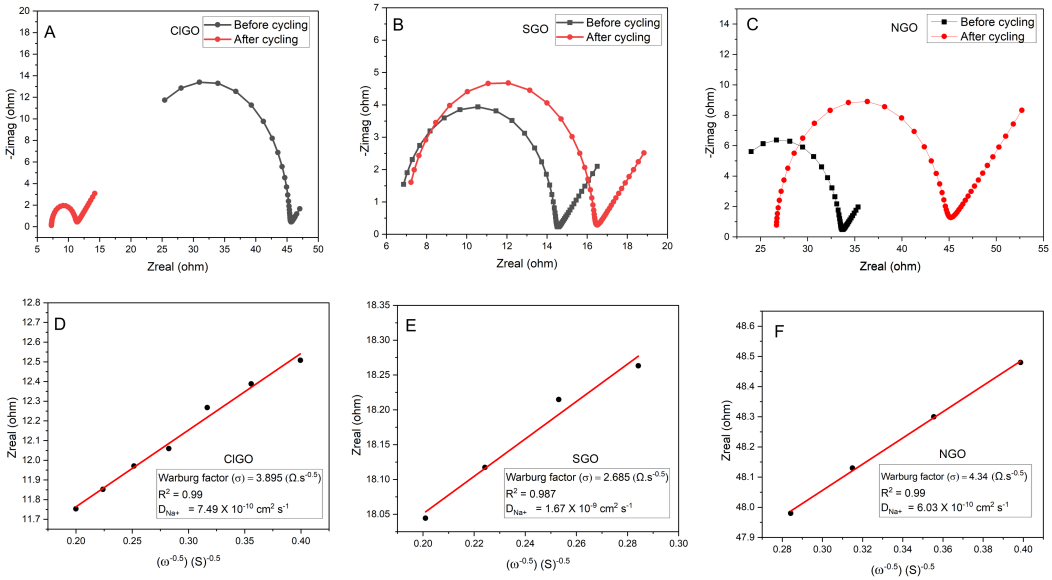


Figure 3.32 Nyquist Plots for (A) ClGO, (B) SGO, and (C) NGO, using $NaPF_6$ in Diglyme Electrolyte. (D-F) Represent the Corresponding Typical Plots for Zreal vs. ($\omega^{-0.5}$) in the Low-Frequency Region.

Similar behavior was observed for all single DGO anodes. In the ClGO anode, the R_{ct} decreased post-cycling. Whereas, for SGO and NGO anodes, Rct increased after cycling, as presented in Table 3.4.

Table 3.4 The Snigle DGO Using $NaPF_6$ in Diglyme Electrolyte Fitting Parameters for Electrochemical Impedance Spectroscopy (EIS) are as Follows: Rs is the Solution (Ohmic) Resistance, Rct is the Charge Transfer Resistance, CPE is the Constant Phase Element, and Zw is the Warburg Impedance.

Sample	Zw / S*s^ (1/2) Before/after cycling	CPE/F Before/after cycling	Rs/Ω Before/after cycling	Rct / Ω Before/after cycling
ClGO	0.1080 / 0.2887	$9.345e^{-7}/1325e^{-7}$	17.963 / 7.267	27.7851 / 3.8578
SGO	0.4243 / 0.355	$9.88e^{-6}$ / $9.65e^{-6}$	6.5384 / 6.942	7.8617 / 9.371
NGO	0.1017 / 0.1071	$2.08e^{-6}$/ $0.205e^{-6}$	20.64 / 26.66	12.73 / 17.73

3.4.5. Calculation of Na^+ Diffusion Coefficients (D_{Na+})

3.4.5.1. Diffusion calculations from EIS

To better perceive the electrochemical reaction kinetics, depending on EIS results, the Na^+ diffusion coefficient technique was calculated using (Equ. 3). As shown in (Figure 3.32.D-F), (D_{EIS}) of the ClGO, SGO, and NGO anodes were calculated to be about $7.49x10^{-10}$, $1.67x10^{-9}$, and $6.03x10^{-10}$ $cm^2\ s^{-1}$, respectively.

3.4.5.2. Diffusion calculations from CV Curves

(Figure 3.27) shows the typical CV curves of the single DGO anodes at a different scan rate between 0.3 and 1.3 mV s^{-1}. The diffusion coefficients were calculated based on the collective data of multiple CV scans at different scan rates. Using the Randles-Sevcik Equation [163]:

$$\mathbf{D_{cv}} = \left(\frac{\mathbf{Slope}}{\mathbf{2.69\times10^5\times n^{3/2}\times A\times C}}\right)^{\mathbf{2}} \qquad \textbf{Equ. 4}$$

The slope is defined as the peak current divided by the square root of the scan rate, as illustrated in (Figure 3.33). Here, n denotes the number of electrons transferred, A represents the valid area of the electrode (cm^2), and C indicates the concentration of Na^+ (mol cm^{-3}). The diffusion coefficient (D_{cv}) was determined to be 5.38×10^{-9}, 5.94×10^{-9}, and 2.57×10^{-9} $cm^2\ s^{-1}$ for Cl, S, and NGO, respectively.

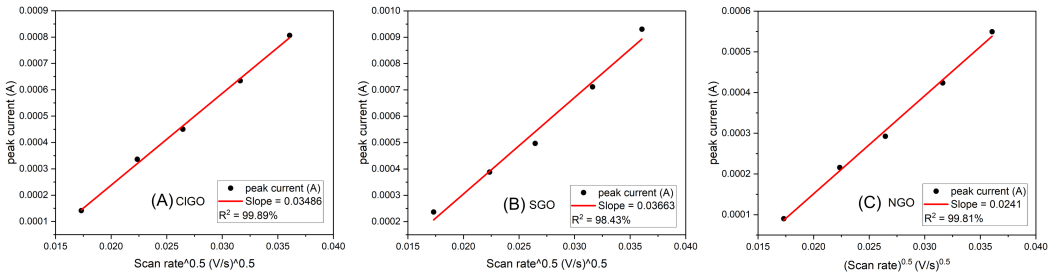


Figure 3.33 Linear Fitting Profile Between the Peak Current and Square Root of the Scan Rate (A) ClGO, (B) SGO, And (C) NGO.

The diffusion of Na^+ ions, determined through a CV-dependent technique, shows a higher D_{Na+} value in comparison to the diffusion calculated using EIS methods. This behavior is typical [169], as the diffusion calculated from CV scans accounts for contributions from surface processes, such as pseudocapacitance. In contrast, D_{EIS} yields a lower value because it reflects only bulk diffusion.

To distinguish the contributions of intercalation and capacitive processes to sodium storage, CV measurements were performed at scan rates ranging from 0.3 to 1.3 mV s^{-1}. The CV curves indicate that sodium storage in the single DGO anode is governed by a combination of capacitive and diffusion-controlled mechanisms. To further analyze the charge storage behavior, the power-law relationship was applied [172]:

$$\boldsymbol{log(i) = b.log(v) + log\ (a)} \qquad \textbf{Equ. 5}$$

Here, a represents the intercept associated with capacitance and diffusion processes, while b denotes the slope from the log(i) vs. log(v) plot, indicating the charge storage mechanism; specifically, (b) approaching 0.5 signifies diffusion control, whereas a (b) value approaching 1 indicates surface control. The slope (b) is derived from the log(i) against log(v) plot, as seen in (Figure 3.34.A-C). The slopes were determined to be approximately 0.92, 0.923, and 0.983, falling between 0.5 and 1, but very close to 1, which indicates a mixed charge storage mechanism.

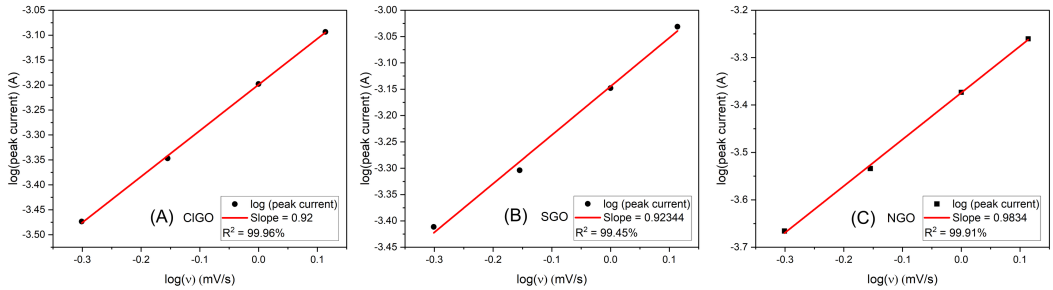


Figure 3.34 log (Peak Current) vs. log (ν, Scan Rate) for (A) ClGO, (B) SGO, and (C) NGO.

The current response at the corresponding potential V can be separated into diffusion-controlled processes ($k_2v^{0.5}$) and surface-controlled behavior (k_1v) [173].

$$\boldsymbol{i_p = K_1V + K_2V^{0.5}} \qquad \textbf{Equ. 6}$$

Rearrange to:

$$\boldsymbol{\frac{i}{v^{1/2}} = K_1V^{0.5} + K_2} \qquad \textbf{Equ. 7}$$

Where *i*, k_1v, $k_2v^{0.5}$, and ν represent the current at a fixed voltage, the surface- and diffusion-controlled currents, and the scan rate, respectively. Where K_1 represents the slope and K_2 represents the intercept of the slope between [(peak current / square root of scan rate) / square root of scan rate], as shown in (Figure 3.35. A-C).

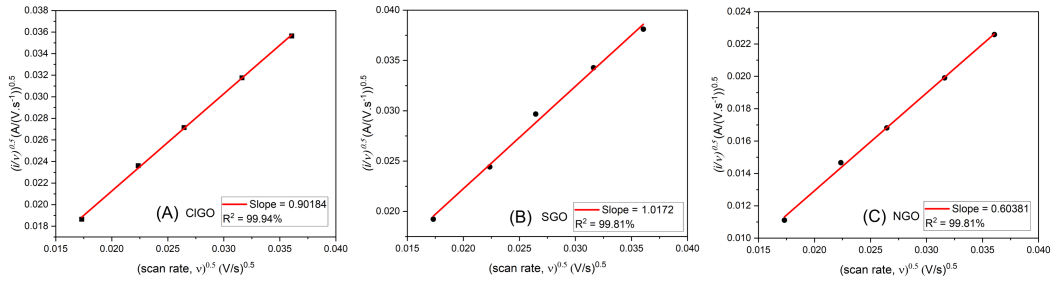


Figure 3.35 Relationship Between [(Peak Current / Square Root of Scan Rate) / Square Root of Scan Rate] for (A) ClGO, (B) SGO, and (C) NGO.

The capacitive (surface-controlled) and diffusive (intercalation-controlled) contributions at different scan rates show normal behavior of increasing the capacitive contributions with increasing the scan rate, with increasing capacitive contribution with increasing scan rate from 0.3 to 1.3 mV s^{-1} (Figure 3.36.A-C). That confirms that all DGO anodes show a pseudocapacitive behavior.

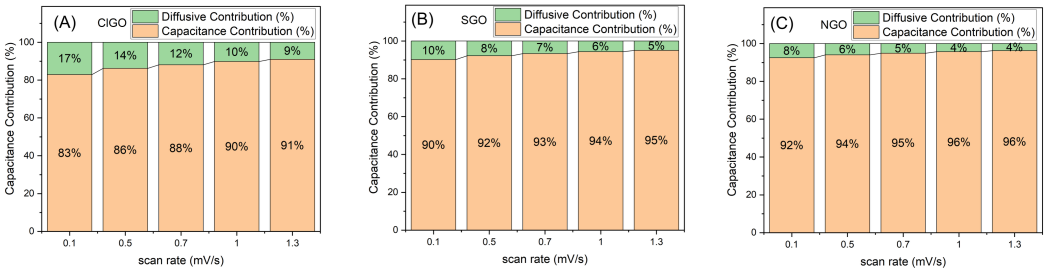


Figure 3.36 Total Na^+ Intercalation and Capacitive Contributions for (A) ClGO, (B) SGO, and (C) NGO.

Given that NGO displayed the highest capacity and SGO demonstrated exceptional cycling stability, we selected N-S-GO as the dual-doped GO to integrate these two desired properties.

3.5. Results of Dual DGO (N-S-GO) Anode Using $NaPF_6$ in Diglyme Electrolyte.

3.5.1. CV

The electrochemical performance of the N–S–GO anode was initially evaluated by cyclic voltammetry (CV), as shown in (Figure 3.37). The measurements were conducted using an electrolyte composed of $NaPF_6$ salt dissolved in 100% diglyme solvent. The half-cell was tested over a potential window of 0.02 to 3 V (vs. Na^+/Na) at various scan rates of 0.3, 0.5, 1, 3, 5, and 10 mV s^{-1}.

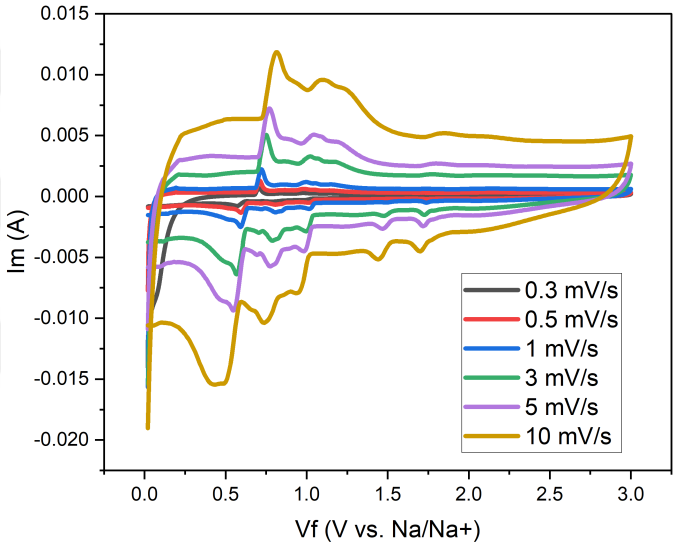


Figure 3.37 CV at Different Scan Rates (0.3-10 mV s^{-1}).

Each observed peak corresponds to the reversible extraction of Na^+ ions. Although the peaks maintain similar shapes, their intensities vary due to changes in the scan rate; specifically, peak currents increase with higher scan rates. The CV results demonstrate excellent electrochemical reversibility and stability, as evidenced by the substantial overlap of the curves across multiple cycles at different sweep rates [169]. A stable SEI layer may have developed, as evidenced by the coherence of all oxidation and reduction peaks, which demonstrate exceptional cyclability. The cause may be associated with the utilization of diglyme as an electrolyte solvent, which is thought to yield high reversibility connected to the formation of a stable SEI layer [68], [69]. The strong overlap of the curves demonstrates excellent reversibility, showing that the electrochemical processes are efficient and stable over multiple cycles. The presence of several oxidation and

reduction peaks indicates a complex and sequential storage process. Additionally, no discernible peaks appear between 2.5 and 3 V, signifying the lack of any electrochemical response within this voltage interval. As a result, the cycling performance and rate performance tests will be conducted in the 0.02–2.5 V potential range.

3.5.2. Rate performance results

The N-S-GO electrode exhibits an initial discharge capacity of approximately 457 mAh g^{-1} at a rate of 0.1C. The following cycle leads to a notable irreversible decrease in capacity, reducing it to around 195 mAh g^{-1}, as shown in (Figure 3.38). The formation of the solid electrolyte interphase (SEI) film accounts for the considerable capacity loss noted in the initial and following cycles [170]. Furthermore, initial parasitic reactions and irreversible phase transitions in the material lead to sodium depletion [30], [60], [162].

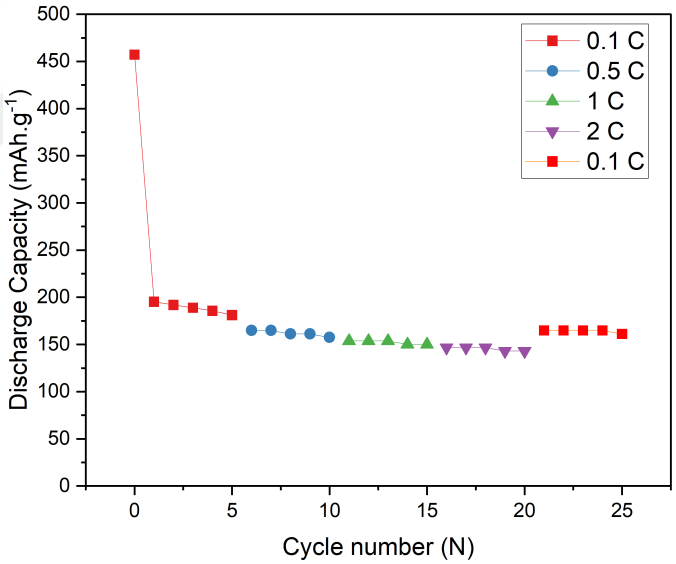


Figure 3.38 N-S-GO Rate Performance at Different Scan Rates.

The rate performance of the N–S–GO half-cell anode exhibits excellent cycling stability across current densities ranging from 0.1 C to 2 C. Notably, the anode demonstrates a strong ability to recover high discharge capacities when the current density returns to 0.1 C after cycling at 2 C, indicating effective structural stability. The capacity values at all tested rates remain close to their maximum, reflecting favorable kinetics and a mechanically stable electrode [171].

3.5.3. Long cycling performance

The long-term cycle stability of N-S-GO at a current density of 2C over 100 cycles is illustrated in (Figure 3.39), showing a discharge capacity of approximately 162 mAh g^{-1} maintained after 100 cycles, accompanied by a columbic efficiency of 99.99% at the 100th cycle.

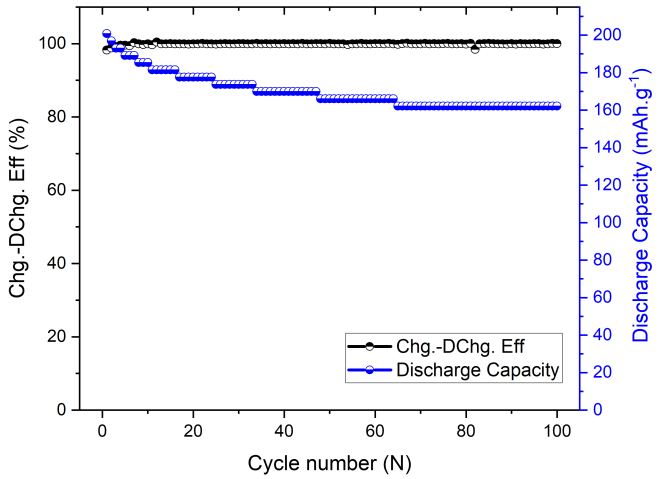


Figure 3.39 Long-Term Cycling Test at 2 C for 100 Cycles.

At 5C (Figure 3.40), the specific capacity fell from 209.82 mAh g^{-1} to 156.25 mAh g^{-1} after 50 cycles, yielding in a columbic efficiency of about 85%.

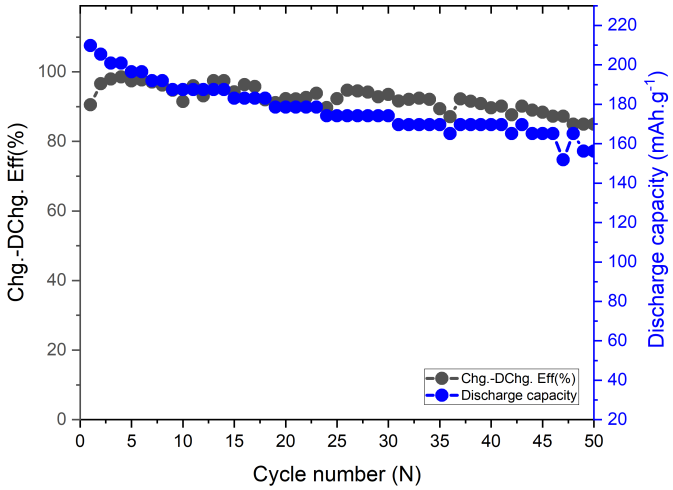


Figure 3.40 Long-Term Cycling Test at 5C for 50 Cycles.

3.5.4. EIS

EIS was performed before and after 100 cycles at 2 C (Figure 3.41) to investigate the electrode kinetics, with the fitting results summarized in Table 3.5.

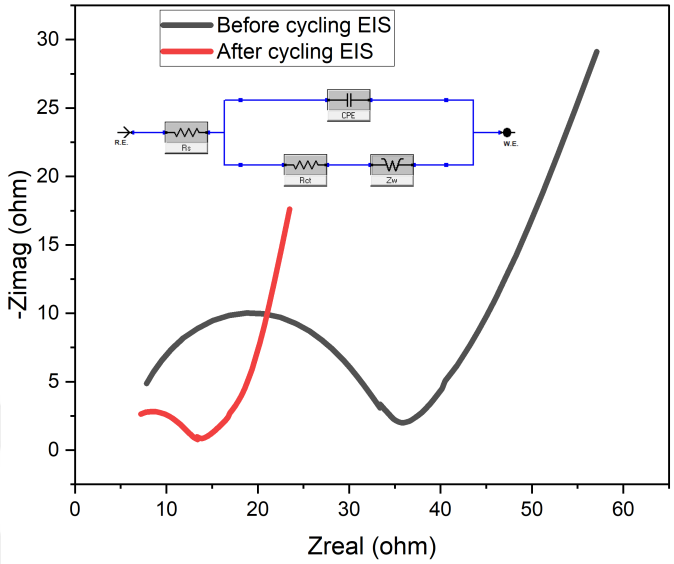


Figure 3.41 Nyquist Plots and the Inset Shows the Equivalent Circuit.

Table 3.5 The N-S-GO Using $NaPF_6$ In EC:DMC with 10% FEC Electrolyte Fitting Parameters for Electrochemical Impedance Spectroscopy (EIS) are as Follows: Rs is the Solution (Ohmic) Resistance, Rct is the Charge Transfer Resistance, CPE is the Constant Phase Element, And Zw is The Warburg Impedance.

Parameter/unit	Before cycling	After cycling
Zw/S*s^ (1/2)	$3.2523e^{-2}$	$6.34\ e^{-2}$
CPE/F	$4.4730e^{-7}$	$8.38\ e^{-7}$
Rs/Ω	8.1139	6.8561
Rct/Ω	25.05	6.36

Although R_{ct} was anticipated to rise with cycling, resulting in significantly higher charge transfer resistance [68]. Our findings indicate a reduction in charge transfer resistance (R_{ct}) post-cycling. This may arise from multiple factors. Initially, cycling can lead to the formation of a more stable and consistent SEI layer, enhancing the wettability of the electrode–electrolyte interface [174]. Secondly, the doped GO structure may experience further rearrangement or partial reduction after several cycles, which enhances its conductivity and reduces the R_{ct} [30].

3.5.5. Calculation of Na^+ Diffusion Coefficients (D_{Na+})

3.5.5.1. Diffusion calculations from EIS

To better understand the electrochemical reaction kinetics underlying the Na^+ storage mechanism in the N–S–GO anode, an analysis of EIS and CV responses was conducted. Determining the diffusion coefficient (D) is crucial for evaluating the dynamics and efficiency of sodium-ion transport within the battery system. As illustrated in (Figure 3.42.A), (D_{Na+}) was determined using (EIS) results prior to and following cycling. The calculation of the diffusion coefficient of Na^+ derived from EIS results ($D_{EIS,\ Na+}$) was conducted using (Equ. 3).

The diffusion coefficient of Na^+ (D_{EIS}) for the N-S-GO anode was calculated to be approximately 4.478 x 10^{-11} cm^2 s^{-1} before cycling and 3.239 x 10^{-10} cm^2 s^{-1} after cycling. The enhancement of the Na^+ diffusion coefficient by one order of magnitude after cycling indicates that the N-S-GO anode improves its electrochemical efficiency as time progresses. This demonstrates both structural integrity and enhanced kinetics during operation.

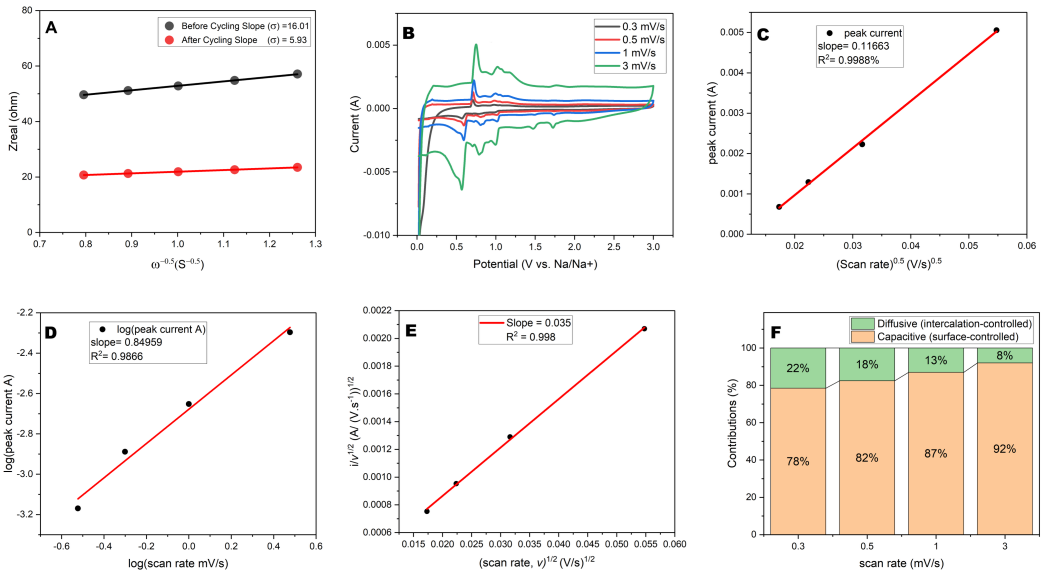


Figure 3.42 (A) The Typical Plots Between Z' vs. ($\omega^{-0.5}$) in the Low Frequency Regain, (B) CV at Scan Rates (0.3-1.3 mv s^{-1}), (C) Linear Fitting Profile Between the Peak Current and Square Root of the Scan Rate , (D) log(i) Vs. log(*v*), (E) Relation Between [(Peak Current / Square Root of Scan Rate)/Square Root of Scan Rate], (F) Total Na^+ Intercalation and Capacitive Contributions.

3.5.5.2. Diffusion calculations from CV

(Figure 3.42.B) shows the typical CV curves of N-S-GO at a different scan rate between 0.3 and 1.3 mV s^{-1}. The diffusion coefficients were calculated based on the collective data of multiple CV scans at different scan rates. Using the Randles-Sevcik Equation (Equ. 4). The slope is defined as the peak current divided by the square root of the scan rate, as illustrated in (Figure 3.42.C). The diffusion coefficient (D_{cv}) was determined to be 8.68×10^{-12} cm^2 s^{-1}. The diffusion of Na^+ ions, determined through a CV-dependent technique, shows a higher D_{Na+} value in comparison to the diffusion calculated using EIS methods. This behavior is typical [169], as the diffusion calculated from CV scans accounts for contributions from surface processes, such as pseudocapacitance. In contrast, D_{EIS} yields a lower value because it reflects only bulk diffusion.

To distinguish the contributions of intercalation and capacitive processes to sodium storage, CV measurements were performed at scan rates ranging from 0.3 to 1.3 mV s^{-1}. The CV curves indicate that sodium storage in the N–S–GO anode is governed by a combination of capacitive and diffusion-controlled mechanisms. To further analyze the charge storage behavior, the power-law relationship was applied (Equ. 5). The slope (b) is derived from the log(*i*) against log(*v*) plot, as seen in (Figure 3.42.D). The slope was determined to be approximately 0.893, falling between 0.5 and 1.0, which indicates a mixed charge storage mechanism. This result supports the conclusion that the chronoamperometric synthesis of N–S–GO powder as an anode material for SIBs enhances ion diffusion properties. This observation aligns with previously reported findings in the literature [175].

The current response at the corresponding potential V can be separated into diffusion-controlled processes ($k_2v^{0.5}$) and surface-controlled behavior (k_1v) using (Equ. 6 and Equ. 7) [173]. As shown in (Figure 3.42.E) the capacitive (surface-controlled) and diffusive (intercalation-controlled) contributions at different scan rates show normal behavior of increasing the capacitive contributions with increasing the scan rate, with increasing capacitive contribution from 70% to 83% with increasing scan rate from 0.3 to 1.3 mV s^{-1} (Figure 3.42.F). That confirms that the N-S-GO anode shows a pseudocapacitive behavior.

4

CONCLUSION

In presented work, single doped graphene oxide and dual doped graphene oxide including chlorine, sulfur, nitrogen doped graphene oxide along with nitrogen-sulfur dual doped graphene oxide were synthesized and used as anode materials of sodium ion batteries.

Two types of electrolytes were used (Carbonate-based electrolyte consist of 1.0 M $NaPF_6$ dissolved in a 1:1 (v/v) mixture of ethylene carbonate (EC) and dimethyl carbonate (DMC) with 10 vol.% fluoroethylene carbonates (FEC) as an additive, and (ii) Ether-based electrolyte consist of 1.0 M $NaPF_6$ in 100% diglyme).

During the initial stage of the research, the synthesized powders were structural examined using XPS, FT-IR, Raman, XRD, BET surface area assessments, and property analysis through SEM-EDS and TEM techniques.

The second stage began with employing the synthesized powders as standalone active anode materials, without the addition of other active components, and were analyzed electrochemically through cyclic voltammetry (CV), electrochemical impedance spectroscopy (EIS), and galvanostatic charge-discharge tests.

The electrochemical results showed when ether-based electrolyte compared to carbonate base the initial discharge capacity increased significantly, even after the capacity droped after SEI formation as shown in Figure 4.1. The results originate from various storage mechanisms when utilizing different electrolytes.

The interpretation of the storage mechanism, derived from the gathered electrochemical and spectroscopy analyses, indicates that the utilization of diglyme solvent as an electrolyte will result in the co-intercalation of solvent molecules alongside Na^+ ions, thereby forming (t-GICs) as Na^+ $(diglyme)_2$ complexes [70],

[171], [176]. The utilization of 1M $NaPF_6$ in diglyme electrolyte yielded significant reversibility, a phenomenon attributed to the formation of a stable solid-electrolyte interphase (SEI).

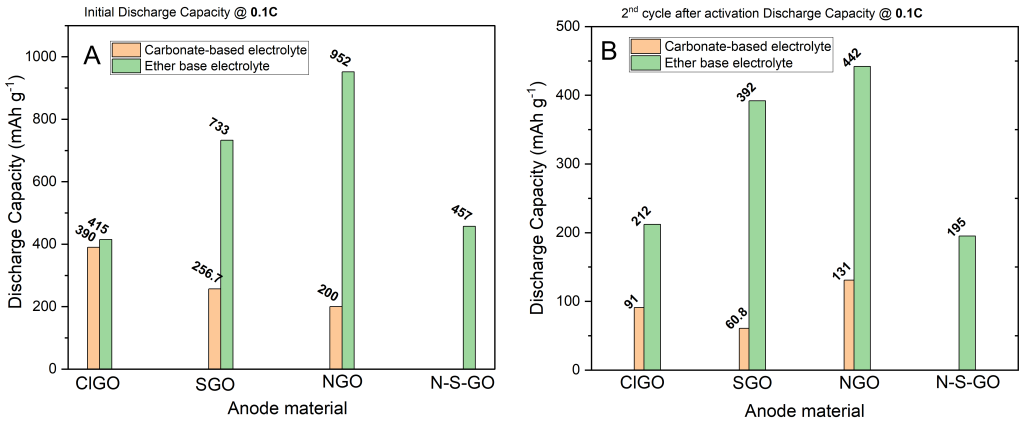


Figure 4.1 (A) Initial Discharge Capacity (B) 2nd Discharge Capacity, at 0.1C Rate.

Figure 4.2.A demonstrates that ClGO, SGO, and NGO exhibit capacity retention rates of 62.5%, 85.4%, and 64.1%, respectively, after 500 cycles at 2C. The capacity retention of N-S-GO after 100 cycles was 77.8%.

Figure 4.2.B shows ClGO, SGO, and NGO after 100 cycles at 5C (1000 mA g^{-1}), retaining 64%, 74.8%, and 71.4% of their initial values, respectively. N-S-GO after 50 cycles retains 74.5% of its initial values.

Figure 4.2.C presents the performance of ClGO, SGO, and NGO at a maximum rate of 10C (2000 mA g^{-1}), with retention rates of 88.9%, 94.9%, and 79.4% after 50 cycles.

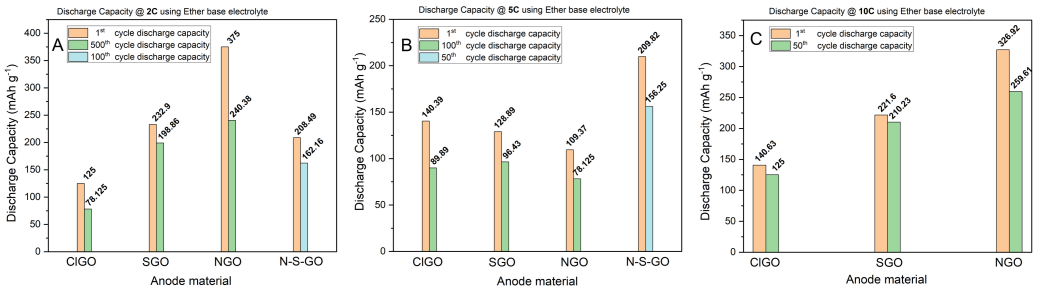


Figure 4.2 Long Cycle Performance (A) 2C, (B) 5C, and (C) 10C, Utilizing Ether-Based Electrolytes.

The electrochemical performance can be summarized as follows.

- The ether-based electrolyte demonstrated superior electrochemical performance in comparison to the carbonate-based electrolyte.
- SGO demonstrated moderate capabilities while exhibiting exceptional cycling stability, particularly at elevated rates.
- CIGO demonstrated the least capacities, despite possessing excellent long-term stability.
- The NGO demonstrated the most impressive overall performance, providing the highest discharge capacities along with superior tolerance to elevated C-rates. In both carbonate and ether-based electrolytes.
- All single DGO demonstrated an exceptionally high retention rate at 10C (2A g^{-1}).
- N-S-GO demonstrates a greater diffusive contribution compared to the individual DGO.

The results showed a viable pathway for synthesizing doped GO anode materials via chronoamperometry and enhancing their electrochemical performance using glyme-based electrolytes, thereby advancing their potential for practical application in large-scale SIBs.

REFERENCES

[1] "World Oil Statistics - Worldometer." Accessed: Dec. 08, 2023. [Online]. Available: https://www.worldometers.info/oil/#

[2] G. L. Soloveichik, "Flow Batteries: Current Status and Trends," Oct. 28, 2015, American Chemical Society. doi: 10.1021/cr500720t.

[3] C. Vaalma, D. Buchholz, M. Weil, and S. Passerini, "A cost and resource analysis of sodium-ion batteries," Nat Rev Mater, vol. 3, p. 18013, 2018.

[4] I. Energy Agency, "Global Energy and Climate Model Documentation 2023," 2023. [Online]. Available: www.iea.org

[5] I. Energy Agency, "Net Zero by 2050 - A Roadmap for the Global Energy Sector," 2050. [Online]. Available: www.iea.org/t&c/

[6] D. Larcher and J. M. Tarascon, "Towards greener and more sustainable batteries for electrical energy storage," Nat Chem, vol. 7, no. 1, pp. 19–29, 2015, doi: 10.1038/nchem.2085.

[7] X. Xu et al., "Nitrogen and Sulfur Co-Doped Graphene Nanosheets to Improve Anode Materials for Sodium-Ion Batteries," ACS Appl Mater Interfaces, vol. 10, no. 43, pp. 37172–37180, 2018, doi: 10.1021/acsami.8b15940.

[8] H. Zhang, I. Hasa, and S. Passerini, "Beyond Insertion for Na-Ion Batteries: Nanostructured Alloying and Conversion Anode Materials," Jun. 15, 2018, Wiley-VCH Verlag. doi: 10.1002/aenm.201702582.

[9] H. Zhang, I. Hasa, and S. Passerini, "Beyond Insertion for Na-Ion Batteries: Nanostructured Alloying and Conversion Anode Materials," Jun. 15, 2018, Wiley-VCH Verlag. doi: 10.1002/aenm.201702582.

[10] "Lithium-ion batteries - statistics & facts | Statista." Accessed: Dec. 12, 2023. [Online]. Available: https://www.statista.com/topics/2049/lithium-ion-battery-industry/#topicOverview

[11] M. D. Slater, D. Kim, E. Lee, and C. S. Johnson, "Sodium-ion batteries," Adv Funct Mater, vol. 23, no. 8, pp. 947–958, Feb. 2013, doi: 10.1002/adfm.201200691.

[12] G. Schafer, "Storage and/or transportation case," Aug. 14, 1990, Google Patents. Accessed: Jun. 30, 2024. [Online]. Available: https://patents.google.com/patent/US4947992A/en

[13] D. Saurel, B. Orayech, B. Xiao, D. Carriazo, X. Li, and T. Rojo, “From charge storage mechanism to performance: a roadmap toward high specific energy sodium-ion batteries through carbon anode optimization,” Adv Energy Mater, vol. 8, no. 17, p. 1703268, 2018.

[14] A. K. Thakur et al., “Advancement in graphene-based nanocomposites as high capacity anode materials for sodium-ion batteries,” J Mater Chem A Mater, vol. 9, no. 5, pp. 2628–2661, 2021, doi: 10.1039/D0TA10227J.

[15] P. Desai, J. Huang, D. Foix, J.-M. Tarascon, and S. Mariyappan, “Zero volt storage of Na-ion batteries: Performance dependence on cell chemistry!,” J Power Sources, vol. 551, p. 232177, 2022, doi: https://doi.org/10.1016/j.jpowsour.2022.232177.

[16] J.-Y. Hwang, S.-T. Myung, and Y.-K. Sun, “Sodium-ion batteries: present and future,” Chem Soc Rev, vol. 46, no. 12, pp. 3529–3614, 2017, doi: 10.1039/C6CS00776G.

[17] S. Rana, R. Kumar, and R. S. Bharj, “Current trends, challenges, and prospects in material advances for improving the overall safety of lithium-ion battery pack,” Chemical Engineering Journal, vol. 463, p. 142336, May 2023, doi: 10.1016/j.cej.2023.142336.

[18] K. M. Thushara et al., “Interlayer, gallery-engineered graphene oxide using selective protection of mono-Boc-ethylenediamine as anode for sodium ion batteries,” J Energy Storage, vol. 73, p. 109237, Dec. 2023, doi: 10.1016/J.EST.2023.109237.

[19] L. Li, C. Wang, C. Zhang, X. Cao, J. Bai, and R. Li, “Yolk-shell V2O3/nitrogen-doped carbon spheres as an ultra-long life anode for half/full sodium-ion batteries,” J Energy Storage, vol. 66, p. 107504, Aug. 2023, doi: 10.1016/J.EST.2023.107504.

[20] V. Nguyen, Y. Liu, Y. Li, S. A. Hakim, X. Yang, and W. Chen, “Synthesis and Electrochemical Performance of $Fe_2(MoO_4)_3$ /Carbon Nanotubes Nanocomposite Cathode Material for Sodium-Ion Battery,” ECS Journal of Solid State Science and Technology, vol. 4, no. 5, pp. M25–M29, Feb. 2015, doi: 10.1149/2.0011505jss.

[21] C. Li et al., “Electrospinning Engineering Enables High-Performance Sodium-Ion Batteries,” Advanced Fiber Materials, vol. 4, no. 1, pp. 43–65, 2022, doi: 10.1007/s42765-021-00088-6.

[22] I. K. Ilic, K. Schutjajew, W. Zhang, and M. Oschatz, “Changes of porosity of hard carbons during mechanical treatment and the relevance for sodium-ion anodes,” Carbon N Y, vol. 186, pp. 55–63, Jan. 2022, doi: 10.1016/j.carbon.2021.09.063.

[23] R. Wang, S. Zhang, S. Peng, Y. Tong, and X. Hu, “Research progress of electrolyte additives for subzero-temperature aqueous sodium-ion batteries,” Dec. 01, 2024, Springer. doi: 10.1007/s43979-024-00081-z.

[24] K. Kubota, N. Yabuuchi, H. Yoshida, M. Dahbi, and S. Komaba, “Layered oxides as positive electrode materials for Na-ion batteries,” MRS Bull, vol. 39, no. 5, pp. 416–422, May 2014, doi: 10.1557/mrs.2014.85.

[25] H. Xiang, Y. Wang, K. Li, X. Zhang, and Z. Chen, “A comprehensive study on state-of-charge and state-of-health estimation of sodium-ion batteries,” J Energy Storage, vol. 72, p. 108314, Nov. 2023, doi: 10.1016/j.est.2023.108314.

[26] “Federal Aviation Administration.” Accessed: Dec. 08, 2023. [Online]. Available: https://www.faa.gov/

[27] Y. Sun et al., “Comparison of reduction products from graphite oxide and graphene oxide for anode applications in lithium-ion batteries and sodium-ion batteries,” Nanoscale, vol. 9, no. 7, pp. 2585–2595, Feb. 2017, doi: 10.1039/c6nr07650e.

[28] J. Wan et al., “In situ transmission electron microscopy observation of sodiation-desodiation in a long cycle, high-capacity reduced graphene oxide sodium-ion battery anode,” Chemistry of Materials, vol. 28, no. 18, pp. 6528–6535, 2016, doi: 10.1021/acs.chemmater.6b01959.

[29] Y.-X. Wang, S.-L. Chou, H.-K. Liu, and S.-X. Dou, “Reduced graphene oxide with superior cycling stability and rate capability for sodium storage,” Carbon N Y, vol. 57, pp. 202–208, 2013, doi: https://doi.org/10.1016/j.carbon.2013.01.064.

[30] J. Li et al., “Novel iodine-doped reduced graphene oxide anode for sodium ion batteries,” RSC Adv, vol. 7, no. 87, pp. 55060–55066, 2017, doi: 10.1039/C7RA09349G.

[31] A. P. Vijaya Kumar Saroja, M. S. Garapati, R. ShyiamalaDevi, M. Kamaraj, and S. Ramaprabhu, “Facile synthesis of heteroatom doped and undoped graphene quantum dots as active materials for reversible lithium and sodium ions storage,” Appl Surf Sci, vol. 504, Feb. 2020, doi: 10.1016/j.apsusc.2019.144430.

[32] J. Li et al., “A confined ‘microreactor’ synthesis strategy to three dimensional nitrogen-doped graphene for high-performance sodium ion battery anodes,” J Power Sources, vol. 378, pp. 105–111, Feb. 2018, doi: 10.1016/j.jpowsour.2017.12.028.

[33] J. Zhao et al., “Partially Reduced Holey Graphene Oxide as High Performance Anode for Sodium-Ion Batteries,” Adv Energy Mater, vol. 9, no. 7, p. 1803215, Feb. 2019, doi: 10.1002/aenm.201803215.

[34] M. M. Doeff, Y. Ma, S. J. Visco, and L. C. De Jonghe, “Electrochemical Insertion of Sodium into Carbon,” J Electrochem Soc, vol. 140, no. 12, pp. L169–L170, Dec. 1993, doi: 10.1149/1.2221153.

[35] K.-H. Nam, K. Hwa Chae, J.-H. Choi, K.-J. Jeon, and C.-M. Park, “Superior carbon black: High-performance anode and conducting additive for rechargeable Li- and Na-ion batteries,” Chemical Engineering Journal, vol. 417, p. 129242, Aug. 2021, doi: 10.1016/j.cej.2021.129242.

[36] R. Alc antara, J. M. Jim enez-Mateos, P. Lavela, and J. L. Tirado, “Carbon black: a promising electrode material for sodium-ion batteries.” [Online]. Available: www.elsevier.com/locate/elecom

[37] C. Zhang, Q. Wang, Y. Song, G. Wang, and H. Wang, “3D ordered hierarchically porous carbon derived from colloidal crystal templates towards alkali metal-ion batteries,” Carbon N Y, vol. 201, pp. 76–99, Jan. 2023, doi: 10.1016/j.carbon.2022.08.087.

[38] M. Kigozi et al., “Electrochemical exfoliation and deposition of sodium-graphene oxide composite for high specific capacity cathode/anode for dual-carbon sodium ion battery application,” Chem Phys Lett, vol. 822, Jul. 2023, doi: 10.1016/j.cplett.2023.140499.

[39] T. Chen, L. Pan, T. Lu, C. Fu, D. H. C. Chua, and Z. Sun, “Fast synthesis of carbon microspheres via a microwave-assisted reaction for sodium ion batteries,” J. Mater. Chem. A, vol. 2, no. 5, pp. 1263–1267, 2014, doi: 10.1039/C3TA14037G.

[40] T. Chen et al., “Electrospun carbon nanofibers as anode materials for sodium ion batteries with excellent cycle performance,” J Mater Chem A Mater, vol. 2, no. 12, p. 4117, 2014, doi: 10.1039/c3ta14806h.

[41] M. Dahbi et al., “Synthesis of hard carbon from argan shells for Na-ion batteries,” J Mater Chem A Mater, vol. 5, no. 20, pp. 9917–9928, 2017, doi: 10.1039/c7ta01394a.

[42] X. Dou et al., “Hard carbons for sodium-ion batteries: Structure, analysis, sustainability, and electrochemistry,” Mar. 01, 2019, Elsevier B.V. doi: 10.1016/j.mattod.2018.12.040.

[43] E. Gibertini et al., “Algae-derived hard carbon anodes for Na-ion batteries,” J Appl Electrochem, vol. 51, no. 12, pp. 1665–1673, Dec. 2021, doi: 10.1007/s10800-021-01609-2.

[44] X. Fan, X. Kong, P. Zhang, and J. Wang, “Research progress on hard carbon materials in advanced sodium-ion batteries,” Energy Storage Mater, vol. 69, p. 103386, May 2024, doi: 10.1016/J.ENSM.2024.103386.

[45] H. Kim, H. Yang, J. Kang, and N. Takeuchi, “Multifunctional Disordered Sulfur-Doped Carbon for Efficient Sodium-Ion-Exchange and 2-Electron-Transfer-Dominant Oxygen Reduction Reaction,” Carbon N Y, vol. 182, pp. 242–253, Sep. 2021, doi: 10.1016/J.CARBON.2021.05.063.

[46] D.-Y. Kim, O. L. Li, and J. Kang, “Novel synthesis of highly phosphorus-doped carbon as an ultrahigh-rate anode for sodium ion batteries,” Carbon N Y, vol. 168, pp. 448–457, 2020, doi: https://doi.org/10.1016/j.carbon.2020.07.021.

[47] P. Wang, H. Wang, C. Liang, and K. Yu, “Two-dimensional porous flake biomass carbon with large layer spacing as an anode material for sodium ion batteries,” Diam Relat Mater, vol. 131, p. 109601, 2023, doi: https://doi.org/10.1016/j.diamond.2022.109601.

[48] Y. Cao et al., “Sodium ion insertion in hollow carbon nanowires for battery applications,” 2012. doi: 10.1021/nl3016957.

[49] N. M. S. Hidayah et al., “Comparison on graphite, graphene oxide and reduced graphene oxide: Synthesis and characterization,” AIP Conf Proc, vol. 1892, 2017, doi: 10.1063/1.5005764.

[50] H. Xu, H. Chen, and C. Gao, “Advanced Graphene Materials for Sodium/Potassium/Aluminum-Ion Batteries,” ACS Mater Lett, vol. 3, no. 8, pp. 1221–1237, Aug. 2021, doi: 10.1021/acsmaterialslett.1c00280.

[51] Y. Li, M. Chen, B. Liu, Y. Zhang, X. Liang, and X. Xia, “Heteroatom Doping: An Effective Way to Boost Sodium Ion Storage,” Jul. 01, 2020, Wiley-VCH Verlag. doi: 10.1002/aenm.202000927.

[52] J. Haruyama, T. Ikeshoji, and M. Otani, “Analysis of lithium insertion/desorption reaction at interfaces between graphite electrodes and electrolyte solution using density functional+ implicit solvation theory,” The Journal of Physical Chemistry C, vol. 122, no. 18, pp. 9804–9810, 2018, doi: 10.1021/acs.jpcc.8b01979.

[53] H. Liu et al., “Creative utilization of natural nanocomposites: nitrogen-rich mesoporous carbon for a high-performance sodium ion battery,” J Mater Chem A Mater, vol. 5, no. 20, pp. 9572–9579, 2017, doi: 10.1039/C7TA01891F.

[54] S. Li, J. Qiu, C. Lai, M. Ling, H. Zhao, and S. Zhang, “Surface capacitive contributions: Towards high rate anode materials for sodium ion batteries,” Nano Energy, vol. 12, pp. 224–230, 2015, doi: 10.1016/j.nanoen.2014.12.032.

[55] Ranjusha Ra, Advanced Materials for Sodium Ion Storage - 1st Edition - Ranjusha Ra. 2020.

[56] Q. Li et al., “Boosting sodium storage performance of biomass-derived porous carbon anodes by surface functionalized strategy,” Diam Relat Mater, vol. 147, p. 111341, 2024, doi: https://doi.org/10.1016/j.diamond.2024.111341.

[57] C. Yang et al., “Regulating solid electrolyte interphase film on fluorine-doped hard carbon anode for sodium-ion battery,” Carbon Energy, vol. 6, no. 6, Jun. 2024, doi: 10.1002/cey2.503.

[58] S. Xin, Y. X. Yin, Y. G. Guo, and L. J. Wan, “A high-energy room-temperature sodium-sulfur battery,” Advanced Materials, vol. 26, no. 8, pp. 1261–1265, Feb. 2014, doi: 10.1002/adma.201304126.

[59] M. Almarzoge, M. Gencten, and G. Ozsin, “Production of Sulphur-Doped Graphene Oxide as an Anode Material for Na-Ion Batteries,” ECS Journal of Solid State Science and Technology, vol. 13, no. 7, p. 071001, Jul. 2024, doi: 10.1149/2162-8777/ad5b87.

[60] M. Almarzoge, M. Gencten, and G. Ozsin, “One-Step Chronoamperometric Synthesized Nitrogen-Doped Graphene Oxide as a Novel Anode for Sodium-Ion Battery with an Enhanced Electrochemical Performance,” ChemElectroChem, vol. 12, no. 4, Feb. 2025, doi: 10.1002/celc.202400564.

[61] G. Ma, Z. Xiang, K. Huang, Z. Ju, Q. Zhuang, and Y. Cui, “Graphene-Based Phosphorus-Doped Carbon as Anode Material for High-Performance Sodium-Ion Batteries,” Particle and Particle Systems Characterization, vol. 34, no. 5, pp. 1–7, 2017, doi: 10.1002/ppsc.201600315.

[62] B. Rosenberg, Advanced Materials for Sodium Ion Storage, vol. 25, no. 8. 2005.

[63] H. Kim, J. Hong, Y. U. Park, J. Kim, I. Hwang, and K. Kang, “Sodium storage behavior in natural graphite using ether-based electrolyte systems,” Adv Funct Mater, vol. 25, no. 4, pp. 534–541, Jan. 2015, doi: 10.1002/adfm.201402984.

[64] K. Li et al., “Evolution of the electrochemical interface in sodium ion batteries with ether electrolytes,” Nat Commun, vol. 10, no. 1, p. 725, Feb. 2019, doi: 10.1038/s41467-019-08506-5.

[65] C. Hakim et al., “P-doped hard carbon as anode material for sodium-ion batteries,” in 2019 7th International Renewable and Sustainable Energy Conference (IRSEC), IEEE, 2019, pp. 1–3.

[66] A. P. Cohn, K. Share, R. Carter, L. Oakes, and C. L. Pint, “Ultrafast Solvent-Assisted Sodium Ion Intercalation into Highly Crystalline Few-Layered Graphene,” Nano Lett, vol. 16, no. 1, pp. 543–548, Jan. 2016, doi: 10.1021/acs.nanolett.5b04187.

[67] I. Hasa et al., “A sodium-ion battery exploiting layered oxide cathode, graphite anode and glyme-based electrolyte,” J Power Sources, vol. 310, pp. 26–31, Apr. 2016, doi: 10.1016/j.jpowsour.2016.01.082.

[68] Z. W. Seh, J. Sun, Y. Sun, and Y. Cui, “A highly reversible room-temperature sodium metal anode,” ACS Cent Sci, vol. 1, no. 8, pp. 449–455, Nov. 2015, doi: 10.1021/acscentsci.5b00328.

[69] M. Goktas et al., “Graphite as Cointercalation Electrode for Sodium-Ion Batteries: Electrode Dynamics and the Missing Solid Electrolyte Interphase (SEI),” Adv Energy Mater, vol. 8, no. 16, Jun. 2018, doi: 10.1002/aenm.201702724.

[70] A. C. S. Jensen, H. Au, S. Gärtner, M. Titirici, and A. J. Drew, “Solvation of $NaPF_6$ in Diglyme Solution for Battery Electrolytes,” Batter Supercaps, vol. 3, no. 12, pp. 1306–1310, Dec. 2020, doi: 10.1002/batt.202000144.

[71] M. Goktas, B. Akduman, P. Huang, A. Balducci, and P. Adelhelm, “Temperature-Induced Activation of Graphite Co-intercalation Reactions for Glymes and Crown Ethers in Sodium-Ion Batteries,” Journal of Physical Chemistry C, vol. 122, no. 47, pp. 26816–26824, Nov. 2018, doi: 10.1021/acs.jpcc.8b07915.

[72] X. Dong et al., “MoS2/N-doped graphene aerogles composite anode for high performance sodium/potassium ion batteries,” Electrochim Acta, vol. 339, p. 135932, 2020, doi: 10.1016/j.electacta.2020.135932.

[73] X. Ma and D. Gao, “High Capacitive Storage Performance of Sulfur and Nitrogen Codoped Mesoporous Graphene,” ChemSusChem, vol. 11, no. 6, pp. 1048–1055, 2018, doi: 10.1002/cssc.201702457.

[74] J. Cai et al., “Nitrogen-doped graphene-wrapped Cu2S as a superior anode in sodium-ion batteries,” Carbon N Y, vol. 170, pp. 430–438, 2020, doi: 10.1016/j.carbon.2020.08.031.

[75] M. S. Islam et al., “N-doped reduced graphene oxide (rGO) wrapped carbon microfibers as binder-free electrodes for flexible fibre supercapacitors and sodium-ion batteries,” J Energy Storage, vol. 37, no. March, p. 102453, 2021, doi: 10.1016/j.est.2021.102453.

[76] D. Wang et al., “In situ double-template fabrication of boron-doped 3D hierarchical porous carbon network as anode materials for Li- and Na-ion batteries,” Appl Surf Sci, vol. 464, no. July 2018, pp. 422–428, 2019, doi: 10.1016/j.apsusc.2018.09.035.

[77] W. Zhang et al., “Hierarchical porous N-doped functionalized reduced graphene oxide by 2-aminoanthraquinone for aqueous zinc-ion hybrid capacitors with high energy density and ultralong-life,” J Energy Storage, vol. 61, p. 106715, 2023, doi: https://doi.org/10.1016/j.est.2023.106715.

[78] N. M. Latiff, C. C. Mayorga-Martinez, L. Wang, Z. Sofer, A. C. Fisher, and M. Pumera, “Microwave irradiated N- and B,Cl-doped graphene: Oxidation method has strong influence on capacitive behavior,” Appl Mater Today, vol. 9, pp. 204–211, 2017, doi: https://doi.org/10.1016/j.apmt.2017.07.006.

[79] W. K. Maboya, N. J. Coville, and S. D. Mhlanga, “Fabrication of chlorine nitrogen co-doped carbon nanomaterials by an injection catalytic vapor deposition method,” Mater Res Express, vol. 8, no. 1, p. 015007, 2021.

[80] H. Gursu, M. Gencten, and Y. Sahin, “Preparation of sulphur-doped graphene-based electrodes by cyclic voltammetry: A potential application for vanadium redox flow battery,” Int J Electrochem Sci, vol. 13, no. 1, pp. 875–885, Jan. 2018, doi: 10.20964/2018.01.71.

[81] H. Gürsu et al., “A novel green and one-step electrochemical method for production of sulfur-doped graphene powders and their performance as an anode in Li-ion battery,” Ionics (Kiel), vol. 26, no. 10, pp. 4909–4919, Oct. 2020, doi: 10.1007/s11581-020-03671-w.

[82] M. B. Arvas, N. Karatepe, M. Gencten, and Y. Sahin, “Fabrication of high-performance symmetrical coin cell supercapacitors by using one step and green synthesis sulfur doped graphene powders,” New Journal of Chemistry, vol. 45, no. 15, pp. 6928–6939, 2021, doi: 10.1039/D0NJ06061E.

[83] A. Mansuroglu, M. Gencten, M. B. Arvas, M. Sahin, A. E. Bozdoğan, and Y. Sahin, “A novel electrolyte additive for gel type valve regulated lead acid batteries: Sulfur doped graphene oxide,” Int J Energy Res, vol. 45, no. 15, pp. 21390–21402, Dec. 2021, doi: 10.1002/er.7189.

[84] M. Besir Arvas, M. Gencten, and Y. Sahin, “Investigation of supercapacitor properties of chlorine-containing functional groups doped graphene

electrodes," Journal of Electroanalytical Chemistry, vol. 918, p. 116438, Aug. 2022, doi: 10.1016/j.jelechem.2022.116438.

[85] H. Gursu et al., "Production of chlorine-containing functional group doped graphene powders using Yucel's method as anode materials for Li-ion batteries," RSC Adv, vol. 11, no. 63, pp. 40059–40071, Dec. 2021, doi: 10.1039/D1RA07653A.

[86] X. Wang, G. Sun, P. Routh, D. H. Kim, W. Huang, and P. Chen, "Heteroatom-doped graphene materials: Syntheses, properties and applications," Chem Soc Rev, vol. 43, no. 20, pp. 7067–7098, 2014, doi: 10.1039/c4cs00141a.

[87] H. Gursu et al., "Production of chlorine-containing functional group doped graphene powders using Yucel's method as anode materials for Li-ion batteries," RSC Adv, vol. 11, no. 63, pp. 40059–40071, 2021, doi: 10.1039/d1ra07653a.

[88] X. Zhang et al., "Impact of chlorine functionalization on high-mobility chemical vapor deposition grown graphene," 2013. doi: 10.1021/nn4026756.

[89] X. Wang et al., "Sulfur covalently bonded graphene with large capacity and high rate for high-performance sodium-ion batteries anodes," Nano Energy, vol. 15, pp. 746–754, Jul. 2015, doi: 10.1016/j.nanoen.2015.05.038.

[90] G. Vignesh, P. Devendran, N. Nallamuthu, S. Sudhahar, P. S. Kumar, and M. K. Kumar, "Effects of nitrogen, sulphur, and temperature treatments on the spectral, structural, and electrochemical characteristics of graphene oxide for energy storage applications," Carbon Trends, vol. 11, p. 100262, Jun. 2023, doi: 10.1016/j.cartre.2023.100262.

[91] Z. Wang et al., "Pure thiophene–sulfur doped reduced graphene oxide: synthesis, structure, and electrical properties," Nanoscale, vol. 6, no. 13, p. 7281, 2014, doi: 10.1039/c3nr05061k.

[92] X. Wang et al., "Sulfur covalently bonded graphene with large capacity and high rate for high-performance sodium-ion batteries anodes," Nano Energy, vol. 15, pp. 746–754, 2015, doi: 10.1016/j.nanoen.2015.05.038.

[93] S. Xin, Y. X. Yin, Y. G. Guo, and L. J. Wan, "A high-energy room-temperature sodium-sulfur battery," Advanced Materials, vol. 26, no. 8, pp. 1261–1265, 2014, doi: 10.1002/adma.201304126.

[94] W. Chen, M. Wan, Q. Liu, X. Xiong, F. Yu, and Y. Huang, "Heteroatom-Doped Carbon Materials: Synthesis, Mechanism, and Application for Sodium-Ion Batteries," Small Methods, vol. 3, no. 4, pp. 1–18, 2019, doi: 10.1002/smtd.201800323.

[95] F. Yang et al., "Dopamine derived nitrogen-doped carbon sheets as anode materials for high-performance sodium ion batteries," Carbon N Y, vol. 91, no. 932, pp. 88–95, 2015, doi: 10.1016/j.carbon.2015.04.049.

[96] Y. Liu et al., "In situ transmission electron microscopy study of electrochemical sodiation and potassiation of carbon nanofibers," 2014. doi: 10.1021/nl500970a.

[97] J. Li et al., “A confined ‘microreactor’ synthesis strategy to three dimensional nitrogen-doped graphene for high-performance sodium ion battery anodes,” J Power Sources, vol. 378, no. September 2017, pp. 105–111, 2018, doi: 10.1016/j.jpowsour.2017.12.028.

[98] S. McArdle et al., “Defective Carbon for Next-Generation Stationary Energy Storage Systems: Sodium-Ion and Vanadium Flow Batteries,” ChemElectroChem, vol. 11, no. 4, p. e202300512, Feb. 2024, doi: https://doi.org/10.1002/celc.202300512.

[99] N. Ahmad et al., “Boron and phosphorous co-doped porous carbon as high-performance anode for sodium-ion battery,” Solid State Ion, vol. 356, no. June, 2020, doi: 10.1016/j.ssi.2020.115455.

[100] T. Zhang, T. Zhang, F. Wang, and F. Ran, “Pretreatment Process Before Heat Pyrolysis of Plant-based Precursors Paving Way for Fabricating High-Performance Hard Carbon for Sodium-Ion Batteries,” ChemElectroChem, vol. 10, no. 24, p. e202300442, Dec. 2023, doi: https://doi.org/10.1002/celc.202300442.

[101] L. Stobinski et al., “Graphene oxide and reduced graphene oxide studied by the XRD, TEM and electron spectroscopy methods,” J Electron Spectros Relat Phenomena, vol. 195, pp. 145–154, 2014, doi: 10.1016/j.elspec.2014.07.003.

[102] X. Jiao, Y. Qiu, L. Zhang, and X. Zhang, “Comparison of the characteristic properties of reduced graphene oxides synthesized from natural graphites with different graphitization degrees,” RSC Adv, vol. 7, no. 82, pp. 52337–52344, Nov. 2017, doi: 10.1039/C7RA10809E.

[103] K. Krishnamoorthy, M. Veerapandian, K. Yun, and S.-J. Kim, “The chemical and structural analysis of graphene oxide with different degrees of oxidation,” Carbon N Y, vol. 53, pp. 38–49, 2013.

[104] X. Wang, G. Li, M. H. Seo, F. M. Hassan, M. A. Hoque, and Z. Chen, “Sulfur Atoms Bridging Few-Layered MoS2 with S-Doped Graphene Enable Highly Robust Anode for Lithium-Ion Batteries,” Adv Energy Mater, vol. 5, no. 23, p. 1501106, 2015.

[105] B. Sungur, E. Bayram, and A. İ. Kömür, “Enhanced Performance for Li & Na Ion Battery Anodes by Charge Modulation of Interface Through SiC4 and SiN1C3 Active Centers on Silicon Nitrogen Co-Doped Graphene,” ChemElectroChem, vol. n/a, no. n/a, p. e202400401, Sep. 2024, doi: https://doi.org/10.1002/celc.202400401.

[106] Y. Wang, C. Wang, Y. Wang, H. Liu, and Z. Huang, “Boric Acid Assisted Reduction of Graphene Oxide: A Promising Material for Sodium-Ion Batteries,” ACS Appl Mater Interfaces, vol. 8, no. 29, pp. 18860–18866, 2016, doi: 10.1021/acsami.6b04774.

[107] H. Piao et al., “Multistep Reaction Processes in Epoxide Formation from 1-Chloro-2-methyl-2-propanol on Ag(110) Revealed by TPXPS and TPD Experiments,” Journal of Physical Chemistry B, vol. 107, no. 50, pp. 13976–13985, Dec. 2003, doi: 10.1021/jp035892e.

[108] R. Krumpolec et al., “Structural and optical properties of luminescent copper(I) chloride thin films deposited by sequentially pulsed chemical vapour deposition,” Coatings, vol. 8, no. 10, 2018, doi: 10.3390/COATINGS8100369.

[109] D. Martin-Vosshage and B. V. R. Chowdari, “XPS studies on (PEO) n LiClO4 and (PEO) n Cu (ClO4) 2 polymer electrolytes,” J Electrochem Soc, vol. 142, no. 5, p. 1442, 1995.

[110] Y. Bai et al., “Hard Carbon Originated from Polyvinyl Chloride Nanofibers As High-Performance Anode Material for Na-Ion Battery,” ACS Applied Materials & Interfaces, vol. 7, no. 9, pp. 5598–5604, Mar. 2015, doi: 10.1021/acsami.5b00861.

[111] X. Xu et al., “Nitrogen and Sulfur Co-Doped Graphene Nanosheets to Improve Anode Materials for Sodium-Ion Batteries,” ACS Appl Mater Interfaces, vol. 10, no. 43, pp. 37172–37180, 2018, doi: 10.1021/acsami.8b15940.

[112] B. Quan et al., “Solvothermal-Derived S-Doped Graphene as an Anode Material for Sodium-Ion Batteries,” Advanced Science, vol. 5, no. 5, pp. 1–7, 2018, doi: 10.1002/advs.201700880.

[113] K. M. Thushara et al., “Interlayer, gallery-engineered graphene oxide using selective protection of mono-Boc-ethylenediamine as anode for sodium ion batteries,” J Energy Storage, vol. 73, Dec. 2023, doi: 10.1016/j.est.2023.109237.

[114] Q. Xu et al., “Preparation of highly photoluminescent sulfur-doped carbon dots for Fe(<scp>iii</scp>) detection,” J Mater Chem A Mater, vol. 3, no. 2, pp. 542–546, 2015, doi: 10.1039/C4TA05483K.

[115] J. Xu, M. Wang, N. P. Wickramaratne, M. Jaroniec, S. Dou, and L. Dai, “High-performance sodium ion batteries based on a 3D anode from nitrogen-doped graphene foams,” Advanced Materials, vol. 27, no. 12, pp. 2042–2048, Mar. 2015, doi: 10.1002/adma.201405370.

[116] Y. Jiang et al., “A novel interlayer-expanded tin disulfide/reduced graphene oxide nanocomposite as anode material for high-performance sodium-ion batteries,” J Colloid Interface Sci, vol. 611, pp. 215–223, 2022, doi: 10.1016/j.jcis.2021.12.017.

[117] H. Gao et al., “Synthesis of S-doped graphene by liquid precursor,” Nanotechnology, vol. 23, no. 27, p. 275605, Jul. 2012, doi: 10.1088/0957-4484/23/27/275605.

[118] S. Li et al., “Sulfur-/Nitrogen-Rich Albumen Derived ‘Self-Doping’ Graphene for Sodium-Ion Storage,” Chemistry - A European Journal, vol. 25, no. 63, pp. 14358–14363, 2019, doi: 10.1002/chem.201902575.

[119] G. Ma, K. Huang, Q. Zhuang, and Z. Ju, “Superior cycle stability of nitrogen-doped graphene nanosheets for Na-ion batteries,” Mater Lett, vol. 174, pp. 221–225, 2016, doi: 10.1016/j.matlet.2016.03.111.

[120] M. B. Arvas, M. Gencten, and Y. Sahin, “One-step synthesized N-doped graphene-based electrode materials for supercapacitor applications,” pp. 2241–2256, 2021.

[121] V. Etacheri, R. R. Maça, V. S. Avvaru, C. N. Hong, A. Alazemi, and V. G. Pol, “Ultrathin (15 nm) Carbon Sheets with Surface Oxygen Functionalization for Efficient Pseudocapacitive Na-ion Storage,” ChemElectroChem, vol. 11, no. 17, p. e202400255, Sep. 2024, doi: https://doi.org/10.1002/celc.202400255.

[122] H. Liu et al., “Nitrogen-doped carbon/graphene hybrid anode material for sodium-ion batteries with excellent rate capability,” J Power Sources, vol. 319, pp. 195–201, 2016, doi: 10.1016/j.jpowsour.2016.04.040.

[123] L. Wang et al., “Chlorine-Doped Graphene Quantum Dots with Enhanced Anti- and Pro-Oxidant Properties,” ACS Appl Mater Interfaces, vol. 11, no. 24, pp. 21822–21829, 2019, doi: 10.1021/acsami.9b03194.

[124] Alyaa. K. Mageed, Dayang Radiah.A.B.,A.Salmiaton,Shamsul Izhar, “Preparation and Characterization of Nitrogen Doped Reduced Graphene Oxide Sheet,” International Journal of Applied Chemistry, vol. 12, no. 1, pp. 104–108, 2016.

[125] X. Xu et al., “Facile synthesis of boron and nitrogen-doped graphene as efficient electrocatalyst for the oxygen reduction reaction in alkaline media,” Int J Hydrogen Energy, vol. 39, no. 28, pp. 16043–16052, 2014, doi: 10.1016/j.ijhydene.2013.12.079.

[126] E. Jayabal, A. Natarajan, and V. Rengarajan, “One-pot hydrothermal synthesis of nitrogen-doped reduced graphene oxide for the highly sensitive and simultaneous determination of dihydroxy benzene isomers,” J Appl Electrochem, vol. 51, no. 8, pp. 1189–1205, 2021, doi: 10.1007/s10800-021-01563-z.

[127] M. G. Ersozoglu, H. Gursu, M. Gencten, A. S. Sarac, and Y. Sahin, “A green approach to fabricate binder-free S-doped graphene oxide electrodes for vanadium redox battery,” Int J Energy Res, vol. 45, no. 2, pp. 2126–2137, 2021, doi: 10.1002/er.5906.

[128] R. Kumar et al., “Bulk synthesis of highly conducting graphene oxide with long range ordering,” RSC Adv, vol. 5, no. 45, pp. 35893–35898, 2015, doi: 10.1039/c5ra01943e.

[129] Lling-Lling Tan, Wee-Jun Ong, Siang-Piao Chai, and Abdul Rahman Moha, “Reduced graphene oxide-TiO 2 nanocomposite as a promising visible-light-active photocatalyst for the conversion of carbon dioxide,” Nanoscale Res Lett, vol. 8, no. 465, pp. 1–9, 2013.

[130] K. Kakaei, M. Hamidi, and S. Husseindoost, “Chlorine-doped reduced graphene oxide nanosheets as an efficient and stable electrode for supercapacitor in acidic medium,” J Colloid Interface Sci, vol. 479, pp. 121–126, 2016, doi: 10.1016/j.jcis.2016.06.058.

[131] L. L. Tan, W. J. Ong, S. P. Chai, and A. R. Mohamed, “Reduced graphene oxide-TiO2 nanocomposite as a promising visible-light-active photocatalyst

for the conversion of carbon dioxide," Nanoscale Res Lett, vol. 8, no. 1, pp. 1–9, 2013, doi: 10.1186/1556-276X-8-465.

[132] L. Chen et al., "One-step synthesis of sulfur doped graphene foam for oxygen reduction reactions," Dalton Transactions, vol. 43, no. 9, pp. 3420–3423, 2014, doi: 10.1039/c3dt52253a.

[133] Y. Wang et al., "Sulfur-Doped Reduced Graphene Oxide for Enhanced Sodium Ion Pseudocapacitance," Nanomaterials, vol. 9, no. 5, p. 752, May 2019, doi: 10.3390/nano9050752.

[134] M. P. Kumar et al., "Nitrogen Doped Graphene as Metal Free Electrocatalyst for Efficient Oxygen Reduction Reaction in Alkaline Media and Its Application in Anion Exchange Membrane Fuel Cells," J Electrochem Soc, vol. 163, no. 8, pp. F848–F855, 2016, doi: 10.1149/2.0541608jes.

[135] M. Mowry, D. Palaniuk, C. C. Luhrs, and S. Osswald, "Insitu Raman spectroscopy and thermal analysis of the formation of nitrogen-doped graphene from urea and graphite oxide," RSC Adv, vol. 3, no. 44, pp. 21763–21775, 2013, doi: 10.1039/c3ra42725k.

[136] L. G. Cançado et al., "Quantifying defects in graphene via Raman spectroscopy at different excitation energies," Nano Lett, vol. 11, no. 8, pp. 3190–3196, 2011, doi: 10.1021/nl201432g.

[137] G. Surekha, K. V. Krishnaiah, N. Ravi, and R. Padma Suvarna, "FTIR, Raman and XRD analysis of graphene oxide films prepared by modified Hummers method," J Phys Conf Ser, vol. 1495, no. 1, pp. 1–6, 2020, doi: 10.1088/1742-6596/1495/1/012012.

[138] F. T. Johra, J. W. Lee, and W. G. Jung, "Facile and safe graphene preparation on solution based platform," Journal of Industrial and Engineering Chemistry, vol. 20, no. 5, pp. 2883–2887, 2014, doi: 10.1016/j.jiec.2013.11.022.

[139] F. Shahzad et al., "Sulfur-doped graphene laminates for EMI shielding applications," J Mater Chem C Mater, vol. 3, no. 38, pp. 9802–9810, 2015, doi: 10.1039/c5tc02166a.

[140] X. Ma, C. Ji, Y. Liu, X. Yu, and X. Xiong, "Oxygen-rich graphene vertically grown on 3D N-Doped carbon foam for high-performance sodium ion batteries," J Power Sources, vol. 530, no. December 2021, p. 231292, 2022, doi: 10.1016/j.jpowsour.2022.231292.

[141] M. B. Arvas, H. Gürsu, M. Gencten, and Y. Sahin, "Supercapacitor applications of novel phosphorus doped graphene-based electrodes," J Energy Storage, vol. 55, no. October, 2022, doi: 10.1016/j.est.2022.105766.

[142] M. B. Arvas, H. Gürsu, M. Gencten, and Y. Sahin, "New Approach Synthesis of S, N Co-Doped Graphenes for High-Performance Supercapacitors," ChemistrySelect, vol. 7, no. 21, 2022, doi: 10.1002/slct.202200360.

[143] Y. Sun et al., "Comparison of reduction products from graphite oxide and graphene oxide for anode applications in lithium-ion batteries and sodium-

ion batteries," Nanoscale, vol. 9, no. 7, pp. 2585–2595, 2017, doi: 10.1039/c6nr07650e.

[144] A. Das, B. Chakraborty, and A. K. Sood, "Raman spectroscopy of graphene on different substrates and influence of defects," Bulletin of Materials Science, vol. 31, no. 3, pp. 579–584, 2008, doi: 10.1007/s12034-008-0090-5.

[145] C. Backes et al., "Spectroscopic metrics allow in situ measurement of mean size and thickness of liquid-exfoliated few-layer graphene nanosheets," Nanoscale, vol. 8, no. 7, pp. 4311–4323, 2016, doi: 10.1039/c5nr08047a.

[146] W. Pei, Y. Wang, Y. Liu, L. Zhou, J. Lei, and J. Zhang, "Activation of peroxymonosulfate by LaCO3OH coupled with N, S co-doped graphene for levofloxacin degradation," Sep Purif Technol, vol. 344, no. March, p. 127157, Sep. 2024, doi: 10.1016/j.seppur.2024.127157.

[147] C. Liu, X. Liu, J. Tan, Q. Wang, H. Wen, and C. Zhang, "Nitrogen-doped graphene by all-solid-state ball-milling graphite with urea as a high-power lithium ion battery anode," J Power Sources, vol. 342, pp. 157–164, Feb. 2017, doi: 10.1016/J.JPOWSOUR.2016.11.110.

[148] L. Qie et al., "Sulfur-Doped Carbon with Enlarged Interlayer Distance as a High-Performance Anode Material for Sodium-Ion Batteries," Dec. 01, 2015, John Wiley and Sons Inc. doi: 10.1002/ADVS.201500195.

[149] Y. Zhang, J. Zhao, H. Sun, Z. Zhu, J. Zhang, and Q. Liu, "B, N, S, Cl doped graphene quantum dots and their effects on gas-sensing properties of Ag-LaFeO3," Sens Actuators B Chem, vol. 266, pp. 364–374, Aug. 2018, doi: 10.1016/j.snb.2018.03.109.

[150] S. D. Bergin et al., "Towards Solutions of Single-Walled Carbon Nanotubes in Common Solvents," Advanced Materials, vol. 20, no. 10, pp. 1876–1881, May 2008, doi: https://doi.org/10.1002/adma.200702451.

[151] A. Langrock, Y. Xu, Y. Liu, S. Ehrman, A. Manivannan, and C. Wang, "Carbon coated hollow Na 2FePO 4F spheres for Na-ion battery cathodes," J Power Sources, vol. 223, pp. 62–67, Feb. 2013, doi: 10.1016/j.jpowsour.2012.09.059.

[152] L. Tang, R. Ji, X. Li, K. S. Teng, and S. P. Lau, "Energy-level structure of nitrogen-doped graphene quantum dots," J Mater Chem C Mater, vol. 1, no. 32, pp. 4908–4915, 2013, doi: 10.1039/C3TC30877D.

[153] T. Lin et al., "Nitrogen-doped mesoporous carbon of extraordinary capacitance for electrochemical energy storage," Science (1979), vol. 350, no. 6267, pp. 1508–1513, Dec. 2015, doi: 10.1126/science.aab3798.

[154] D. Wei, Y. Liu, Y. Wang, H. Zhang, L. Huang, and G. Yu, "Synthesis of n-doped graphene by chemical vapor deposition and its electrical properties," Nano Lett, vol. 9, no. 5, pp. 1752–1758, 2009, doi: 10.1021/nl803279t.

[155] P. Huang et al., "Enhancing nitrogen electroreduction to ammonia by doping chlorine on reduced graphene oxide," ACS Catal, vol. 10, no. 24, pp. 14928–14935, 2020, doi: 10.1021/acscatal.0c03941.

[156] H. Karimi-Maleh, F. Tahernejad-Javazmi, N. Atar, M. L. Yola, V. K. Gupta, and A. A. Ensafi, "A Novel DNA Biosensor Based on a Pencil Graphite Electrode Modified with Polypyrrole/Functionalized Multiwalled Carbon Nanotubes for Determination of 6-Mercaptopurine Anticancer Drug," Ind Eng Chem Res, vol. 54, no. 14, pp. 3634–3639, Apr. 2015, doi: 10.1021/ie504438z.

[157] D. Khalili, "Graphene oxide : a promising carbocatalyst for the regioselective thiocyanation of aromatic amines , phenols , anisols and enolizable ketones by hydrogen peroxide / KSCN in water Department of Chemistry , College of Sciences , Shiraz University , Shiraz 7," New Journal of Chemistry, vol. 40, no. 3, pp. 2547–2553, 2016.

[158] B. Amanulla, K. N. Perumal, and S. K. Ramaraj, "Chitosan functionalized gold nanoparticles assembled on sulphur doped graphitic carbon nitride as a new platform for colorimetric detection of trace Hg2+," Sens Actuators B Chem, vol. 281, pp. 281–287, Feb. 2019, doi: 10.1016/J.SNB.2018.10.039.

[159] M. B. Arvas, H. Gürsu, M. Gencten, and Y. Sahin, "Preparation of different heteroatom doped graphene oxide based electrodes by electrochemical method and their supercapacitor applications," J Energy Storage, vol. 35, no. November 2020, 2021, doi: 10.1016/j.est.2021.102328.

[160] Y. Zhang, J. Zhao, H. Sun, Z. Zhu, J. Zhang, and Q. Liu, "B, N, S, Cl doped graphene quantum dots and their effects on gas-sensing properties of Ag-LaFeO3," Sens Actuators B Chem, vol. 266, pp. 364–374, 2018, doi: 10.1016/j.snb.2018.03.109.

[161] P. Simon and Y. Gogotsi, "Materials for electrochemical capacitors," Nat Mater, vol. 7, no. 11, pp. 845–854, 2008, doi: 10.1038/nmat2297.

[162] W. Nie et al., "Hierarchical Porous Carbon Anode Materials Derived from Rice Husks with High Capacity and Long Cycling Stability for Sodium-Ion Batteries," ChemElectroChem, vol. 7, no. 3, pp. 631–641, Feb. 2020, doi: https://doi.org/10.1002/celc.201901826.

[163] A. J. Bard, L. R. Faulkner, and H. S. White, Electrochemical methods: fundamentals and applications. John Wiley & Sons, 2022.

[164] M. Li et al., "Low-temperature performance of Na-ion batteries," 2024, John Wiley and Sons Inc. doi: 10.1002/cey2.546.

[165] C. Li et al., "Nitrogen and phosphorous dual-doped graphene aerogel with rapid capacitive response for sodium-ion batteries," Carbon N Y, vol. 139, pp. 1117–1125, Nov. 2018, doi: 10.1016/j.carbon.2018.06.035.

[166] H. Hou, C. E. Banks, M. Jing, Y. Zhang, and X. Ji, "Carbon Quantum Dots and Their Derivative 3D Porous Carbon Frameworks for Sodium-Ion Batteries with Ultralong Cycle Life," Advanced Materials, vol. 27, no. 47, pp. 7861–7866, Dec. 2015, doi: https://doi.org/10.1002/adma.201503816.

[167] G. Zou et al., "Carbon-coated rutile titanium dioxide derived from titanium-metal organic framework with enhanced sodium storage behavior," J Power Sources, vol. 325, pp. 25–34, 2016, doi: https://doi.org/10.1016/j.jpowsour.2016.06.017.

[168] W. Bai et al., “3D-Printed Hierarchically Microgrid Frameworks of Sodiophilic Co3O4@C/rGO Nanosheets for Ultralong Cyclic Sodium Metal Batteries,” Advanced Science, vol. 11, no. 35, p. 2404419, Sep. 2024, doi: https://doi.org/10.1002/advs.202404419.

[169] J. Wang et al., “Localized Electron Density Redistribution in Fluorophosphate Cathode: Dangling Anion Regulation and Enhanced Na-Ion Diffusivity for Sodium-Ion Batteries,” Adv Funct Mater, vol. 32, no. 4, Jan. 2022, doi: 10.1002/adfm.202109694.

[170] Y.-X. Wang, S.-L. Chou, H.-K. Liu, and S.-X. Dou, “Reduced graphene oxide with superior cycling stability and rate capability for sodium storage,” Carbon N Y, vol. 57, pp. 202–208, 2013.

[171] B. Jache and P. Adelhelm, “Use of Graphite as a Highly Reversible Electrode with Superior Cycle Life for Sodium-Ion Batteries by Making Use of Co-Intercalation Phenomena,” Angewandte Chemie International Edition, vol. 53, no. 38, pp. 10169–10173, Sep. 2014, doi: 10.1002/anie.201403734.

[172] H. Lindström et al., “Li+ Ion Insertion in TiO2 (Anatase). 2. Voltammetry on Nanoporous Films,” J Phys Chem B, vol. 101, no. 39, pp. 7717–7722, Sep. 1997, doi: 10.1021/jp970490q.

[173] T. -C. Liu, W. G. Pell, B. E. Conway, and S. L. Roberson, “Behavior of Molybdenum Nitrides as Materials for Electrochemical Capacitors: Comparison with Ruthenium Oxide,” J Electrochem Soc, vol. 145, no. 6, p. 1882, 1998, doi: 10.1149/1.1838571.

[174] V. Thirumal, P. Rajkumar, K. Yoo, and J. Kim, “Hydrothermal Synthesis of Boron-Doped Graphene for High-Performance Zinc-Ion Hybrid Capacitor Using Aloe Vera Gel Electrolyte,” Inorganics (Basel), vol. 11, no. 7, Jul. 2023, doi: 10.3390/inorganics11070280.

[175] I. Jeon et al., “Super-Fast Sodium Storage Properties of Nitrogen-Doped Graphene-Based Material Synthesized via Arc-Discharge Method,” Batteries, vol. 11, no. 4, Apr. 2025, doi: 10.3390/batteries11040135.

[176] B. Jache, J. O. Binder, T. Abe, and P. Adelhelm, “A comparative study on the impact of different glymes and their derivatives as electrolyte solvents for graphite co-intercalation electrodes in lithium-ion and sodium-ion batteries,” Physical Chemistry Chemical Physics, vol. 18, no. 21, pp. 14299–14316, 2016, doi: 10.1039/c6cp00651e.

PUBLICATIONS FROM THE THESIS

Conference Papers

1. MohammedMustafa ALMARZOGE, Metin GENÇTEN, and Gamzenur ÖZSİN. "Heteroatom Doped Graphene Oxide as an Anode Material for Na-ion Batteries," in Proc. 18th International Nanoscience and Nanotechnology Conference (NanoTR-18), Koç University, İstanbul, Türkiye, (2024).
2. Gamzenur ÖZSİN, MohammedMustafa ALMARZOGE, and Metin GENÇTEN. "Carbon-Based Anodes for Na-Ion Batteries: A Comparative Study of Electrochemical Performance and Enhanced Ion Storage," in Proc. The First AACG Carbon Symposium, Istanbul Technical University, Istanbul, Türkiye, (2025).

Papers

1. Almarzoge M, Gencten M, Ozsin G (2024) Production of Sulphur-Doped Graphene Oxide as an Anode Material for Na-Ion Batteries. ECS Journal of Solid State Science and Technology 13:071001. https://doi.org/10.1149/2162-8777/ad5b87.
2. Almarzoge M, Gencten M, Ozsin G (2025) One-Step Chronoamperometric Synthesized Nitrogen-Doped Graphene Oxide as a Novel Anode for Sodium-Ion Battery with an Enhanced Electrochemical Performance. ChemElectroChem 12:. https://doi.org/10.1002/celc.202400564.
3. Almarzoge, M., Gencten, M. & Ozsin, G. Exploring Chlorine Doping of Graphene Oxide Synthesized via Chronoamperometry for Enhanced Sodium-Ion Battery Anode Performance. Korean J. Chem. Eng. (2025). https://doi.org/10.1007/s11814-025-00556-4.

Books

1. M. Gencten, M. Almarzoge, A. V. Hacınecipoğlu, and B. Birol, "2.04-Graphene," I. B. T.-C. E. S. (Second E. Dincer, Ed., Oxford: Elsevier, 2025, pp. 104–138. https://doi.org/10.1016/B978-0-44-313219-3.00014-9.

Projects

1. Yildiz Technical University Scientific Research Council (BAP) for FCD-2024-6420.
2. Yildiz Technical University Scientific Research Council (BAP) for FDK-2024-6346 Doctoral Project code.